POLITEKNIK NEGERI BALI

Journal of Engineering Design and Technology

logic

Vol. 25 No. 3 November 2025

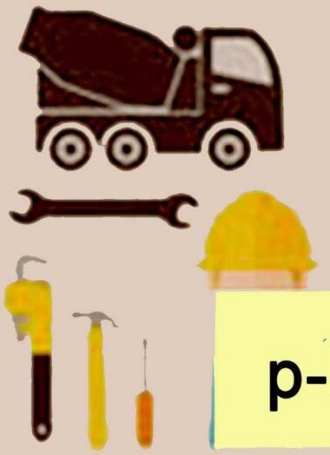

LOGIC

Jurnal Rancang Bangun dan Teknologi

p-ISSN. 1412-114X

e-ISSN. 2580-5649

LOGIC

Jurnal Rancang Bangun dan Teknologi

Journal of Engineering Design and Technology

Gedung P3M, lt.1 Politeknik Negeri Bali, Bukit Jimbaran
PO BOX 1064 Kuta Selatan, Badung, Bali - Indonesia
Telp. (+62)361 701981 Fax. (+62)361 701128
Email: logic@pnb.ac.id

LOGIC JOURNAL TEAM

PREFACE

Logic: Jurnal Rancang Bangun dan Teknologi (Journal of Engineering Design and Technology) is a peer-reviewed research journal aiming at promoting and publishing original high quality research in all disciplines of engineering and applied technology. All research articles submitted to Logic should be original in nature, never previously published in any journal or presented in a conference or undergoing such process across the world. All the submissions will be peer-reviewed by the panel of experts associated with particular field. Submitted papers should meet the internationally accepted criteria and manuscripts should follow the style of the journal for the purpose of both reviewing and editing.

Logic is a journal covering articles in the field of civil and mechanical engineering, design, and technology published 3 times a year in March, July, and November. Language used in this journal is English.

LOGIC. P-ISSN 1412-114X
LOGIC. E-ISSN 2580-5649
Indexing : GOOGLE SCHOLAR, DOAJ, EBSCO OPEN SCIENCE DIRECTORY, SINTA, GARUDA

Best Regard,

LOGIC Editorial Team

TABLE OF CONTENTS

LOGIC
Journal of Engineering Design and Technology
Vol. 25 No.3 November ; p. 140-146

p-ISSN : 1412-114X
e-ISSN : 2580-5649
http://ojs2.pnb.ac.id/index.php/LOGIC

UTILIZATION OF CORN COB WASTE AS AN ALTERNATIVE CATALYST IN CATALYTIC CONVERTERS FOR DIESEL ENGINE CARBON EMISSION REDUCTION

Muhamad Muhajir [1)*], Imron Musthofa [1)], Hajar Isworo[1)]
Muhammad Rezki Fitri Putra [2)], Bayu Agung Wicaksono [2)]

1) Heavy Equipment DepartmentTechnology. Politeknik Negeri Tanah Laut, Kalimantan Selatan
2) Automotive Technology Department. Politeknik Negeri Tanah Laut, Kalimantan Selatan

Correponding email [1)] : muhamadmuhajir@politala.ac.id

Abstract. Catalytic converters function to transform harmful exhaust gases into less hazardous substances through catalytic reactions, primarily oxidation and reduction. This study aims to investigate the potential of corncob waste as an alternative catalytic material in catalytic converters for reducing carbon emissions from diesel engines. The methodology involves synthesizing biochar-based catalysts derived from corncobs via pyrolysis, followed by performance evaluation within a catalytic converter system under varying engine speeds: 700 RPM, 900 RPM, and 1100 RPM. Experimental results demonstrate that catalytic efficiency does not increase monotonically with char content; instead, the 70% char formulation achieved the highest smoke opacity reduction, recording 18.90% at 700 RPM and 14.70% at 900 RPM, outperforming both the 50% and 100% variants at 1100 RPM, where exhaust temperature and flow rate increase substantially, the 100% char catalyst showed comparatively greater stability, achieving a reduction of 5.50%, while the 70% formulation declined to 2.90%. These quantitative outcomes confirm that optimal performance arises from a balanced char loading that maximizes reactive surface area while preserving gas–solid interaction efficiency. Corncob biochar thus represents a viable and sustainable alternative to metal-based catalysts. However, the variability in performance across operating conditions and the need for improved thermal durability underscore the importance of further material optimization for commercial diesel applications.

Keywords: Biochar, Catalyst, Catalytic Converter, Diesel Engine, Emissions.

1. INTRODUCTION

Escalating global concern over environmental degradation, particularly air pollution stemming from vehicular emissions, has catalyzed transformative shifts in industrial paradigms with the automotive sector at the forefront. Diesel engines, despite their operational efficiency and widespread deployment, remain significant contributors to atmospheric contamination through the release of noxious pollutants including particulate matter (PM), nitrogen oxides (NO_x), and carbon monoxide (CO). These emissions are causally linked to deteriorating urban air quality, elevated incidences of respiratory morbidity, and the exacerbation of secondary environmental phenomena such as acid precipitation and photochemical smog. In response, regulatory frameworks worldwide are progressively tightening emission thresholds, thereby intensifying the imperative for sustainable, high-efficiency emission abatement technologies [1], [2] .

Catalytic converters have long served as the principal engineering intervention for mitigating vehicular exhaust toxicity, leveraging catalytic oxidation and reduction reactions to convert hazardous compounds into benign byproducts. Conventional systems predominantly employ platinum-group metals (PGMs) notably platinum, palladium, and rhodium as catalytic agents. While highly efficacious, these materials entail substantial economic costs and pose sustainability challenges due to finite geological reserves and the ecologically deleterious

processes associated with their extraction and refinement. Consequently, the scientific community is increasingly directing efforts toward identifying economically viable and environmentally benign catalytic alternatives, with biomass-derived catalysts emerging as a compelling avenue for innovation [3], [4].

Among biomass feedstocks, agricultural residues particularly corncob have attracted considerable research interest owing to their abundant availability, high lignocellulosic content, and amenability to thermochemical conversion into functional biochar. Corncob-derived biochar exhibits favorable physicochemical attributes, including high specific surface area, hierarchical porosity, and carbon-rich composition, rendering it a promising substrate for catalytic applications. Empirical evidence indicates that such biochar can rival or even surpass conventional catalysts in specific contexts, while simultaneously advancing circular economy principles by valorizing waste streams and minimizing reliance on virgin resource extraction [5], [6], [7].

Notwithstanding these advantages, the practical deployment of biomass-derived catalysts in diesel aftertreatment systems confronts significant technical hurdles. Chief among these is the inherent heterogeneity in catalytic performance, attributable to feedstock variability and the sensitivity of pyrolysis parameters (e.g., temperature, heating rate, residence time) on biochar microstructure and active site distribution. Such inconsistencies compromise catalytic reproducibility and reliability under real-world operating conditions. Moreover, while laboratory-scale assessments often report encouraging results, biomass catalysts frequently exhibit diminished activity relative to PGMs under demanding operational regimes characterized by elevated temperatures and prolonged exposure to complex exhaust matrices [3], [8].

To address these limitations, recent research has explored multifaceted optimization strategies, including feedstock pre-treatment protocols, structural modification via heteroatom doping or surface functionalization, and hybridization with complementary catalytic materials. Metal doping, for instance, has been shown to augment catalytic activity by introducing redox-active centers, while surface engineering enhances gas-phase adsorption kinetics, thereby improving overall conversion efficiency [9]. Although these approaches have yielded measurable performance gains, scalability and long-term durability under industrial conditions remain critical research frontiers. The design and number of catalytic converters also contribute to reducing exhaust emissions [10], [11]

This study advances the field by experimentally evaluating the efficacy of corncob-derived biochar catalysts within a dynamically controlled diesel engine environment. Specifically, it investigates the influence of varying biochar loadings and engine operational parameters on the catalyst's capacity to mitigate smoke opacity and PM emissions. While prior investigations have validated the catalytic potential of corncob biochar under static or idealized conditions, a conspicuous knowledge gap persists regarding its behavior under transient, engine-representative regimes [12], [13].

The primary objective of this work is to bridge this empirical deficit by subjecting biomass-derived catalysts to realistic engine dynamics, thereby assessing their viability as drop in replacements for conventional PGM systems. The study's novelty resides in its explicit focus on dynamic performance metrics an aspect frequently neglected in bench-scale catalysis research. It is hypothesized that corncob biochar, when engineered through optimized synthesis protocols, can achieve catalytic performance commensurate with or exceeding that of noble metal benchmarks, thus offering a sustainable, cost-effective pathway for diesel emission control. The research scope encompasses catalyst synthesis, engine-integrated performance testing, and comparative analysis against standard catalytic converter configurations, contributing actionable insights toward the decarbonization and circularization of automotive aftertreatment technologies.

2. METHODS

This study encompasses material selection, catalyst synthesis, and experimental procedures specifically designed to evaluate the performance of corncob waste-based catalysts in reducing exhaust emissions from diesel engines. The research employs multiple catalyst models derived from corncob waste, processed into biochar and subsequently utilized as alternative catalytic materials in catalytic converter systems. The detailed methodology is outlined as follows:

2.1 Materials and Material Sources

The primary material used in this study is corncob waste (Zea mays), sourced from local agricultural areas in Tanah Laut Regency, near the research site. Only dried corncobs free from decay were selected to ensure optimal quality during processing. A total of 3 kg of dried corncobs was collected and used as the main feedstock for catalyst production.

2.2 Catalyst Preparation

Catalyst fabrication commenced with the carbonization of dried corncobs via pyrolysis. The pyrolysis process was conducted under controlled temperature conditions to yield biochar possessing a porous structure capable of enhancing catalytic activity. The resulting char was then ground into fine powder using a blender (Philips Model HR-2116); crushed corncobs were also finely milled to achieve uniform particle size. A total of 500 grams of char powder, obtained from carbonizing 3 kilograms of dried corncobs (yield ratio approximately 6:1), was used as the active catalytic material. For catalyst fabrication, the char powder was mixed with finely crushed corncob powder

according to the required composition ratios—50:50, 70:30, and 100:0—resulting in mass ratios of 250 g:250 g, 350 g:150 g, and 500 g:0 g, respectively. Each mixture was then blended with epoxy resin, and hardener was added at 10% of the total mixture weight. The mixture was homogenized and molded into cylindrical catalyst units. The mixture was homogenized and molded into cylindrical shapes using plastic molds (8 cm diameter, 10 cm height) with 17 perforations, producing three catalytic converter variants: (Figure 1a) converter with 50% char content, (Figure 1b) converter with 70% char content, and (Figure 1c) converter with 100% char content.

Figure 1. Catalytic converter from dry corn cobs and corn cob charcoal:
a. Charcoal 50%, b. Charcoal 70%, c. Charcoal 100%

2.3 Catalyst Housing Fabrication

The catalyst housing, commonly referred to as the "property tube," was engineered to securely contain the catalyst and ensure proper integration into the exhaust system of the test vehicle. As illustrated in Figure 2, the housing design was initially modeled using AutoCAD software and subsequently fabricated physically at the Automotive Technology Workshop of Politeknik Negeri Tanah Laut (POLITALA). This housing serves to uniformly distribute exhaust gases during testing and to guarantee optimal contact between the exhaust stream and the catalyst surface.

Figure 2. Catalyst housing

2.4 Catalytic Converter Assembly

Upon completion of the housing fabrication, the molded catalysts dried for 48 hours were prepared for installation into the exhaust system of the test vehicle. The catalyst units were mounted at the exhaust outlet of the test engine, ensuring precise alignment and mechanical stability throughout the experimental trials to prevent displacement or leakage during operation.

2.5 Experimental Procedure

The experiments were conducted using a diesel-powered test vehicle (Quick G 1000 Tractor) located at the Automotive Technology Workshop of Politeknik Negeri Tanah Laut (Politala). Three distinct corncob waste-based catalytic converter models, previously fabricated, were evaluated. Each catalyst unit was sequentially installed into the vehicle's exhaust system and tested across three engine speeds: 700 RPM, 900 RPM, and 1100 RPM. Engine speed was monitored using a photo-mode tachometer mounted on the flywheel to ensure accurate and consistent RPM readings throughout data acquisition. Each experimental run was maintained for a minimum of one minute per variable, with smoke opacity measurements repeated at least twice to guarantee data reliability and reproducibility.

2.6 Data Measurement and Analysis

Collected data included smoke opacity levels recorded at each tested RPM. Opacity measurements were performed using a smoke analyzer (Exhaust Gas Tester Model OP-201), which quantifies light extinction percentage (% opacity) of the exhaust stream. The acquired data were subsequently analyzed to compare emission reduction performance between the corncob-based catalytic converter models and a conventional catalytic converter serving as the baseline reference. Statistical evaluation was employed to determine the significance of observed differences

and to correlate catalytic efficiency with engine speed and char content variation [14].

3. RESULTS AND DISCUSSION

The results and discussion presented in this study evaluate the performance of corncob-based catalysts in reducing smoke opacity from diesel engine exhaust emissions. The investigation employed three catalyst models containing varying proportions of corncob char (50%, 70%, and 100%), which were tested across three engine speed conditions (700 RPM, 900 RPM, and 1100 RPM) to systematically assess catalytic effectiveness under dynamic operational parameters.

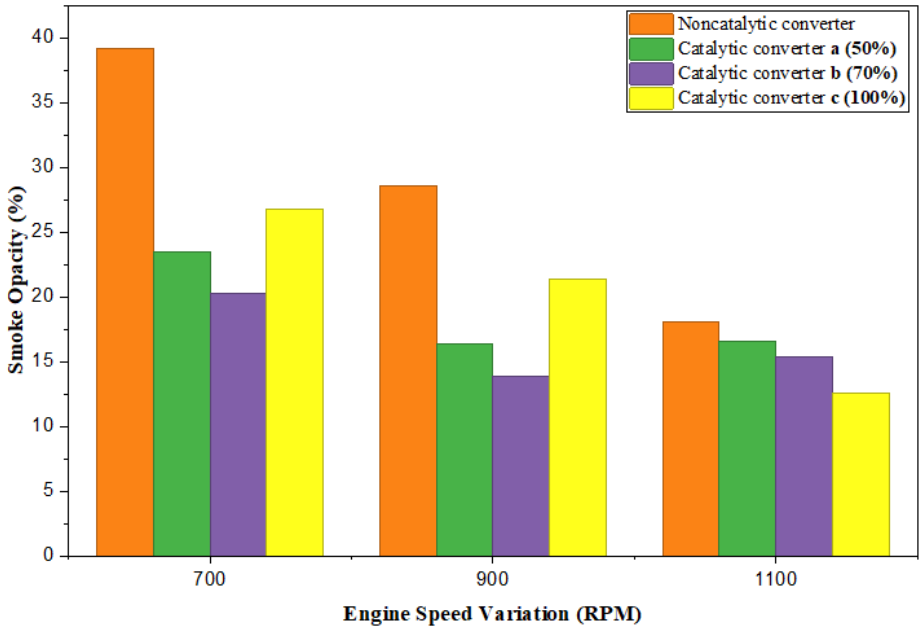

Figure 2. Reduction in smoke opacity across different catalytic converter models

Experimental results show a clear link between the proportion of corncob-derived biochar in the catalyst and smoke opacity reduction. Of the three formulations, the 70% char catalyst cut smoke opacity the most at critical engine speeds of 700 and 900 RPM. This composition achieves the best balance between active surface area and structural integrity. Catalytic performance does not increase linearly with the addition of more char; rather, the 70% formulation is optimal. It offers the most reactive sites while maintaining strong mass transfer. These findings support earlier literature that notes catalytic efficiency depends not just on the number of carbonaceous active sites but on achieving the right microstructure. This structure promotes surface-mediated redox reactions [15]. The high carbon matrix in corncob biochar enhances interactions with exhaust gases, boosting oxidation of particulate matter (PM).

The 50% char formulation resulted in modest reductions in opacity, which were still statistically significant at all engine speeds. The 70% char variant achieved the most reduction and consistently outperformed both the 50% and 100% formulations, especially at 700 and 900 RPM. This suggests that catalytic efficiency does not consistently rise with increased char; rather, the 70% composition strikes the best balance between reactive sites and structural strength. The data show that excessive char, as in the 100% formulation, may block gas–solid interaction or weaken the substrate, thereby reducing efficiency. Thus, it is essential to determine the optimal char content, rather than simply maximizing it, to control emissions while preserving the catalyst's structure and function.

3.1 Impact of Engine Speed on Catalytic Efficiency

Figure 3 demonstrates that engine rotational speed strongly influences catalytic functionality. The data show that smoke opacity reduction decreases progressively as engine speed increases. At 700 RPM, all catalyst models achieve their highest reduction performance. This suggests that the lower engine load and slower exhaust flow enhance gas–catalyst residence time and interfacial interaction, leading to more effective conversion. The 70% char catalyst achieves the greatest reduction at this speed, followed by the 50% and 100% formulations.

As engine speed rises to 900 RPM, catalyst performance drops for all types. The 70% char catalyst still achieves the best reduction, but the loss of efficiency shows that faster exhaust lowers contact time. Note that more exhaust flow increases mixing, but the graph shows that shorter contact at this speed reduces pollutant-catalyst contact [16].

At 1100 RPM, efficiency drops more noticeably. The 50% and 70% char catalysts sharply reduce opacity control, while the 100% char catalyst shows better stability and the highest reduction at this speed. This may result from the greater thermal tolerance of higher carbon content materials. Still, overall reduction remains low, suggesting that high exhaust temperatures and rapid gas flow hinder catalytic activity. These findings align with Yu et al. (2020), who observed that even with improved gas–solid contact at higher speeds, biomass-derived catalysts often face performance limits from structural and thermal constraints [16].

Furthermore, the elevated exhaust temperatures associated with higher engine speeds may trigger thermal degradation pathways, a concern also highlighted by Lott & Deutschmann (2020) [16]. Such thermal stress can compromise the long-term structural stability of biochar-based catalysts, making sustained operation at high RPM challenging. Thus, although biomass-derived catalysts perform effectively at lower engine speeds, the decline in efficiency with increasing RPM underscores the need for further optimization to ensure long-term thermal resilience and practical deployment in real-world diesel applications.

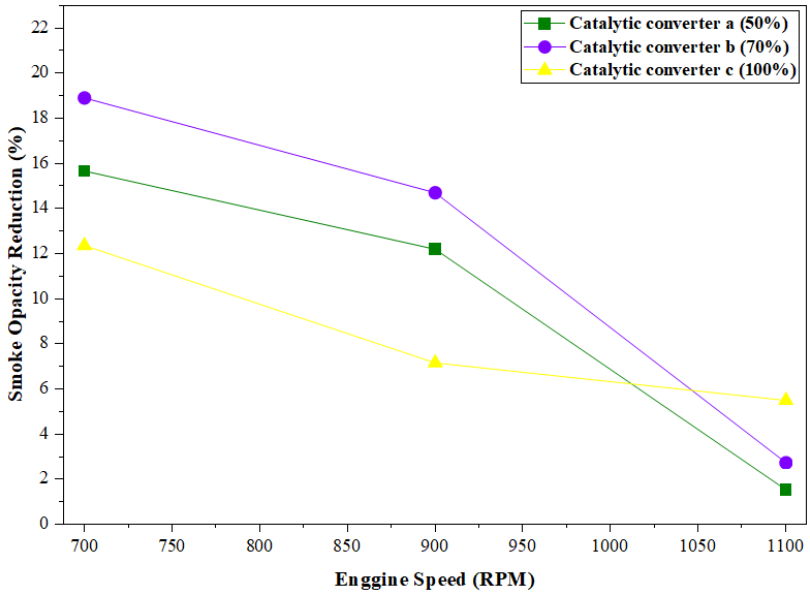

Figure 3. Impact of engine speed on catalytic efficiency

3.2 Thermal Effects on Catalytic Activity

Operating temperature is a key modulator of catalytic kinetics. As engine speed increases, exhaust gas temperature also rises, directly influencing reaction rates by providing the thermal energy required to overcome activation barriers [8]. However, excessive thermal exposure may induce catalyst deactivation, particularly in formulations with insufficient structural reinforcement, through mechanisms such as pore collapse, surface oxidation, or degradation of functional groups.

In this study, the 70% char catalyst demonstrated the most favorable balance between catalytic activity and thermal tolerance, maintaining higher efficiency than both the 50% and 100% formulations across the entire temperature range tested. Although carbon-rich structures can exhibit enhanced thermal stability as noted by Yu et al. (2021), the 100% char catalyst did not outperform the optimized 70% formulation, likely due to reduced structural cohesion or less effective gas–solid interaction at elevated temperatures [17]. While higher temperatures at increased engine speeds can promote more vigorous pollutant–catalyst interactions [18]. Performance declines beyond certain thresholds indicate the onset of thermal stress. Therefore, operational temperature must be carefully optimized within the engine's performance envelope to sustain catalytic efficiency and ensure long-term material durability in real-world applications[19].

3.3 Long-Term Stability and Structural Durability

The viability of corncob derived catalysts in commercial diesel systems hinges critically on their ability to maintain structural and chemical integrity under prolonged, dynamic operating conditions including thermal cycling, oxidative stress, and moisture exposure. Experimental assessments revealed that the 100% char catalyst retained its performance significantly better than lower loading variants following repeated thermal and hygrothermal stress cycles. In contrast, the 50% and 70% formulations exhibited accelerated performance decay, indicating diminished resistance to environmental degradation.

These findings echo Yu et al. (2020), who identified thermal and oxidative instability as key limitations of biomass-based catalysts [20]. Enhancing char content not only amplifies initial catalytic activity but also fortifies long-term durability by improving structural coherence and resistance to active site depletion. To further augment resilience, future formulations may incorporate stabilizing agents such as inorganic binders or metal oxide

promoters or leverage advanced synthesis techniques including controlled activation, heteroatom doping, or hybridization with thermally stable ceramic supports [21]. Such innovations are essential to translate laboratory-scale efficacy into industrially viable, durable emission control solutions.

3.4 Comparative Analysis with Noble Metal Catalysts

When benchmarked against conventional platinum or palladium-based catalysts, corncob-derived systems exhibit competitive though not yet equivalent performance in smoke opacity reduction. Noble metal catalysts remain unmatched in terms of intrinsic activity and reaction selectivity, particularly for complex oxidationreduction pathways [22]. However, their prohibitive cost and geologically constrained supply render them unsustainable for global, long-term deployment [20]. Biomass derived alternatives offer a compelling substitute by leveraging renewable agricultural residues, thereby reducing dependency on critical raw materials and advancing circular economy objectives [7]

Although the corncob catalysts achieved comparable opacity reductions under specific operational windows, inconsistencies in performance across variable loads and evidence of progressive deactivation highlight the need for further material optimization. Strategic enhancements such as metal oxide doping, catalytic pyrolysis, or chemical activation protocols may bridge the efficiency gap while improving thermal and mechanical robustness [23]. These advancements are imperative to enable scalable, reliable integration of biomass-derived catalysts into commercial aftertreatment systems.

4. CONCLUSION

This study demonstrates that corncob-based catalysts can effectively reduce smoke opacity in diesel engine exhaust, with performance governed by both char composition and engine operating conditions. Quantitative results confirm that the 70% char formulation provides the highest reduction, achieving 18.90% at 700 RPM and 14.70% at 900 RPM, reflecting an optimal balance between reactive surface area and structural cohesion. At elevated speeds, the 100% char catalyst exhibits comparatively better thermal stability, recording 5.50% reduction at 1100 RPM, although its overall performance remains below that of the optimized 70% formulation. These trends highlight the dependence of catalytic efficiency on gas–solid residence time and thermal loading, both of which diminish as engine speed increases. Despite the promising performance of biochar-based catalysts, challenges remain regarding consistency and long-term durability under high-temperature exhaust environments. Future studies should focus on enhancing catalyst robustness through improved activation techniques, thermally stable binders, and metal oxide promoters. Extended engine endurance testing and validation across diverse diesel platforms are also recommended to support practical implementation and advance industrial adoption.

5. ACKNOWLEDGEMENT

The authors express their deepest gratitude to Politeknik Negeri Tanah Laut (POLITALA) for providing essential institutional support, including access to research facilities, academic opportunities, and a conducive scholarly environment that greatly facilitated the preparation of this manuscript. Special appreciation is extended to all individuals who contributed valuable insights, constructive feedback, and intellectual guidance throughout the research and writing process. Their thoughtful input significantly enhanced both the coherence and academic rigor of this work. The authors also acknowledge the collective effort of colleagues, mentors, and technical staff whose unwavering support played an indispensable role in the successful completion of this study.

6. REFERENCES

[1] F. Knobloch *et al.*, “Net Emission Reductions From Electric Cars and Heat Pumps in 59 World Regions Over Time,” *Nat Sustain*, vol. 3, no. 6, pp. 437–447, 2020, doi: 10.1038/s41893-020-0488-7.

[2] I. Yakoumis, A. Moschovi, M. Panou, and D. Panias, “Single-Step Hydrometallurgical Method for the Platinum Group Metals Leaching From Commercial Spent Automotive Catalysts,” *Journal of Sustainable Metallurgy*, vol. 6, no. 2, pp. 259–268, 2020, doi: 10.1007/s40831-020-00272-9.

[3] L. Robles-Lorite, R. Dorado-Vicente, E. Torres-Jiménez, G. Bombek, and L. Lešnik, “Recent Advances in the Development of Automotive Catalytic Converters: A Systematic Review,” *Energies (Basel)*, vol. 16, no. 18, p. 6425, 2023, doi: 10.3390/en16186425.

[4] H. Wakudkar and S. Jain, "A Holistic Overview on Corn Cob Biochar: A Mini-Review," *Waste Management &Amp; Research: The Journal for a Sustainable Circular Economy*, vol. 40, no. 8, pp. 1143–1155, 2022, doi: 10.1177/0734242x211069741.

[5] S. Pradhan, H. R. Mackey, T. A. Al-Ansari, and G. McKay, "Biochar From Food Waste: A Sustainable Amendment to Reduce Water Stress and Improve the Growth of Chickpea Plants," *Biomass Convers Biorefin*, vol. 12, no. 10, pp. 4549–4562, 2022, doi: 10.1007/s13399-022-02575-1.

[6] F. O. Ochedi, J. Yu, H. Yu, Y. Liu, and A. Hussain, "Carbon Dioxide Capture Using Liquid Absorption Methods: A Review," *Environ Chem Lett*, vol. 19, no. 1, pp. 77–109, 2020, doi: 10.1007/s10311-020-01093-8.

[7] S. Sampaolesi, L. E. Briand, M. C. N. Saparrat, and M. V. Toledo, "Potentials of Biomass Waste Valorization: Case of South America," *Sustainability*, vol. 15, no. 10, p. 8343, 2023, doi: 10.3390/su15108343.

[8] F. Leach, M. Peckham, and M. Hammond, "Identifying NOx Hotspots in Transient Urban Driving of Two Diesel Buses and a Diesel Car," *Atmosphere (Basel)*, vol. 11, no. 4, p. 355, 2020, doi: 10.3390/atmos11040355.

[9] E. Santolini, M. Bovo, A. Barbaresi, D. Torreggiani, and P. Tassinari, "Turning Agricultural Wastes Into Biomaterials: Assessing the Sustainability of Scenarios of Circular Valorization of Corn Cob in a Life-Cycle Perspective," *Applied Sciences*, vol. 11, no. 14, p. 6281, 2021, doi: 10.3390/app11146281.

[10] A. Ghofur *et al.*, "Modelling study of flue gas flow pattern with pressure, amount and shape variation catalytic converter," *Archives of Materials Science and Engineering*, vol. 103, no. 1, pp. 5–17, 2020, doi: 10.5604/01.3001.0014.1769.

[11] H. Isworo *et al.*, "PENGARUH CATALYTIC CONVERTER BERBAHAN ALUMUNIUM, SENG TERHADAP KEMAMPUAN REDUKSI EMISI GAS BUANG, DAN PERFORMA PADA SEPEDA MOTOR 110 CC," *JTAM ROTARY*, vol. 6, no. 2, p. 117, May 2024, doi: 10.20527/jtam_rotary.v6i2.12322.

[12] A. Hamid *et al.*, "An Improvement of Catalytic Converter Activity Using Copper Coated Activated Carbon Derived from Banana Peel," *International Journal of Renewable Energy Development*, vol. 12, no. 1, pp. 144–154, Jan. 2023, doi: 10.14710/ijred.2023.48739.

[13] S. Ullah, S. Hussain, N. A. Shah, and T. Akitsu, "Catalytic Reduction of Anthropogenic Pollutants over Gold (Au) Based Activated Charcoal," 2024, doi: 10.35248/2161-0495.24.14.554.

[14] J. Akhtar *et al.*, "Torrefaction and Thermochemical Properties of Agriculture Residues," *Energies (Basel)*, vol. 14, no. 14, p. 4218, 2021, doi: 10.3390/en14144218.

[15] Y. Gao, M. Li, J. Xue, and Y. Liu, "Evaluation of Effectiveness of China's Carbon Emissions Trading Scheme in Carbon Mitigation," *Energy Econ*, vol. 90, p. 104872, 2020, doi: 10.1016/j.eneco.2020.104872.

[16] P. Lott and O. Deutschmann, "Lean-Burn Natural Gas Engines: Challenges and Concepts for an Efficient Exhaust Gas Aftertreatment System," *Emission Control Science and Technology*, vol. 7, no. 1, pp. 1–6, 2020, doi: 10.1007/s40825-020-00176-w.

[17] D. Yu *et al.*, "Dual-Sites Coordination Engineering of Single Atom Catalysts for Flexible Metal–Air Batteries," *Adv Energy Mater*, vol. 11, no. 30, 2021, doi: 10.1002/aenm.202101242.

[18] S. M. Bagheri, Y. Huang, P. Walker, J. L. Zhou, and N. C. Surawski, "Strategies for Improving the Emission Performance of Hybrid Electric Vehicles," *Sci Total Environ*, vol. 771, p. 144901, 2021, doi: 10.1016/j.scitotenv.2020.144901.

[19] S. Hajimirzaee and A. M. Doyle, "3D Printed Catalytic Converters With Enhanced Activity for Low-Temperature Methane Oxidation in Dual-Fuel Engines," *Fuel*, vol. 274, p. 117848, 2020, doi: 10.1016/j.fuel.2020.117848.

[20] C. Yu *et al.*, "Agricultural Waste Derived Catalysts for Low Temperature SCR Process: Optimization of Preparation Process, Catalytic Activity and Characterization," *Aerosol Air Qual Res*, vol. 20, no. 4, pp. 862–876, 2020, doi: 10.4209/aaqr.2019.11.0596.

[21] J. T. Cunha *et al.*, "Consolidated Bioprocessing of Corn Cob-Derived Hemicellulose: Engineered Industrial Saccharomyces Cerevisiae as Efficient Whole Cell Biocatalysts," *Biotechnol Biofuels*, vol. 13, no. 1, 2020, doi: 10.1186/s13068-020-01780-2.

[22] M. J. B. Kabeyi and O. A. Olanrewaju, "Sustainable Energy Transition for Renewable and Low Carbon Grid Electricity Generation and Supply," *Front Energy Res*, vol. 9, 2022, doi: 10.3389/fenrg.2021.743114.

[23] C. M. Cova, A. Zuliani, R. Manno, V. Sebastian, and R. Luque, "Scrap Waste Automotive Converters as Efficient Catalysts for the Continuous-Flow Hydrogenations of Biomass Derived Chemicals," *Green Chemistry*, vol. 22, no. 4, pp. 1414–1423, 2020, doi: 10.1039/c9gc04091a.

LOGIC
Journal of Engineering Design and Technology
Vol. 25 No.3 November 2025 ; p. 147 - 155

p-ISSN : 1412-114X
e-ISSN : 2580-5649
http://ojs2.pnb.ac.id/index.php/LOGIC

ANALYSIS OF TENSILE STRENGTH IN A COMBINATION OF RECYCLED HDPE PLASTIC AND LIQUID ASPHALT

Achmad Bryan Baharrudin Sofan [1], Moh. Hartono [1)*]

1) Mechanical Engineering Departement, Politeknik Negeri Malang, Jl Soekarno-Hatta 9, Malang, Indonesia

Correponding email [1)] : moh.hartono@polinema.ac.id

***Abstract*.** Plastic waste reuse has gained significant attention due to its potential to reduce environmental pollution and provide alternative materials for engineering applications, particularly in the construction sector where durability and maintenance issues are common. One persistent problem in building structures is roof leakage caused by long-term exposure to rainfall, ultraviolet radiation, and extreme temperature changes, which gradually damage conventional waterproofing materials. To improve performance, materials with higher tensile strength and flexibility are needed. High-Density Polyethylene (HDPE), a thermoplastic known for its strength and durability, offers promising reinforcement when combined with liquid asphalt, while also supporting environmentally sustainable practices by reducing plastic waste. In this study, liquid asphalt was heated to 40°C and mixed with HDPE heated at 200°C, 210°C, and 220°C, then stirred for 1.5 hours until homogeneous, cooled to room temperature, and molded according to ASTM D638 for tensile testing. The results show that the 90:10 (HDPE: asphalt) composition at 200°C produced the highest tensile strength of 6.14 MPa, while the 80:20 composition at 220°C showed the lowest value of 3.86 MPa, indicating that higher HDPE content at optimal melting temperatures enhances mechanical properties and provides strong potential for use as a durable, environmentally friendly waterproofing layer in building construction.

Keywords : Liquid Asphalt, Recycle HDPE, Tensile test.

1. INTRODUCTION

Plastic, a petroleum-derived material [1], is widely used in various aspects of daily life, ranging from packaging products to industrial components, and as a result, the global plastic waste crisis continues to worsen. Data shows that in 2022, global plastic production reached 400.3 million tons, with most of it ending up as waste that is difficult to decompose in the environment [2]. Managing plastic waste, particularly from domestic and industrial sectors, remains a significant unresolved challenge. HDPE that is not properly recycled can persist in the environment for hundreds of years, causing ecosystem disruption, soil contamination, and potential health risks to humans [3]. Several approaches have been explored to reduce plastic waste, one of which is the incorporation of recycled HDPE into asphalt mixtures as a means to improve material performance while supporting environmental sustainability.

Research has shown that adding HDPE to 60/70 penetration asphalt can enhance several physical properties, including penetration, softening point, specific gravity, and viscosity, while simultaneously reducing ductility, indicating that the presence of HDPE alters the mechanical behavior of the asphalt binder [4]. Further studies also highlight that HDPE-blended asphalt exhibits higher stiffness compared to conventional mixtures, as reflected by the increase in stability values from 1729.31 kg in mixtures without HDPE to 1776.77 kg, 1797.07 kg, and 1840.90 kg in mixtures containing 12%, 14%, and 16% HDPE, respectively [5]. In addition, HDPE-modified asphalt demonstrates increased density due to reduced pore size and a higher softening point, making the

mixture more resistant to high temperatures and environmental conditions. The decrease in penetration values with the addition of HDPE indicates a stiffer binder, which can improve structural performance, although mixtures containing 6% HDPE do not meet the penetration requirements for modified asphalt [6].

However, the majority of these studies focus on road pavement applications, and there are still very few that evaluate HDPE as a mixture for coating materials in buildings, such as roofs or protective surfaces. Meanwhile, roof damage due to rainwater is common, such as holes around loose, rusted, or widened nails, allowing water to seep in and damage the building structure below [7]. To address this issue, this study developed a new material based on a mixture of liquid asphalt and High-Density Polyethylene (HDPE) plastic. Liquid asphalt, which is asphalt melted with a solvent from petroleum refining [8], is known for its waterproof properties and is commonly used as a roof coating. HDPE was chosen for its good mechanical properties and its ability to enhance the stiffness and waterproofing properties of the asphalt mixture [5]. Additionally, the temperature of HDPE plastic is 180–230 °C [9]. This study aims to produce a new material and explore the potential use of HDPE as a coating material.

To produce new material that is homogeneous and has optimal tensile properties, a proper mixing process is required. One method commonly used in mixing plastic and asphalt is the hot-hot mix method, which involves mixing plastic and asphalt while both are in a molten state [10]. This method is believed to produce better molecular integration than the cold method.

This study aims to examine the effect of HDPE temperature and mixture composition on the tensile strength of the material, using the ASTM D638 standard tensile test, which is widely used for testing plastic-based materials [11]. With this approach, it is hoped that new materials can be developed that are not only strong and durable but also environmentally friendly through the use of recycled plastic waste. Therefore, further research is still needed to understand how variations in temperature and mixture composition can affect mechanical properties, particularly tensile strength. This testing aims to determine how much the material can stretch without suffering permanent damage. Additionally, this research aims to contribute ideas for the utilization of plastic waste as an alternative for recycling.

2. METHODS

Figure 1 illustrates the research framework that follows. The research was conducted experimentally at the Material Testing Laboratory of the State Polytechnic of Malang from April to July 2025. The treatment variations consisted of three HDPE temperatures, namely 200 °C, 210 °C, and 220 °C, as well as three HDPE: liquid asphalt mixture compositions, namely 80:20, 85:15, and 90:10. The research was limited to HDPE recycled plastic pellets and MC 30 liquid asphalt. The plastic mixing method uses a method in which hot asphalt meets hot plastic. Tensile test was used to evaluate the mechanical properties of the mixture.

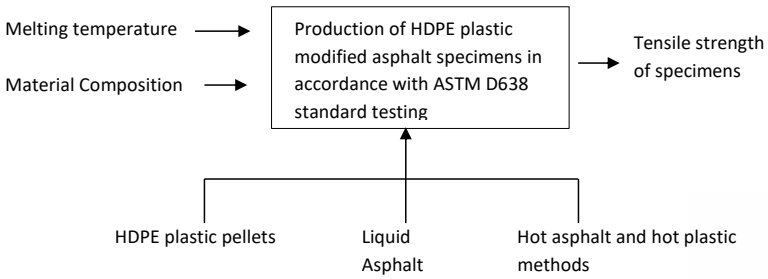

Figure 1. Research concept framework

The specimen production process begins with the selection of recycled HDPE plastic pellets as the main material to be mixed with MC 30 liquid asphalt. The first step involves calculating the mold volume based on the standard ASTM D638 mold dimensions to determine the amount of material required for each composition variation, such as 80:20, 85:15, and 90:10 (HDPE: liquid asphalt). After the mass of each material is obtained from the calculation of volume fraction and density, the heating process is carried out separately for both materials. Recycled HDPE plastic was heated in a pan until it reached its point at 200°C, 210°C, or 220°C depending on the treatment variation, while MC 30 liquid asphalt was heated in a separate container until it reached 40°C to remain in a liquid state. The mixing method used in this study is the hot asphalt–hot plastic mixture method, where both materials are first heated separately until they reach a liquid state, then mixed in a single container while both are still hot [13]. This method (Figure 2) is considered the most effective as it produces better molecular mixing and avoids the formation of lumps due to temperature differences. After the liquid asphalt was poured into the melted HDPE,

the mixture was manually stirred using a metal spatula for 15–30 minutes until homogeneous, indicated by a uniform dark brown color change. The hot mixture is then poured into a metal mold, allowed to cool and harden at room temperature, then the specimen is removed from the mold and cut using a band saw to meet the ASTM D638 tensile test standard.

Figure 2. Specimen manufacture

In this study, tensile testing was used to test the strength of a material under axial force. Tensile testing was carried out by continuously pulling the test specimen with tensile force, so that the material (its elongation) continued to increase steadily until it broke, with the aim of determining the tensile value [11]. The testing standard used in this study is ASTM D638, which is a specific tensile test method for plastic-based materials [13]. This standard was chosen based on its suitability for the characteristics of the material used, namely a mixture of HDPE plastic and liquid asphalt, where mechanical properties such as tensile strength and maximum strain are the main parameters observed. Figure 3 shows an image of the tensile test specimen using the ASTM D638 standard. The standard sizes are shown in Table 1.

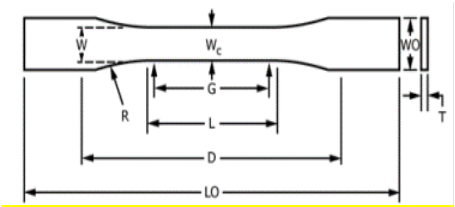

Figure 3. Spesimen ASTM D638

Table 1. Description Spesimen ASTM D638

No ID	Description	Dimension (mm)
1	Total length (L0)	165
2	Distance between grips (D)	115
3	Length of parallel section (L)	57
4	Gauge Length (G)	50
5	Radius (R)	76
6	Parallel section width	13
7	Total width (W0)	19
8	Thickness	4

3. RESULTS AND DISCUSSION

The tensile test data was processed with three replications to ensure the accuracy of the test data. Table 2 shows the tensile test results. Based on the test results, the tensile strength of each variation of point temperature at 200°C, 210°C, and 220°C and the composition of the mixture of the two materials between recycled HDPE plastic and liquid asphalt was obtained.

Table 2. Tensile Test Data

No	Temperature (°C)	Composition HDPE:Asphalt (%)	Pull Force (kg)	Pull Force(N)	Elongation (mm)	Tensile Test(MPa)	Strain (%)
1	200	80:20	23.6	231.28	7.82	4.81	0.16
2	200	80:20	22.4	219.52	9.96	4.56	0.2
3	200	80:20	21.6	211.68	6.22	4.40	0.12
4	200	85:15	26.2	256.76	6.84	5.34	0.14
5	200	85:15	28.4	278.32	6.31	5.79	0.13
6	200	85:15	32.6	319.48	3.47	6.64	0.07
7	200	90:10	29.6	290.08	4.71	6.03	0.09
8	200	90:10	27.2	266.56	4.27	5.54	0.09
9	200	90:10	33.6	329.28	5.51	6.85	0.11
10	210	80:20	22.4	219.52	6.84	4.56	0.13
11	210	80:20	18.2	178.36	8.18	3.71	0.16
12	210	80:20	21.2	207.76	2.48	4.32	0.04
13	210	85:15	28.6	280.28	4.97	5.83	0.11
14	210	85:15	22.2	217.56	6.22	4.52	0.12
15	210	85:15	20.2	197.96	5.77	4.12	0.12
16	210	90:10	25.4	248.92	12.26	5.18	0.24
17	210	90:10	31.4	307.72	8.98	6.40	0.17
18	210	90:10	29.2	286.16	16.79	5.95	0.33
19	220	80:20	16.4	160.72	3.47	3.34	0.06
20	220	80:20	19.8	194.04	2.84	4.03	0.05
21	220	80:20	20.6	201.88	4.00	4.20	0.08
22	220	85:15	22.8	223.44	8.98	4.65	0.17
23	220	85:15	23.8	233.24	2.22	4.85	0.04
24	220	85:15	22.4	219.52	6.22	4.56	0.12
25	220	90:10	27.6	270.48	6.84	5.62	0.13
26	220	90:10	27.8	272.44	5.15	5.66	0.1
27	220	90:10	28.4	278.32	8.18	5.79	0.15

The maximum tensile load is the highest force value achieved by the specimen before failure or breakage. Then, the maximum tensile strength is calculated by dividing the maximum load by the cross-sectional area of the test specimen. This value represents the maximum stress that the material can withstand before permanent deformation or failure occurs, as shown in Table 3.

Table 3. Maximum Tensile Strength Data

Temperature (°C)	HDPE composition: Asphalt (%)	Tensile Strength (MPa)			Average Tensile Strength (Mpa)
		Test 1	Test 2	Test 3	
200 C	80:20	4.81	4.56	4.40	4.59
210 C		5.38	3.71	4.32	4.47
220 C		3.34	4.03	4.20	3.86
200 C	85:15	5.42	5.79	6.64	5.95
210 C		5.83	4.52	4.12	4.82
220 C		4.65	4.85	4.56	4.69
200 C	90:10	6.03	5.54	6.85	6.14
210 C		5.18	6.40	5.95	5.84
220 C		5.62	5.66	5.79	5.69

Figure 4 shows a diagram of the relationship between tensile stress and strain of specimens made from a mixture of recycled HDPE plastic and liquid asphalt with a composition ratio of 80/20 at melting temperatures of 200°C, 210°C, and 220°C. This graph provides an overview of the mechanical characteristics of each specimen in relation to the plastic deformation that occurred during the tensile test. Based on Figure 4, the relationship between stress and strain in the recycled HDPE and liquid asphalt mixture with a composition of 80/20 shows differences in behavior at each variation in temperature. At 200 °C, stress increases steadily until reaching a maximum value of 4.8 MPa at a strain of 0.1564%, indicating that the material has good strength and flexibility. At 210 °C, stress increases and then suddenly decreases, with a lower strain compared to 200 °C. Meanwhile, at 220 °C, the stress tends to be low, and the graph flattens out after a certain point. This indicates that an increase in melting temperature affects the reduction in the material's mechanical performance, and 200 °C is the most optimal condition within this testing range.

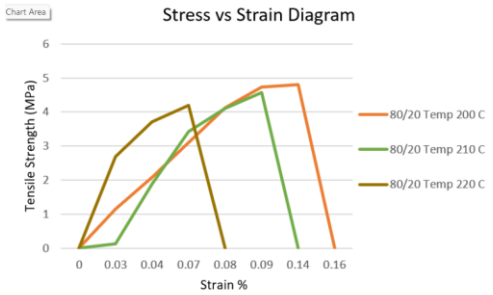

Figure 4. Stress-strain graph of 80/20 composition

Figure 5 shows a graph of the relationship between tensile stress and strain in specimens composed of 85% recycled HDPE plastic and 15% liquid asphalt, tested at three different melting temperatures: 200°C, 210°C, and 220°C. It shows that the melting temperature affects the tensile strength of the recycled HDPE and liquid asphalt mixture with a composition of 85:15. A temperature of 200°C produces the highest maximum stress of 6.5 MPa with a strain of around 0.03%, indicating the best mechanical performance. At 210°C, the stress decreases to approximately 5.7 MPa, while at 220°C the stress value is lower and the graph tends to flatten out. This indicates that 200°C is the most optimal temperature for producing a material that is both strong and sufficiently elastic at this composition.

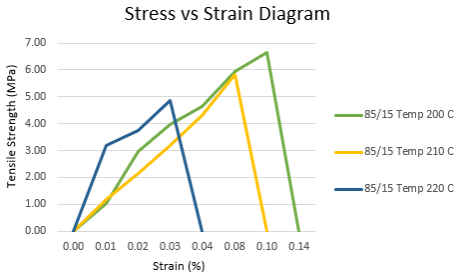

Figure 5. Stress-strain graph of 85/15 composition

Figure 6 shows a graph of the relationship between tensile stress and strain in specimens composed of 90% recycled HDPE plastic and 10% liquid asphalt, tested at melting temperatures of 200°C, 210°C, and 220°C.

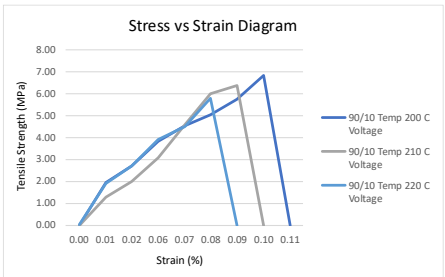

Figure 6. Stress-strain graph of 90/10 composition

It shows that the melting temperature affects the tensile strength of the recycled HDPE and liquid asphalt mixture with a composition of 90:10. A temperature of 200°C produces the highest maximum stress of 6.85 MPa with a strain of approximately 0.11%, indicating the best performance. At 210°C, the stress decreases to approximately

6.4 MPa, and the graph drops sharply after the peak. At 220°C, the stress is lower, and the curve tends to flatten out. Therefore, 200°C is the most optimal condition for this composition.

To determine the extent of the influence of melting temperature, the composition of the HDPE plastic and liquid asphalt mixture, and the interaction between the two on the tensile strength of the material, a two-way analysis of variance (ANOVA) was performed. The ANOVA test results are presented in Table 4.

Table 4. Results of Two-Way ANOVA Analysis

Analysis of Variance

Source	Df	Adj SS	Adj MS	F-Value	P-Value
temperature (°C)	2	3.1502	1.5751	5.61	0.013
Composition HDPE:Asphalt	2	12.6777	6.3389	22.58	0.000
temperature (°C)*Composition HDPE:Asphalt	4	0.7275	0.1819	0.65	0.636
Eror	18	5.0522	0.2807		
Total	26	21.6076			

Based on the ANOVA results, it is known that the plastic:asphalt composition has a very significant effect on the mechanical properties of the material with a p-value of 0.000, while the melting temperature also has an effect but at a lower level of significance, namely with a p-value of 0.013. Although both are below the significance threshold of 0.05, the smaller p-value indicates that the plastic:asphalt composition has a more dominant influence on the results compared to the melting temperature. Meanwhile, the interaction between the two factors resulted in a p-value of 0.636, which is not significant. This indicates that the influence of each factor on the material properties is independent, or does not affect each other. Additionally, the interaction graph between the melting temperature variable and the HDPE plastic:liquid asphalt mixture composition on the material's maximum tensile strength value is shown in Figure 7.

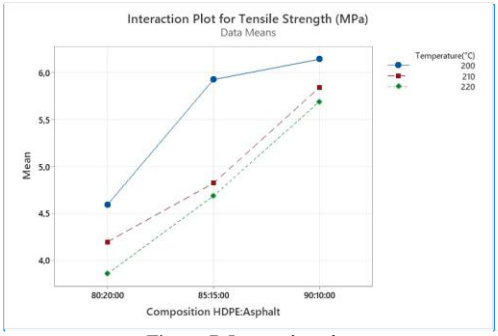

Figure 7. Interaction plot

Commented [NK1]: Please use English

Based on the interaction plot graph, it can be concluded that the higher the plastic composition in the plastic:asphalt mixture, the maximum tensile strength increases consistently across all melting temperature variations. This indicates that the plastic:asphalt composition has an effect on improving the mechanical properties of the material. Meanwhile, for the melting temperature factor, it is observed that 200°C produces the highest tensile strength, followed by 210°C, and the lowest at 220°C. This pattern indicates that an increase in melting temperature actually reduces the material's tensile strength, likely due to thermal degradation or a decrease in the integrity of inter-component bonds at extremely high temperatures. The three lines do not intersect, confirming that there is no significant interaction between composition and temperature, and each factor can be analyzed independently, as also demonstrated by the ANOVA results.

Figure 8 shows the relationship between variations in melting temperature and the maximum tensile strength of specimens made from a mixture of liquid asphalt and recycled HDPE plastic. There is a decrease in tensile strength as the melting temperature increases. A melting temperature of 200°C produces the highest average tensile strength, which is around 5.57 MPa. However, when the temperature is increased to 210°C and 220°C, the tensile strength decreases to around 4.95 MPa and 4.75 MPa, respectively. This pattern indicates that mixing at too high a temperature tends to reduce tensile strength, due to thermal degradation of the material. Thus, a melting temperature of 200°C can be considered the optimal condition for producing the best tensile mechanical properties in the material.

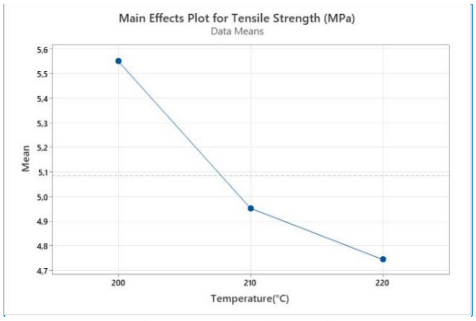

Figure 8. Main effects plot

Figure 9 illustrates the effect of varying the composition of recycled HDPE plastic mixed with liquid asphalt on maximum tensile strength.

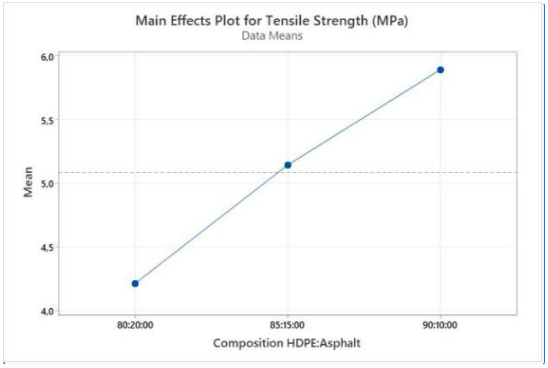

Figure 9. Main effect plot tensile strength

It can be seen that the higher the percentage of plastic in the mixture, the greater the tensile strength produced. At a composition of 80:20 (plastic:asphalt), the average tensile strength obtained is around 4.2 MPa. This value increases significantly to approximately 5.2 MPa at a composition of 85:15, and reaches a maximum value of approximately 5.9 MPa at a composition of 90:10. These results indicate that increasing the proportion of plastic in the mixture can enhance the mechanical properties of the material, particularly tensile strength, as HDPE plastic tends to provide better tensile strength compared to liquid asphalt.

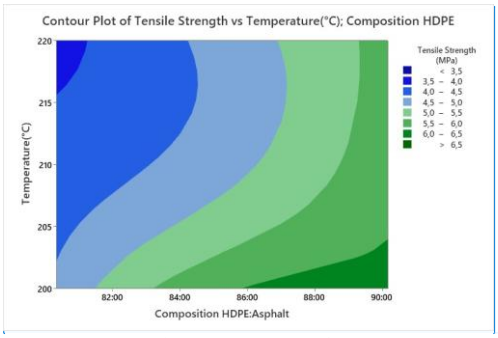

Figure 10. Contour plot

Figure 10 presents a contour plot illustrating the influence of the interaction between melting temperature and plastic:asphalt composition on the maximum tensile strength (MPa). From the color gradient pattern on the graph, it can be seen that the highest tensile strength is achieved in areas with high plastic composition (close to 90:10) and lower melting temperatures (around 200°C). The dark green color indicates zones with tensile strength greater than 6.0 MPa, which are consistently found in that area. Conversely, in regions with high temperatures (approaching 220°C) and low plastic content (around 80:20), the blue color dominates, indicating tensile strength below 4.0 MPa. When compared to pure asphalt, which typically has tensile strength values in the range of 1–2 MPa as reported by [14], the tensile strength of the HDPE–asphalt composites in this study is significantly higher. These results indicate that there is a significant interaction between the two independent variables in determining the mechanical properties of the material. Excessively high melting temperatures tend to reduce tensile strength, especially if not balanced by adequate plastic content. Therefore, the optimal combination for achieving the best tensile strength is at low temperatures and high plastic composition.

4. CONCLUSION

The following conclusions can be drawn from the research conducted:

1) The melting temperature of HDPE has a significant effect on the tensile strength of the material. A temperature of 200°C produces the highest tensile strength value, while at a temperature of 220°C the tensile strength value decreases. This indicates that increasing the melting temperature above 210°C causes a decrease in tensile strength, likely due to thermal degradation of the material.
2) The composition of the mixture between recycled HDPE plastic and liquid asphalt also affects the tensile strength value. A composition of 90% HDPE and 10% liquid asphalt produces the highest tensile strength compared to other compositions. This means that the higher the percentage of HDPE in the mixture, the greater the tensile strength produced.
3) The best combination in this study was found in the 90:10 (HDPE:asphalt) composition at a melting temperature of 200°C, yielding an average tensile strength value of 6.14 MPa. Meanwhile, the lowest combination was found in the 80:20 composition at a temperature of 220 °C, with an average value of 3.86 MPa.

5. ACKNOWLEDGEMENT

Our gratitude goes to the production and maintenance mechanical engineering study program of the Malang State Polytechnic for the support and facilities that have been provided during testing, data collection and completion of this report.

6. REFERENCES

[1] B. Wajdi, S. Sapiruddin, B. Novianti, and L. Zahara, “Pengolahan sampah plastik menjadi bahan bakar minyak (bbm) dengan metode pirolisis sebagai energi alternatif,” Kappa J., vol. 4, no. 1, pp. 100–112, 2020, doi: 10.29408/kpj.v4i1.2156.
[2] P. G. C. Nayanathara Thathsarani Pilapitiya and A. S. Ratnayake, “The world of plastic waste: A review,” Clean. Mater., vol. 11, no. January, p. 100220, 2024, doi: 10.1016/j.clema.2024.100220.
[3] W. Dhamayanthi, R. P. Ya, D. K. Wardani, P. Andini, and H. Ahmad, “Pemanfaatan HDPE (High Density Polyethylene) menjadi produk komersial pada KWT Meuseuraya Sidoarjo,” SEJAGAT: Jurnal Pengabdian Masyarakat, vol. 1, no. 2, pp. 47–55, 2024, doi: 10.25047/sejagat.v1i2.5143.
[4] F. E. Poerwodihardjo and F. Setiabudi, “Perbandingan penggunaan limbah plastik HDPE, limbah plastik PP dan lateks terhadap aspal penetrasi 60/70,” Teodolita Media Komunkasi Ilm. di Bid. Tek., vol. 23, no. 1, pp. 90–101, 2022.
[5] I. Nofriandi, W. Alamsyah, and E. N. Lydia, “Studi penambahan variasi campuran plastik jenis HDPE pada campuran aspal penetrasi 60/70 untuk lapis aus AC-WC,” J. Tek. Sipil, vol. 12, no. 2, pp. 116–123, 2023, doi: 10.24815/jts.v12i2.31207.
[6] S. Sumiati, M. Mahmuda, and A. Syapawi, “Perkerasan aspal beton (AC-BC) limbah plastik HDPE yang tahan terhadap cuaca ekstrem,” Constr. Mater. J., vol. 1, no. 1, pp. 1–11, 2019, doi: 10.32722/cmj.v1i1.1322.
[7] H. Adeswastoto and M. Islah, “Analisis jenis kerusakan pada bangunan perumahan,” J. Tek. Ind. Terintegrasi, vol. 2, 2018.
[8] Silvia Sukirman, “Beton Aspal Campuran Panas, 3rd ed.” Bandung: Institut Teknologi Nasional, 2016.
[9] A. Latif and A. Setiawan, “Pengaruh penambahan plastik High Density Polyethylene (HDPE) dan Low Density Polyethylene (LDPE) terhadap karakteristik campuran aspal AC-WC menggunakan metode kering,” Sainteks, vol. 20, no. 2, pp. 153–165, 2023, doi: 10.30595/sainteks.v20i2.17200.
[10] B. Afriyanto, E. W. Indriyati, and P. Hardini, “Pengaruh limbah plastik Low Density Polyethylene terhadap karakteristik dasar aspal,” J. Transp., vol. 19, no. 1, pp. 59–66, 2019, doi: 10.26593/jt.v19i1.3263.59-66.
[11] W. T. Putra, “A Zenk Galvalum Analisa kekuatan tarik Seng Galvalum terhadap beban yang di berikan,” Mach. J. Tek. Mesin, vol. 5, no. 1, pp. 9–14, 2019, doi: 10.33019/jm.v5i1.767.

[12] D. Fauzy, A, Metodologi Penelitian: Metodologi Penelitian, no. March. 2022. [Online]. Available: https://www.researchgate.net/publication/380362452_METODOLOGI_PENELITIAN
[13] American Society for Testing and Materials D638, "ASTM D638-14, Standard practice for preparation of metallographic specimens," ASTM Int., vol. 82, no. C, pp. 1–15, 2016, doi: 10.1520/D0638-14.1.
[14] L. Bao, M. He, S. Wang, and X. Wu, "Study on the effect of asphalt static conditions on the tensile properties of acidic aggregate hydraulic asphalt concrete," Materials, vol. 17, no. 11, p. 2627, 2024.

LOGIC
Journal of Engineering Design and Technology
Vol. 25 No.3 November ; p. 156-168

p-ISSN : 1412-114X
e-ISSN : 2580-5649
http://ojs2.pnb.ac.id/index.php/LOGIC

DESIGN OF INTEGRATED DISTILLATION-DEHYDRATION PROTOTYPE FOR BIOETHANOL WITH FLEXIBLE COLUMN AND CAPILLARY CONDENSER

Mustofa [1)*], Siradjuddin Haluti [1)], Ovin Daud [1)]

1) Agricultural Machinery and Equipment Department, Politeknik Gorontalo, Gorontalo

Correponding email [1)] : mustofa@poligon.ac.id

Abstract. The production of high-purity bioethanol remains a challenge, particularly when the feedstock originates from traditional fermentation processes such as *cap tikus*. This study presents an integrated distillation–dehydration prototype that enables simultaneous vapor separation and moisture removal within a single columnn – an innovation that combines a flexible dual-layer adsorbent chamber and a capillary-type condenser tio improve mass and heat transfer performance. The prototype consists of three main components: a boiler with a diameter and height of 500 mm, a distillation–dehydration column with a diameter of 101.6 mm and a height of 1000 mm designed for flexibility to accommodate various adsorbents, and a shell-and-tube condenser 1200 mm long equipped with 19 capillary tubes of 8 mm diameter. Heat is supplied by a "1000-eye" gas burner that ensures uniform thermal distribution at the boiler base. Preliminary testing with 10.8 L of *cap tikus* (25% alcohol) produced 94 mL of distillate in 3 hours, with a stable of 5 °C temperature gradient along the column. The resulting distillate reached alcohol 87% purity, demonstrating the capability of the integrated system to enhance dehydration performance. Despite performance limitations caused by heat losses in the boiler and vapor-flow resistance witihn the zeolite-packed column, theprototype shows promising thermal and separation characteristics and is ready for futher optimization to increase distillation rate and energy efficiency.

Keywords: Bioethanol, Capillary Tube Condenser, Distillation-Dehydration, Flexible Column, Prototype Design

1. INTRODUCTION

Indonesia continues to strengthen the development of renewable fuels, including bioethanol, as part of its national energy diversification strategy. Government programs targeting E5–E10 gasoline blends indicate a growing demand for fuel-grade ethanol, yet national production capacity remains limited due to constraints in technology readiness and feedstock availability [1]-[5]. Traditional fermentation products such as *cap tikus* represent a potential local ethanol source; however, they typically contain only 20–38% ethanol before purification, with some samples reported at below 25% [6]-[8]. These concentrations are far from the >95% purity required for fuel applications, indicating the need for effective purification technologies suited to decentralized or small-scale processing contexts. Conventional distillation is widely used to increase ethanol concentration, but thermodynamic limitations prevent separation beyond the azeotropic point (~90-95%), making an additional dehydration step essential [3]. Adsorptive dehydration using zeolite (particularly zeolite 3A) has been shown to efficiently remove residual water from ethanol due to its highly selective pore structure [9]-[12]. Recent reviews emphasize that adsorption remains one of the most effective pathways for producing fuel-grade ethanol, and new advancements continue to strengthen its role in integrated separation systems [4], [5]. Despite this, most studies treat distillation and adsorption as separate units, requiring multiple stages and introducing additional thermal losses.

To address these inefficiencies, integrated distillation-adsorption systems have been proposed, offering reductions in equipment count, energy consumption, and heat loss by combining vapor generation and dehydration within the same column [13], [14]. However, such integrated configurations remain underexplored, particularly for local feedstocks such as *cap tikus*, and few studies have evaluated column temperature gradients, vapor–adsorbent mass-transfer behavior, or distillation efficiency under practical operating conditions. Previous work on single-column reflux distillation for *cap tikus* achieved ethanol purities of only ~96-96.5% without a dehydration unit [8], indicating the need to incorporate an adsorptive medium directly within the column. Furthermore, optimization of column configuration, zeolite density, and operating temperature has been shown to significantly influence the achievable bioethanol purity in integrated systems [12]. Despite this, the application of simultaneous distillation-dehydration to traditional fermentation feedstocks like *cap tikus* remains rarely reported, particularly with respect to yield performance, final purity, and energy consumption [15].

Another key design consideration relates to the heating system. While many laboratory-scale distillation studies rely on electric heaters or industrial thermal systems, LPG-based gas burners offer practical advantages for small-scale and rural applications, including lower operating costs, rapid heating response, and easier temperature control [16]-[18]. Nevertheless, their effectiveness depends strongly on boiler geometry, heat distribution, and thermal insulation, all of which influence vapor formation and stability. Studies on small-scale distillation columns further indicate that thermal boundary conditions and wall heat losses can significantly impact separation performance, potentially reducing vapor flow rate and adsorption effectiveness when not properly managed [7]. Based on these gaps, this study focuses on the design and construction of a laboratory-scale integrated distillation-dehydration system equipped with a flexible dual-layer adsorbent chamber and a capillary-type condenser. The measurable objectives of this research are: (1) to design a practical, low-cost prototype capable of increasing ethanol purity from low-concentration feedstock such as *cap tikus* through a single-column distillation–adsorption mechanism; and (2) to evaluate its preliminary performance, including distillate purity, temperature profile behavior, and distillation rate under gas-fired operation. This prototype is expected to serve as a foundation for optimizing integrated separation systems and supporting the development of decentralized bioethanol production technologies in Indonesia.

2. METHODS

This study was carried out through four main stages: design specification, instrument identification, prototype fabrication, and preliminary performance testing. The overall research flow is shown in Figure 1. Functional criteria were established to ensure that each subsystem (boiler, column, condenser) performed within its expected operational limits before the prototype was evaluated. These criteria included: (i) steady steam flow from the boiler to the column without leaks; (ii) the condenser outlet temperature was maintained below 30 ºC; (iii) no leaks at any connections; (iv) cooling water flowed through each capillary tube gap without leaks entering the tube; and (iv) initial distillate was produced within a reasonable heating time (<40 minutes). If one or more of these criteria were not met, the fabrication phase was repeated to correct the identified issues.

2.1 Materials and Tools

The essential materials and tools used for developing the prototype are summarized in Table 1. The table presents only essential components of the integrated distillation–dehydration prototype, including the main structural elements, measurement instruments, heating and cooling systems, and fabrication tools. Listing these items with their key specifications provides a clear overview of the physical resources required for prototype construction and ensures replicability for future studies.

Table 1. Materials and Tools

Category	Item/Instrument	Key Specifications
Main Components	Stainless steel boiler	Ø 500 mm; height 500 mm; SS 304; conical top
	Distillation–dehydration column	Ø 101.6 mm; height 1000 mm; SS 304; two adsorbent chambers
	Capillary condenser	Shell Ø 101.6 mm; length 1200 mm; 19 tubes (Ø 8 mm); SS 304
	Support frame	HSS iron; welded
Adsorbent	Zeolite 4A	Granular; 100 g x 2 layers
Heating System	LPG “1000-eye” burner	Multi-flame; adjustable valve
Cooling System	Water tank + hoses	150 L; ambient cooling
	Water pump	DB-125; max. capacity: 27 L/minute; suction height: 8 m
Measurements	Thermometer (T1, T2)	WIPRO Bimetal Thermometer; Range 0-100 ºC; Ø 76.2 mm

Category	Item/Instrument	Key Specifications
	Alcoholmeter	Allafrance Alcoholmeter; 0-100%; accuracy ±2; calibration temperature: 20 ºC
	Distillate container	Erlenmeyer Pyrex; 1000 mL
	Stopwatch	Smartphone timer
	Pressure gauge	0-350 psi (0-25 bar)
Fabrication Tools	SMAW welding machine	For frame and component welding
	Grinder, drill, cutter	Metal fabrication tools

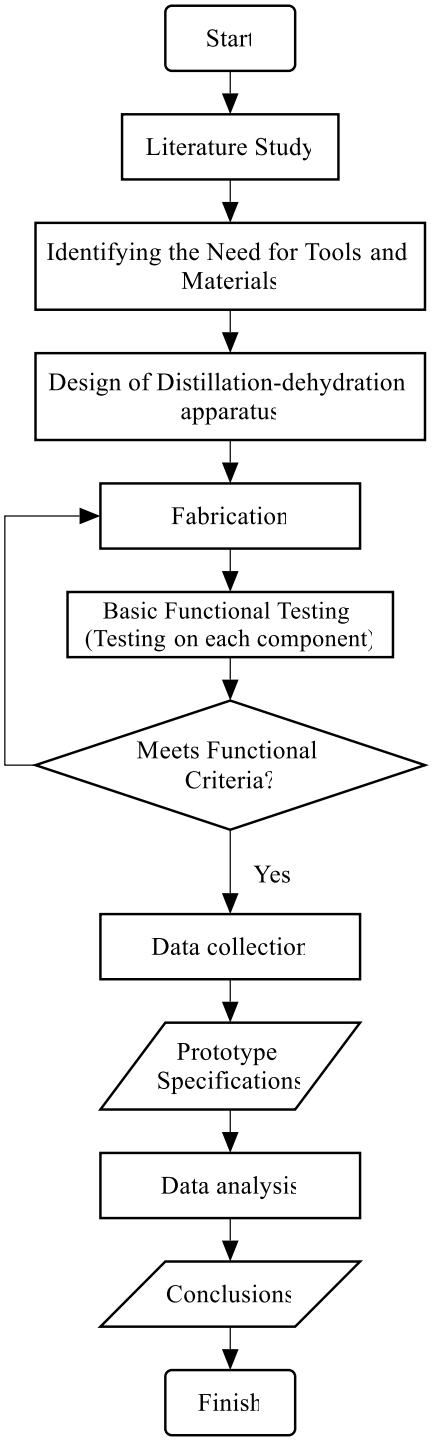

Figure 1. Research flowchart

2.2 Design of Distillation-Dehydration System

The conceptual and dimensional design of the apparatus was developed using Microsoft PowerPoint 2024, which served as a 2D schematic drafting tool for generating scaled engineering layouts. Although PowerPoint is not a conventional CAD platform, it enables precise manipulation of geometric elements, allowing all principal dimensions – such as boiler diameter, column height, condenser length, and capillary-tube arrangement – to be defined manually based on predetermined measurements. As the objective of this study was prototype construction rather than computational simulation or tolerance-critical machining, the schematic-based approach was sufficient to represent the structural configuration and spatial relationships among components. The final prototype dimensions were validated during assembly, confirming that the drafting method adequately supported the accuracy required for the development of a functional laboratory-scale distillation–dehydration system.

2.3 Fabrication

The distillation-dehydration apparatus was fabricated at the Welding Laboratory of the Agricultural Machinery and Equipment Study Program, Politeknik Gorontalo. The fabrication process included the construction of the boiler, column, and condenser installation using stainless steel welding techniques. Fittings, valves, and connectors were installed to ensure the system's operational flexibility and ease of maintenance. Before operation, a functional test was conducted on each component, particularly the boiler, distillation-dehydration column, condenser, and cooling water circulation system. This test aimed to check for leaks in these components and ensure there was no steam/water loss at the connections.

2.4 Determination of Distillation-Dehydration Equipment Specifications

The specifications of the distillation–dehydration apparatus were determined by analyzing process requirements related to target ethanol purity, batch feed capacity, and thermal efficiency. Literature data and basic thermodynamic estimations were used to define the necessary boiler volume, column dimensions, and condenser heat-transfer area. Material selection and structural flexibility were prioritized to ensure compatibility with multiple adsorbents and repeated laboratory use. The column was therefore designed with removable adsorbent compartments to support testing under different dehydration configurations. Overall, the resulting specifications were formulated to produce an efficient and adaptable system suitable for processing ethanol from traditional fermentation feedstocks.

2.5 Operating Parameters

The operating parameters applied during the initial performance test of the prototype are presented in Table 2. These parameters describe the thermodynamic conditions, feed characteristics, adsorbent configuration, and output variables measured during a 3-hour distillation–dehydration run. The summarized values provide a quantitative basis for assessing the system's functional behavior and identifying factors influencing vapor generation, mass transfer, and distillate yield.

Table 2. Operating Parameters of Distillation-Dehydration System

Parameter	Value/Condition
Feed volume	10.8 L *cap tikus*
Initial alcohol content	25% v/v
Heating source	LPG "1000-eye burner"
Average boiler temperature	78-80 ºC
Column temperatures	T1 ≈ 80 ºC; T2 < T1
Cooling-water temperature	< 30 ºC
Adsorbent mass	100 g x 2 layers (Zeolite 4A)
Time opeartion	180 minutes

2.6 Data Analysis Technique

The analysis of experimental data in this study was carried out through a structured procedure encompassing data processing, performance evaluation, and measurement validation. Temperature data recorded at the lower (T1) and upper (T2) sections of the column were collected at 5-minute intervals and subsequently plotted as time–temperature profiles to observe heating dynamics, thermal stabilization, and column temperature gradients throughout the distillation–dehydration process. Distillate production was monitored by measuring the cumulative volume collected during the 3-hour operation, enabling calculation of the distillation rate in mL/h. The ethanol concentration of the distillate was determined using a calibrated alcoholmeter to quantify purification effectiveness.

3. RESULTS AND DISCUSSION

3.1 Bioethanol Distillation-Dehydration Equipment Specifications

The design of the tool is carried out by determining the functional specifications of the distillation-dehydration tool equipped with several components as presented in Figure 2. The bioethanol distillation-dehydration tool series consists of: (1) a boiler tube that functions as a heating place for the cap tikus feed to produce ethanol vapor, (2) a feed input pipe to enter liquid raw materials, (3) a manometer to monitor the pressure in the boiler, (4) a thermometer to measure the operating temperature, (5) a distillation-dehydration column filled with zeolite 3A as an adsorbent, (6) a condenser to cool the vapor into a liquid distillate, (7 and 8) circulating water that enters and exits through the condenser for the condensation process, (9) a water reservoir as a source of coolant circulation, (10) a water pump to maintain a continuous flow of coolant circulation, and (11) a gas stove as the main heat source. This design allows the distillation and dehydration processes to take place simultaneously, so that the system is simpler in increasing the ethanol content in the raw materials. Among these components, the distillation-dehydration column and condenser are very important components in increasing the ethanol content.

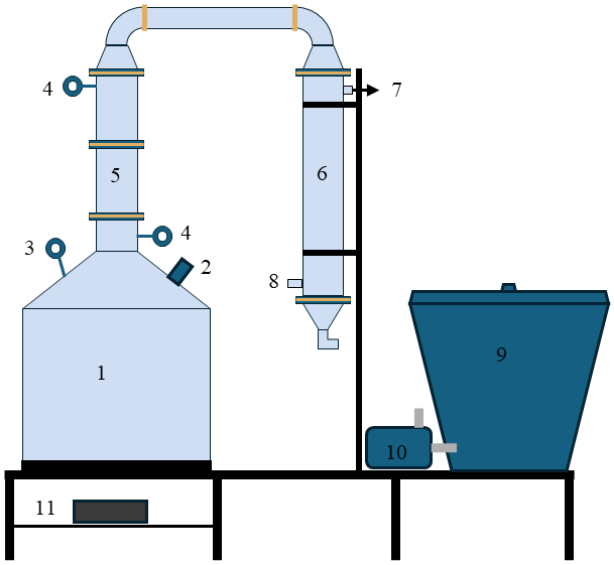

Information:
1. Boiler tube
2. Feed/raw material input
3. Manometer
4. Thermometer
5. Distillation-dehydration column
6. Condenser
7. Water outlet pipe
8. Water inlet pipe
9. Water reservoir
10. Water pump
11. Gas stove

Figure 2. Design of bioethanol distillation-dehydration equipment

The distillation-dehydration column is designed in a vertical cylindrical shape equipped with an internal chamber to accommodate the adsorbent material (Figure 3(a)). The placement of the adsorbent in this column aims to improve the separation process, especially in the ethanol dehydration stage, by utilizing the selective properties of the adsorbent material towards water molecules. The condenser is designed with a double pipe system (shell and tube) consisting of a number of small pipes on the inside and one large pipe as the outer sheath (Figure 3(b)). The small pipes function as a flow path for the distilled ethanol vapor which then undergoes a cooling process so that it condenses into a liquid phase. Meanwhile, cooling water flows through the large pipe on the outside, filling the gaps around the small pipes, so that heat transfer occurs efficiently. The working principle of this condenser is based on the forced convection mechanism of the cooling water flow and heat conduction through the pipe walls, which results in a decrease in the temperature of the ethanol vapor to its condensation point.

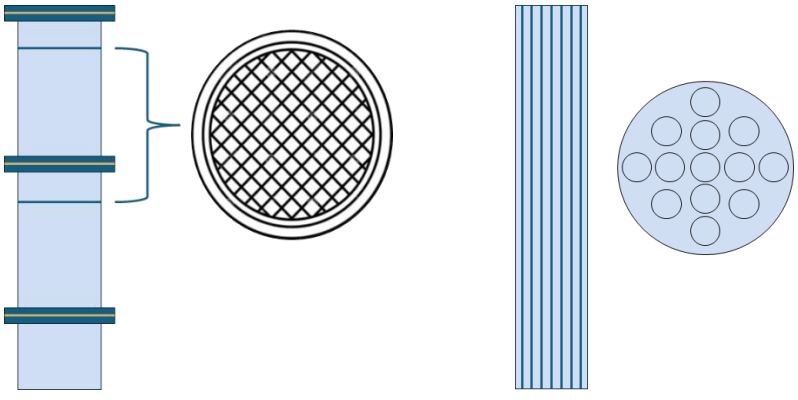

(a) (b)

Figure 3. Main component design: (a) distillation-dehydration column and (b) condenser

A bioethanol distillation-dehydration equipment has been successfully designed and fabricated with the primary goal of producing high-purity ethanol. The design integrates the distillation and dehydration processes in a single column, reducing the need for additional equipment while minimizing heat loss. The apparatus's working principle is based on heating the raw material, cap tikus, which has a relatively high ethanol content. Evaporation and separation of the ethanol-water mixture occur in a column containing 4A zeolite adsorbent, and recondensation of the ethanol vapor occurs through a water-cooled condenser. The apparatus's configuration is compact, utilizing a metal support frame for stability and ease of operation on a laboratory scale. The design of the distillation-dehydration apparatus can be seen in Figure 4. The energy source used to heat the raw material is a gas stove.

The bioethanol distillation-dehydration tool designed in this research consists of several main components with the following technical specifications:

1. Main/Support frame
   This frame (Figure 4) serves as a base for the boiler, motor, and reservoir, as well as a condenser support. The main frame measures 1750x520 mm, with a height of 300 mm from the bottom of the boiler base. The lower part of the main frame is made of angle iron, while the condenser support is made of hollow iron coated with anti-rust paint for increased durability.
2. Boiler
   The vertical cylindrical boiler (Figure 5) is made of 304 grade stainless steel with a plate thickness of 2 mm. This material was chosen for its resistance to corrosion and chemical reactions with ethanol. This boiler has a diameter of 500 mm and a height of 500 mm, thus the boiler can hold a maximum liquid material capacity of 98.125 L. The boiler is equipped with a feed inlet for entering liquid raw materials (mouse cap), as well as a steam outlet connected to the distillation column and the distillation residue outlet.
3. Distillation-dehydration column
   The column is a vertical cylindrical tube (Figure 6(a)) made of 304 stainless steel with a diameter of 101.6 mm and a height of 1000 mm. The inside of the column is equipped with a filling chamber of 3 mm particle size zeolite 3A adsorbent, with a maximum filling capacity of 500 grams for each section. This column is designed to be able to perform two functions simultaneously, namely distillation to separate ethanol from water based on boiling point, and dehydration to absorb water molecules using zeolite. The column structure consists of several segments that can be removed to facilitate filling and replacing the adsorbent. This design also allows the flexibility of using various types of adsorbent materials, such as zeolite or porous geopolymer, according to research needs. The steam flow will come into direct contact with the adsorbent layer so that the water content in the ethanol can be reduced, producing ethanol with a higher purity. With this design, the column not only functions as a separation medium based on boiling point, but also integrates an adsorption mechanism as a dehydration stage.

Figure 4. Design results of bioethanol distillation-dehydration equipment

Figure 5. Boiler design

4. Condenser
   The condenser (Figure 6(b)) is designed using a shell and tube type design with a total length of 1200 mm and an outer diameter of 101.6 mm. There are 19 stainless steel pipes on the inside with a diameter of 10 mm each, where the ethanol vapor is flowed and then condensed. Cooling water is flowed in the opposite direction (counter-current flow) through the outer space of the pipe which is circulated by a water pump. The multi-pipe design on the inside allows for an increase in the heat transfer surface area, so that the condensation efficiency becomes more optimal [19]-[21]. This is because it allows an increase in the heat transfer surface area, so that condensation is more effective, thermal resistance is reduced, and the operating temperature is stable [22]. With this design, the ethanol vapor coming out of the distillation column can be condensed quickly and stably, producing ethanol liquid with a purity that meets the target dehydration process.
5. Water reservoir tank
   The tank, made of polyethylene (PE) (Figure 7), has a total volume of 150 L and serves as a reservoir for cooling water that is circulated to the condenser. Water from this reservoir is circulated to the condenser using a water pump with a maximum capacity of 27 L/minute and 200 Watts of electrical power.

(a) (b)

Figure 6. Component design: (a) distillation-dehydration column and (b) condenser

Figure 7. Water tank and pump

6. Heat source
   The heat used for evaporation of the raw materials is a gas stove with a "1000 eye" stove specification (Figure 8). The use of the "1000 eye" type gas stove was chosen as the main heat source for the 50 cm diameter boiler because it is able to produce an even flame distribution across the entire surface of the tube base. The multi-burner design of this stove allows heat to be distributed homogeneously, thereby minimizing temperature gradients and speeding up the heating process. With a relatively high combustion power, this type of gas stove is suitable for large-capacity boilers that require significant thermal energy to evaporate the fermentation solution.

Figure 8. Stove “1000 eyes”

In addition to heat distribution, the use of a gas stove offers advantages in terms of operational flexibility and energy costs. This system does not require a high-power electrical installation like resistive heaters, and is easier to operate in both laboratory and field conditions. Heat transfer efficiency can be increased by adjusting the distance between the flame and the boiler base, allowing for more controlled gas consumption without reducing the distillation rate. Therefore, the "1000-eye" gas stove is a practical and economical alternative for heating in the design of bioethanol distillation-dehydration equipment.

3.2 Discussion

Design and Construction of the Bioethanol Distillation–Dehydration System

The bioethanol distillation-dehydration apparatus is designed with special designs for several main components, such as the distillation-dehydration column and condenser. The designed distillation-dehydration column has a length of 1000 mm and a diameter of 101.6 cm so that it provides an adequate height-to-diameter (H/D) ratio for vapor-liquid phase separation and adsorptive interactions in the vapor-upflow. Modern packed bed design studies have shown that column geometry (H/D) and filling distribution have a significant effect on the pressure drop and contact profile between the gas and solid phases, which in turn determine the mass transfer efficiency in adsorptive/distillative applications [23], [24]. Zeolite is a superior adsorbent in separation technology because its microporous structure allows high selectivity towards water molecules in ethanol-water mixtures. Recent studies have confirmed that optimizing the use of zeolites can replace conventional energy-intensive separation methods, making them more sustainable [25]. Therefore, this column is designed with two adsorbent holding chambers (one at the bottom and one at the top) to avoid the accumulation of adsorbent mass at one point and to maintain the

porosity distribution along the bed, thereby reducing the risk of channeling and unwanted vapor flow reduction [26]. Thus, this design can expand the vapor-adsorbent contact so that the dehydration efficiency is increased according to the principle of zeolite-based separation optimization.

On the other hand, the dimensions and position of the distillation-dehydration column structure play a role in the evaporation mechanism and vapor contact with the adsorbent. Research on scaling up adsorption columns [27] shows that column dimensions, especially diameter and height, affect the saturation time, residence time, and volume of solution that can be processed, while the adsorption capacity remains relatively constant. This is in line with the design of the distillation-dehydration column in this study, where the vertical configuration was chosen to maximize the contact between the ethanol-water vapor and the zeolite layer. Meanwhile, a modeling study of a gas adsorption column [28] confirmed that the adsorption dynamics can be accurately predicted using a 1-D pseudo-homogeneous approach, which is also relevant to analyzing the adsorption behavior of ethanol vapor in a vertical column. Thus, the design of the distillation-dehydration column used is not only supported by empirical considerations, but also in accordance with theoretical approaches in the literature.

Another key component that plays a significant role in this system is the condenser. The condenser design in this study has an outer diameter of 10.16 cm and a length of 120 cm, with 19 capillary tubes of 0.8 cm diameter inside, providing an internal heat transfer surface area of approximately 0.57 m2 from the capillary tubes alone. This capillary structure increases the internal heat transfer coefficient by reducing the condensate film thickness and increasing the turbulence of the vapor flow relative to the tube surface, resulting in a faster and more efficient condensation process. Previous research related to shell-and-tube condensers has shown that increasing the number of tubes and reducing the tube diameter can significantly increase the heat transfer rate and condensation effectiveness [29]. In addition, long vertical condenser tubes with optimized surface structures result in an increase in the condensation coefficient of up to 20-60% compared to similar plain tubes [30]. With this configuration, the condenser design in the bioethanol distillation-dehydration apparatus is expected to produce a more stable condensate product and prevent vapor from escaping without being adequately condensed.

Preliminary Performance Evaluation and Analysis of Factors Affecting Process Efficiency

Based on the preliminary testing results, a total of 10,800 mL of Cap Tikus (alcohol 25% v/v) was introduced into the boiler, and the corresponding data are presented in Figure 9. The figure of experimental results shows the variation of temperatures at the lower (T1) and upper (T2) parts of the column throughout the distillation–dehydration process, with data recorded at 5-minute intervals. During the initial phase (0-34 minutes), both T1 and T2 gradually increased toward the boiling point of ethanol, as indicated by the appearance of the first distillate droplet at 34 minutes. Once the system reached the operational phase (≥ 40 minutes), T1 stabilized at approximately 86 ºC and T2 at around 81 ºC, with an average temperature difference of about 5 ºC. This condition indicates the formation of a consistent temperature gradient within the column, which is essential for effective vapor separation and adsorption. Nevertheless, the total distillate volume obtained after 3 hours of heating was only 94 mL, indicating limited heat and mass transfer efficiency within the system that requires further optimization.

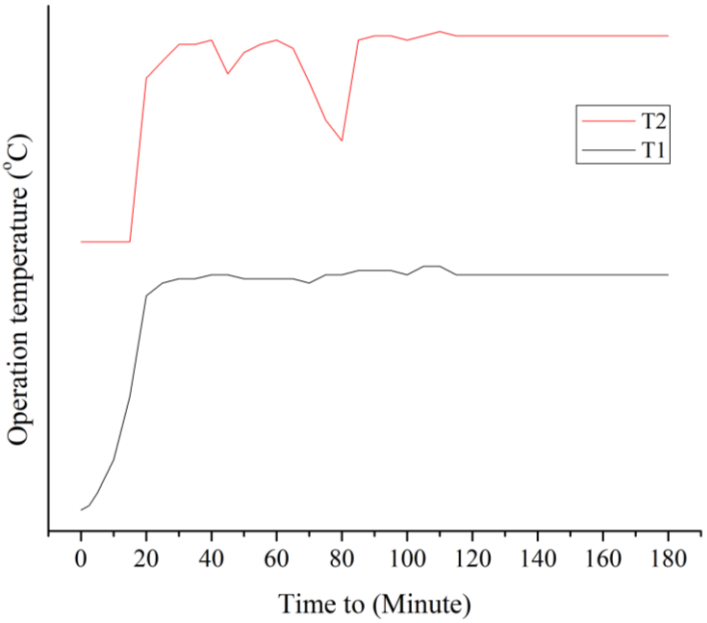

Figure 9. Time versus temperature of distillation-dehydration process

The flow of ethanol vapor from the boiler to the condenser required approximately 15 minutes from the onset of boiling (t = 00:20:00, T1 = 81 °C, and T2 = 71 °C) until the vapor condensed into liquid distillate at 34 minutes. The total distillate collected over 3 hours was 94 mL, equivalent to 31.3 mL/h (or approximately 38.7 mL/h when calculated from the first drop), indicating a relatively low effective vapor rate compared to the feed volume. While the condenser temperature was maintained low and stable at 26 °C, the main limitation is presumed to lie in heat transfer within the boiler, including losses by conduction, convection, and radiation due to insufficient insulation and non-uniform flame distribution. Previous studies have reported that vapor flow resistance in packed columns increases with higher adsorbent density and uneven flow distribution, leading to reduced vapor velocity and product throughput [31,32]. Moreover, thermal conditions of the column wall significantly influence separation performance, as heat losses may trigger premature condensation and internal reflux, hindering vapor transport toward the condenser [33]. This phenomenon is consistent with the experimental findings showing a temperature gradient of about 5 °C between the lower and upper sections of the column, indicating that mass transfer occurred but was not yet optimal. Furthermore, column performance simulations have demonstrated that non-idealities arising from mass transfer resistance must be considered in design and analysis, as they directly affect separation efficiency and temperature distribution along the column [34].

The distillation–dehydration column design with a total height of 1000 mm in this study provides a sufficient residence time for ethanol vapor to interact with the adsorbent layers. However, the total height of the zeolite bed, approximately 30 mm (3 cm), remains relatively low, thereby limiting the adsorption capacity and accelerating the occurrence of breakthrough. Several studies have shown that increasing the bed height to 4-5 cm can significantly extend the breakthrough time and enhance adsorption capacity, although this must be balanced with an appropriate control of the vapor flow rate to prevent excessive flow resistance [35-37]. Furthermore, both the vapor flow rate and initial vapor concentration play important roles, as higher values tend to accelerate adsorbent saturation due to shorter contact times and increased mass loading [38].

Another critical aspect influencing the quantity of bioethanol produced is the headspace ratio within the boiler. A low liquid filling ratio leads to a significant portion of the thermal energy being dissipated to heat the gas in the upper space, thereby reducing heat transfer efficiency and delaying the establishment of stable vapor formation. The overall thermal system efficiency increases only up to an optimum point before declining due to ineffective heat distribution [39]. In addition, experimental results have shown substantial heat loss in columns with a high surface-area-to-volume ratio, which reduces the actual vapor load [40]. A large headspace volume also tends to produce non-uniform vapor flow patterns and increases the likelihood of internal condensation along the column wall or within the adsorbent bed, causing part of the vapor to revert to liquid before reaching the condenser [41,42]. These conditions necessitate an optimal headspace ratio to balance heat transfer efficiency to the liquid phase and vapor expansion space, thereby improving the evaporation rate. Therefore, in the preliminary test case (boiler filled at approximately 10.8% of its total volume), the low product volume (94 mL over 3 hours) indicates heat losses and vapor formation inefficiency resulting from the excessive headspace. Determining the optimal headspace ratio is thus essential to maintain thermal efficiency, vapor flow stability, and high bioethanol productivity. Design improvements through increasing the liquid filling ratio, enhancing boiler insulation, and optimizing adsorbent configuration in the column are expected to improve the distillation rate and separation efficiency. Consequently, the overall performance of the distillation–dehydration system can be significantly enhanced through integrated control of thermal, hydrodynamic, and mass transfer characteristics.

Design improvements through increasing the liquid filling ratio, enhancing boiler insulation, and optimizing adsorbent configuration in the column are expected to improve the distillation rate and separation efficiency. Consequently, the overall performance of the distillation–dehydration system can be significantly enhanced through integrated control of thermal, hydrodynamic, and mass-transfer characteristics. In this study, despite the limited vapor production, the distillation–dehydration process successfully increased the ethanol concentration of cap tikus from 25% to 87%, demonstrating that the prototype is capable of achieving substantial purification even under suboptimal operating conditions.

4. CONCLUSION

A bioethanol distillation–dehydration prototype integrating both separation stages within a single column has been successfully designed and fabricated. The system consists of a 500 mm x 500 mm stainless-steel boiler, a 1000 mm x 101.6 mm distillation–dehydration column with flexible adsorbent compartments, and a 1200 mm capillary-type condenser containing 19 tubes of 8 mm diameter. The “1000-eye” LPG burner provided uniform thermal distribution necessary for stable vapor generation. Preliminary testing using 10.8 L of cap tikus produced 94 mL of distillate over 3 hours, with a consistent column temperature gradient of approximately 5 °C. Despite the low yield, the system successfully increased ethanol concentration from 25% to 87%, demonstrating that the integrated column effectively enhances dehydration performance even under non-optimal heating conditions. The observed limitations indicate the need for improvements in boiler insulation, liquid filling ratio, and adsorbent configuration to enhance vapor generation and separation efficiency. Overall, the prototype shows strong potential for further

optimization and serves as a foundational platform for subsequent performance validation and scale-up studies in local bioethanol production.

5. ACKNOWLEDGEMENT

The authors gratefully acknowledge the Directorate General of Research and Development, Ministry of Higher Education, Science, and Technology for funding support. The authors also thank the Laboratory of Machinery and Welding, Study Program of Agricultural Machinery and Equipment, Gorontalo Polytechnic, for providing facilities and technical assistance in apparatus fabrication and testing. Their contributions were invaluable to the successful completion of this research.

6. REFERENCES

[1] Admin, "Indonesia plans to launch 5% bioethanol mix of fuel in three years", 7 Dec. 2022. [Online]. Available: https://www.astra-agro.co.id/2022/12/07/indonesia-plans-to-launch-5-bioethanol-mix-of-fuel-in-three-years/. [Accessed: 7 Jul. 2025].

[2] Enerdata, "Indonesia starts selling gasoline with 5% bioethanol", 6 Jul. 2023. [Online]. Available: https://www.enerdata.net/publications/daily-energy-news/indonesia-starts-selling-gasoline-5-bioethanol.html. [Accessed: 7 Jul. 2025].

[3] Ibai, "Indonesia to target 10 bioethanol blend in fuel by 2030", 11 Sep. 2024. [Online]. Available: https://www.ibai.or.id/news/item/6002-indonesia-to-target-10-bioethanol-blend-in-fuel-by-2030.html/. [Accessed: 7 Jul. 2025].

[4] F. Nangoy dan B. Christina, "Analysis-Indonesia faces ethanol feedstock hurdle to repeat biodiesel success", 6 Apr. 2023. [Online]. Available: https://theprint.in/environment/analysis-indonesia-faces-ethanol-feedstock-hurdle-to-repeat-biodiesel-success/1500955/. [Accessed: 7 Jul. 2025].

[5] J. Isaac, "Aprobi urges regulatory clarity as Indonesia targets 500 bioethanol plants", 24 Apr. 2025. [Online]. Available: https://indonesiabusinesspost.com/4167/policy-and-governance/aprobi-urges-regulatory-clarity-as-indonesia-targets-500-bioethanol-plants/. [Accessed: 7 Jul. 2025].

[6] L. V. Lintong, D. Deeng dan W. E. Mamosey, "Perubahan Nilai Budaya Masyarakat Cap Tikus di desa Talaitad Utara Kecamatan Suluun Tareran Kabupaten Minahasa Selatan," *Jurnal Holistik,* vol. 15, no. 4, pp. 1-16, 2022.

[7] N. F. Tambayong, O. E. H. Laoh dan O. Porajow, "Analisis Usaha Cap Tikus di Desa Poopo Kecamatan Passi Timur Kabupaten Bolaang Mongondow," *Agr-sosioekonomi,* vol. 12, no. 2, pp. 77-86, 2016.

[8] F. Wenur dan Y. Waromi, "Studi Pengolahan Bioetanol Tradisional dari Nira Aren di Minahasa Selatan," *Jurnal Teknologi Pertanian,* vol. 8, no. 2, pp. 1-7, 2017.

[9] M. Subandriyo dan F. A. Putri, "The effect of various zeolites as an adsorbent for bioethanol purification using a fixed bed adsorption column," *International Journal of Technology,* vol. 11, no. 7, pp. 1300-1308, 2020.

[10] Khaidir, D. Setyaningsih dan H. Haerudin, "Modifikasi Zeolit Alat sebagai Material Molekular Sieve pada Proses Dehidrasi Bioetanol," *Jurnal Zeolit Indonesia,* vol. 8, no. 2, pp. 97-105, 2009.

[11] S. B. Ginting dan J. Kristian, "Ethanol Dehydration in Fixed Bed Column Using Pellet Adsorbent from Lampung Natural Zeolite," *Jurnal Rekayasa Kimia dan Lingkungan,* vol. 17, no. 1, pp. 53-63, 2022.

[12] H. Hargono, N. A. Handayani, S. D. Andani, E. Wardani, U. A. Fisama dan K. S. Seng, "Adsorption method using zeolite to produce fuel-grade bioethanol," *International Journal of Renewable Energy Development,* vol. 12, no. 4, pp. 808-815, 2023.

[13] A. Rahmanulloh, "Biofuels Annual," Foreign Agricultural Service, United States Department of Agriculture, Jakarta, 2023.

[14] Grains, "Ethanol market profiles – Indonesia", 13 May 2014. [Online]. Available: https://grains.org/bioethanol/ethanol-market-profiles/indonesia/. [Accessed: 7 Jul. 2025].

[15] Y. Sumampouw, H. S. Kolibu dan S. H. J. Tongkukut, "Pembuatan Bioetanol dengan Teknik Destilasi Refluks Satu Kolom," *Jurnal Ilmiah Sains,* vol. 15, no. 2, pp. 154-158, 2015.

[16] E. O'Rear, D. Webb, J. Kneifel dan C. O'Fallon, "Gas vs electric: Heating system fuel source implications on low-energy single-family dwelling sustainability performance," *Journal of Building Engineering,* vol. 25, no. 2019, p. 100779, 2019.

[17] Australian Energyr Upgrades, "Gas vs. Electric: Which Heating System is More Efficient?", 9 Apr. 2024. [Online]. Available: https://australianenergyupgrades.com.au/gas-vs-electric-which-heating-system-is-more-efficient/. [Accessed: 7 Jul. 2025].

[18] A. Brui, "Electric Boiler vs Gas Boiler: Which is Better?", 9 Apr. 2025. [Online]. Available: https://www.greenmatch.co.uk/boilers/compare/types/electric-vs-gas. [Accessed: 7 Jul. 2025].

[19] B. L. Rakshith(a), L. G. Asirvatham, A. A. Angeline, J. A. P. S. Raj, J. R. Bose, P. J. B. Princess, S. Gautam, O. Mahian, G. Ribatski dan S. Wongwises, "Cooling of power electronic devices using rectangular flat heat

pipes with externally and internally cooled condensor," *Applied Thermal Engineering,* vol. 236, no. Part B, p. 121474, 2024.
[20] B. L. Rakshith(b), L. G. Asirvatham, A. A. Angeline, J. P. S. Raj, J. R. Bose dan S. Wongwises, "Experimental investigation on the heat transfer performance of flat heat pipe embedded with internally cooled condensor," *International Journal of Heat and Mass Transfer,* vol. 230, no. 2024, p. 125728, 2024.
[21] P. Dong, G. Wang, W. Yu, E. Liu dan Y. Han, "Investigation on heat transfer performance of flat plate micro-heat pipe phase change heat storage/release device," *Green Energy and Resources,* vol. 2, no. 2, p. 100071, 2024.
[22] J. Jose dan T. K. Hotta, "Thermal performance analysis and optimization of a heat pipe-based electronic thermal management system using experimental data-driven neuro-genetic technique," *Thermal Science and Engineering Progress,* vol. 54, no. 2024, p. 102860, 2024.
[23] V. Jurado-Davila, J. T. De Oliveira, D. Estumano dan L. A. Féris, "Fixed-bed column for phosphate adsorption combining experimental observation, mathematical simulation, and statistics: Classical and Bayesian," *Separation and Purification Technology,* vol. 317, no. 2023, p. 123914, 2023.
[24] V. Stampi-Bombelli dan M. Mazzotti, "Exploring Geometric Properties and Cycle Design in Packed Bed and Monolith Contactors Using Temperature-Vacuum Swing Adsorption Modeling for Direct Air Capture," *Industrial & Engineering Chemistry Research,* vol. 63, no. 2024, pp. 19728-19743, 2024.
[25] E. Pérez-Botella, S. Valencia dan F. Rey, "Zeolites in Adsorption Processes: State of the Art and Future Prospects," *Chemical Reviews,* vol. 122, no. 24, pp. 17647-17695, 2022.
[26] V. Stampi-Bombelli, A. Storione, Q. Grossmann dan M. Mazzotti, "On Comparing Packed Beds and Monoliths for CO2 Capture from Air Through Experiments, Theory, and Modeling," *Industrial & Engineering Chemistry Research,* vol. 63, no. 2024, pp. 11637-11653, 2024.
[27] D. Juela, M. Vera, C. Cruzat, A. Astudillo dan E. Vanegas, "A new approach for scaling up fixed-bed adsorption columns for aqueous systems: A case of antibiotic removal on natural adsorbent," *Process Safety and Environmental Protection,* vol. 159, no. 2022, pp. 953-963, 2022.
[28] F. J. G. Ortiz, M. B. Rodríguez dan R. T. Yang, "Modeling of fixed-bed columns for gas physical adsorption," *Chemical Engineering Journal,* vol. 378, no. 2019, p. 121985, 2019.
[29] Z. Rifaldo, B. Hafid, Z. Husin, E. H. Wijayanto dan M. Idris, "Heat Transfer Analysis in Shell and Tube Type Condenser," *Journal of Mechanical Engineering, Manufactures, Materials and Energy,* vol. 8, no. 1, pp. 67-74, 2024.
[30] Z. Chen, K. Zhang dan N. Wang, "Experimental Investigation of Large-Scale Vertically Coated Tubes for Enhanced Air–Steam Condensation Heat Transfer," *Energies,* vol. 17, no. 4759, pp. 1-15, 2024.
[31] Y. Cao, H. A. Dhahad, A. Khandakar, M. E. H. Chowdury, M. A. Ayari, S. M. Alizadeh dan B. Vaferi, "Employing computational fluid dynamics technique for analyzing the PACK-1300XY with methanol and isopropanol mixture," *Scientific Reports,* vol. 12, no. 6588, pp. 1-11, 2022.
[32] A. Surmi, A. Mohd Shariff dan S. S. M. Lock, "Comprehensive Analysis of Pressure Drop Phenomena in Rotating Packed Bed Distillation: An In-Depth Investigation," *ACS Omega,* vol. 9, no. 26, pp. 28105-28113, 2024.
[33] R. Staud, K. Schroder, K. Mesarek, J. Schroder, R. Herbst, K. Jasch dan S. Scholl, "Impact of thermal column wall conditions and subcooled reflux on separation performance in miniplant distillation columns," *Separation and Purification Technology,* vol. 358, no. 2025, p. 130479, 2025.
[34] H. Poortalari, F. Varaminian dan J. Karimi Sabet, "A packed distillation column performance simulation by modified equilibrium stage model based on multicomponent packing efficiencies," *Progress in Engineering Thermodynamics and Kinetics,* vol. 1, no. 2, pp. 1-19, 2024.
[35] A. S. Kovo, S. Alaya-Ibrahim, A. S. Abdulkareem, O. D. Adeniyi, T. C. Egbosiuba, J. O. Tijani, M. Saheed, B. O. Okafor dan Y. S. Adeyinka, "Column adsorption of biological oxygen demand, chemical oxygen demand and total organic carbon from wastewater by magnetite nanoparticles-zeolite A composite," *Heliyon,* vol. 9, no. 2, p. e13095, 2023.
[36] A. Samanth, R. Vinayagam, T. Varadavenkatesan dan R. Selvaraj, "Fixed bed column adsorption systems to remove 2,4-Dichlorophenoxyacetic acid herbicide from aqueous solutions using magnetic activated carbon," *Environmental Research,* vol. 261, no. 2024, p. 119696, 2024.
[37] L. Meina, M. Qiao, Q. Zhang, S. Xu dan D. Wang, "Study on the dynamic adsorption and recycling of phosphorus by Fe–Mn oxide/mulberry branch biochar composite adsorbent," *Scientific Reports,* vol. 14, no. 1, p. 1235, 2024.
[38] S. E. Marranea, K. Dânoun, Y. Essamlali, S. Aboulhrouz, S. Sair, O. Amadine, I. Jioui, A. Rhihila dan M. Zahouily, "Fixed-bed adsorption of Pb(II) and Cu(II) from multi-metal aqueous systems onto cellulose-g-hydroxyapatite granules: optimization using response surface methodology," *RSC Advances,* vol. 13, no. 2023, pp. 31935-31947, 2023.

[39] B. Shahzamanian, S. Varga, J. Soares, A. I. Palmero-Marrero dan A. C. Oliveira, "Theoretical performance assessment of a multi-effect distillation system integrated with thermal vapour compression unit running on solar energy," *International Journal of Low-Carbon Technologies,* vol. 19, no. 2024, pp. 908-921, 2024.
[40] L. M. Ränger, Y. Waibel dan T. Grützner, "Experimental Investigation of Heat Losses in a Pilot-Scale Multiple Dividing Wall Distillation Column with Three Parallel Sections," *Chemiengineering,* vol. 7, no. 68, pp. 1-16, 2023.
[41] R. Hu, C. Duan dan Y. Lan, "Investigating the Effects of Distillation System, Geographical Origin, and Aging Time on Aroma Characteristics in Brandy Using an Untargeted Metabonomic Approach," *Foods,* vol. 13, no. 1922, pp. 1-15, 2024.
[42] N. M. Tahir, J. Zhang dan M. Armstrong, "Control of Heat-Integrated Distillation Columns: Review, Trends, and Challenges for Future Research," *Processes,* vol. 13, no. 17, pp. 1-33, 2025.

LOGIC
Journal of Engineering Design and Technology
Vol. 25 No.3 November ; p. 169-174

p-ISSN : 1412-114X
e-ISSN : 2580-5649
http://ojs2.pnb.ac.id/index.php/LOGIC

OPTIMIZATION OF PINEAPPLE LEAF FIBER-REINFORCED ABS WASTE FILAMENTS FOR FDM: EFFECT OF MESH SIZE AND VOLUME FRACTION

Azizul Fikri [1], Faiza Armalia Putri [1], Risa Nurin Baiti [2], Mhd Yasin Siregar [1], Wahyu Solafide Sipahutar [1]*

1) Department of Materials Engineering, Institut Teknologi Sumatera, Lampung
2) Department of Mechanical Engineering, Politeknik Negeri Bali, Bali

Correponding email [1] : wahyu.sipahutar@mt.itera.ac.id

Abstract. Acrylonitrile Butadiene Styrene (ABS) plastic waste presents significant potential for upcycling into environmentally friendly materials, particularly as feedstock for 3D printing filaments in Fused Deposition Modeling (FDM). This study investigates the influence of pineapple leaf fiber (PALF) reinforcement at two weight fractions (3% and 5%) and two mesh sizes (200 and 300) on the dimensional stability, printability, and mechanical properties of ABS waste-based composite filaments. Comprehensive evaluations were conducted, including filament diameter consistency, surface morphology, and uniaxial tensile testing. The 5% fiber content with 300-mesh PALF yielded the most stable filament diameter (average 1.73 mm, CV 2%), while the same formulation also achieved the highest ultimate tensile strength (UTS) of 8.873 MPa and elongation at break of 0.197%. Interestingly, the highest Young's modulus (0.139 GPa) was observed in the 3%–300 mesh variant, although it exhibited more brittle behavior. Overall, the 5%–300 mesh formulation was identified as optimal, striking a favorable balance between tensile strength, flexibility, and dimensional consistency, thereby validating its suitability as a sustainable FDM filament derived from post-consumer ABS waste.

Keywords : 3D Printing, Composite Filament, Fused Deposition Modeling (FDM), Morphology, Pineapple Leaf Fiber, Printability, Recycled ABS, Tensile Test.

1. INTRODUCTION

Plastics are widely used across numerous industries, but this extensive use generates substantial waste [1]. The recycling process is a beneficial way to handle plastic waste. As technology improves, the processing of plastic waste is becoming increasingly common as a source of new materials. One of the most promising outcomes of this development is composite materials, which are already applied in many applications [2], [3]. The matrix and fibers are the two parts that make up composites. These parts impart composites benefits like being light, strong, and resistant to corrosion.

In composite processing, there are several common methods used, such as compression molding and additive manufacturing (3D printing) [4]. Compression molding, which uses a hot press, is a widely used method because it can produce high-quality composites in various volumes. However, in practice, this method has a weakness: its inability to form composites in more complex configurations [5]. Compared to hot pressing, 3D printing methods have advantages in producing more complex and economical composite products, thereby improving the efficiency of the production process [6].

The 3D printing process uses filament as the main material. Thermoplastic materials are used to create 3D printer prototypes [6], [7]. Acrylonitrile Butadiene Styrene, or ABS, is one of the two common types of polymer thermoplastics used as filaments. To enhance its mechanical properties and sustainability, natural fibers are often added as reinforcement. Pineapple leaf fiber (PALF), with a high cellulose content (70–80%), offers excellent stiffness and strength, making it a promising additive. PALF-reinforced ABS filaments are suitable for use in various industries, including construction, automotive, and aerospace [8], [9].

Muck et al. (2021) study colour fastness to various agents and dynamic mechanical characteristics of

biocomposite filaments and 3d printed samples. The researcher used a matrix made of PLA with 5% wood and flax fibers added to it in the study [10]. The results showed that adding wood and flax fibers to PLA made it much rougher on the surface than pure PLA. The resulting filaments also changed size, going from 1.54 to 1.9 mm, which which in turn reduced filament uniformity. Previous research used ABS and PLA as the matrix materials, while flax fibers and rice husk served as the fillers. They use an extrusion temperature between 165 and 200°C for plastic pellets. With fiber mesh sizes of 75, 100, and 125 mesh, they found that particles larger than 100 mesh would cause clogging in the nozzle used. Therefore, the researchers used a larger nozzle size for fibers with particle sizes below 100 mesh. However, this will cause the filament results to decrease when extruded [11].

Compared with these studies, the present work focuses specifically on recycled ABS waste reinforced with PALF, with controlled variations in mesh size (200 and 300 mesh) and volume fraction (3 and 5 vol%). The recycled filament was extruded at 180°C . This study not only extends previous research by examining finer PALF particle sizes but also combine the practical issue of producing stable filaments from plastic waste, thereby supporting both material performance and sustainability objectives.

2. METHODS

This study used recycled ABS pellets (Polylac PA-757) as the matrix and pineapple leaf fibers (PALF) as reinforcement. The fibers were first cleaned using a wire brush to remove impurities and then treated with a 5% NaOH solution for 1 hour to eliminate non-cellulosic components. After rinsing with clean water, the fibers were oven-dried at 100°C for 2 hours and subsequently ground using a blender to produce fine powder. The resulting powder was sieved using 200 and 300 mesh screens to obtain the desired particle sizes. Both the ABS pellets and treated PALF were weighed using a digital scale to match the required fiber volume fractions of 3% and 5%. The schematic diagram mof filament preparation is shown in Figure 1.

The composite mixture of ABS pellets and pineapple leaf fiber (PALF) was homogenized and then processed using a WellZoom single-screw extruder at a temperature of 180°C. The filament exiting the 0.8 mm diameter nozzle is directed into a container of water for cooling to maintain dimensional stability and then wound onto a spool. During the extrusion process, parameters such as temperature, extrusion speed, and cooling rate are monitored to ensure filament consistency.

Filament dimension measurements were taken using a digital micrometer at several points along the filament to evaluate diameter uniformity, which is crucial for 3D printing performance. Measurement data were statistically analyzed by calculating the mean and coefficient of variation (CV) to assess dimensional stability. Additionally, the surface morphology of the filaments was observed using the same microscope to identify structural irregularities, fiber distribution, and the potential presence of voids, thus offering perspectives on the homogeneity and quality of the composite structure.

The extruded filaments from each variation were then cut into 10 cm lengths and was tensile tested according to the ASTM D3822 standard. Tensile testing was conducted using a Universal Testing Machine to obtain the maximum tensile strength (UTS), elongation at break, and Young's modulus values, thus enabling an evaluation of how the amount of pineapple leaf fiber and mesh size influence the mechanical performance of ABS waste-based composite filaments.

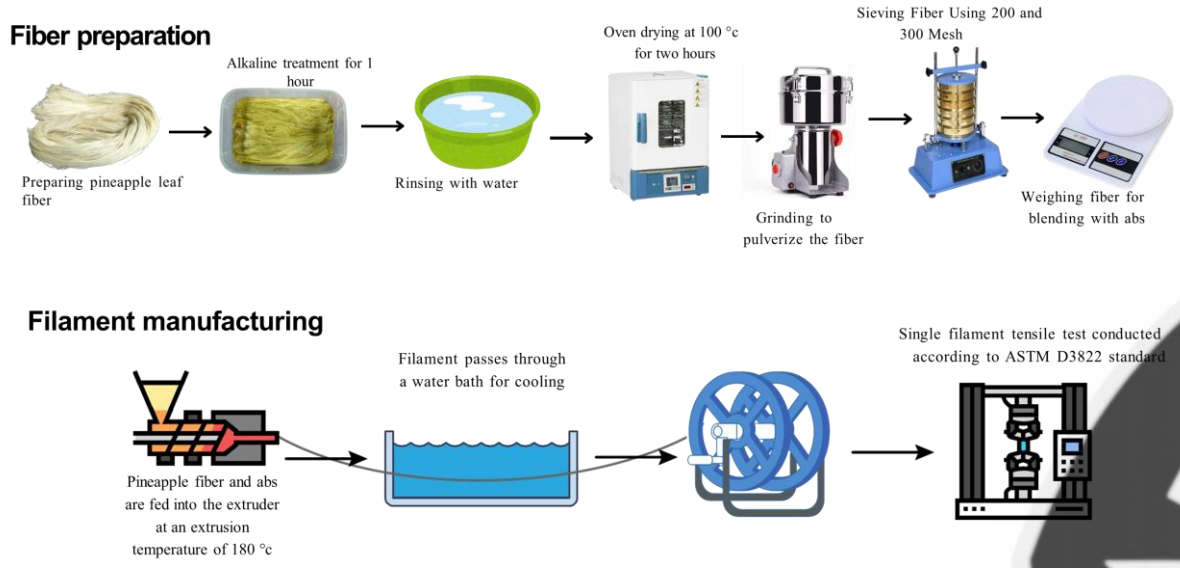

Figure 1. The sequential process of fiber preparation and filament manufacturing

Table 1. Summary of Experimental Variables Used

	Variable	Description / Levels
Matrix Material	ABS	Recycled ABS (Polylac PA-757) pellets
Reinforcement	Pineapple Leaf Fiber (PALF)	Cleaned, alkaline treated, ground, and sieved
Fiber Mesh Size	Mesh size	200 mesh and 300 mesh
Fiber Volume Fraction	vol%	3% and 5%
Extrusion Temperature	°C	180°C
Extruder Type	—	Single-screw WellZoom extruder
Nozzle Diameter	mm	0.8 mm
Cooling Method	—	Water bath during filament take-up
Measured Printability Parameters	Diameter uniformity	Mean diameter, coefficient of variation (CV)
	Surface morphology	Optical microscopy (roughness, fiber distribution, voids)
Mechanical Testing Parameters	Tensile properties	UTS, elongation at break, Young's modulus (ASTM D3822)
Sample Preparation	Filament length	10 cm samples for tensile testing

3. RESULTS AND DISCUSSION

3.1 Filament Morphology Analysis

Dimensional measurements were conducted using a digital micrometer with a resolution of 0.01 mm. For each filament sample, measurements were taken every 5 cm along a 100 cm segment, resulting in 20 data points per variation. As listed in table 2, the recorded average diameters for each formulation were as follows: 1.66 mm for 3% fiber content with 200 µm mesh, 1.73 mm for 5% with 200 µm mesh, 1.72 mm for 3% with 300 µm mesh, and 1.73 mm for 5% with 300 µm mesh. In research conducted by Cardona et al. [12], the tolerance for filaments for 3D printing was explained to be ±0.02 mm. Therefore, only the filament with 5% pineapple fiber content (for both 200 and 300 mesh) met the ISO 5425:2023 required the diameter 1.75 with the tolerance standard of ±0.02 mm and was deemed suitable for FDM-based 3D printing. The filament with 5% PALF had more stable diameters because the greater fiber content let the ABS–fiber combination melt more easily and flow more smoothly during extrusion. The higher fiber content at 5% made the composite flow more even and continuous, which reduced die swell variance and helped the extrudate keep its shape as it cooled in water. This makes the filament less likely to become bigger or thinner. Only the 5% PALF formulations met the ISO 5425:2023-dimensional criterion for a 1.75 mm filament (±0.02 mm). Thus, the data obtained showed that filaments with a volume fraction variation of 3% and 200 and 300 µm mesh did not meet the standard for the 3D printing process because the filament dimensional size exceeded the tolerance limit of ±0.02 mm. Filaments with a volume fraction of 5% and mesh sizes of 200 and 300 µm met the standard because their diameters were within the specified tolerance limits. This reasoning is supported by research conducted by Lendvai et al., which explains that deviations of more than ±0.02 mm cause unstable printing and deformation in the final printed product [13], [14].

Table 2. Coefficient of Variation (CV) of Filament Diameter

Fiber Volume Fraction	Mesh Size	Average Diameter (mm)	CV (%)
3%	200	1.66	11
5%	200	1.73	8
3%	300	1.72	5
5%	300	1.73	2

As shown in Table 2, the filament with 3% fiber content and 200 µm mesh exhibited the highest CV value of 11%, indicating significant dimensional inconsistency and poor homogeneity. This variation does not meet the threshold for acceptable printability (CV <10%). Meanwhile, the 5%/200 µm, 3%/300 µm, and 5%/300 µm variations achieved CV values of 8%, 5%, and 2%, respectively demonstrating better extrusion stability and fiber dispersion. The 5%/300 µm variant, with the lowest CV of 2%, meets the criteria for high dimensional precision and is the most suitable for FDM 3D printing applications.

Based on digital microscope analysis at 100× magnification (Figure 2), the surface morphology of the filaments shows significant variation across different combinations of pineapple fiber content and mesh size. Filaments with 3% fiber content and a 200 µm mesh size, exhibit a rough surface, high ovality, and dominant porosity due to uneven fiber distribution and particle clumping, potentially leading to nozzle clogging during extrusion. The 5% variation with a 200 µm mesh shows similar symptoms to the addition of air bubbles, indicating high moisture content, which, according to Hamrol et al.[15], can affect viscosity and dimensional stability, as

well as reduce print quality. Increasing the mesh size to 300 µm yielded better results, as seen in the 3%–300 µm variation, with the cross-sectional shape being closer to a circle, fiber distribution more even, and a reduction in the number of pores. Meanwhile, the 5%–300 µm variation showed the best morphology: a perfect circular cross-section, smooth surface, minimal porosity, and no indication of clogging, making it the most optimal formulation for FDM-based 3D printing. These results confirm that printability performance is highly influenced by dimensional uniformity, surface condition, particle size, moisture content, and extrusion process parameters, as previous research [16].

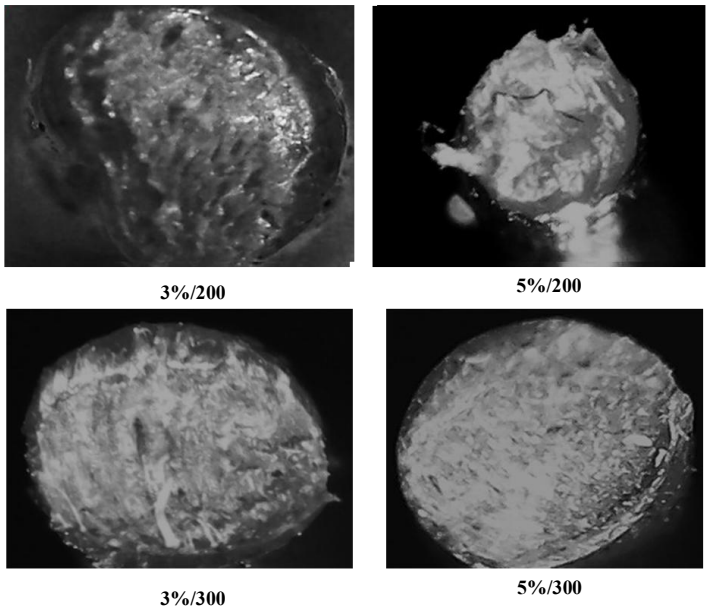

Figure 2. Surface morphology of filament with 3% /200, 5% /200, 3% /300, 5% /300 mesh size (100x maginification)

3.2 Tensile Properties of Filaments

Figure 4 and Table 3 show the results of tensile testing on the filament, the analyzed parameters such as Ultimate Tensile Strength (UTS), Yield Strength (YS), Young's Modulus, and Strain, each of which plays an important role in determining the performance of the composite material. The test results show that at a 5% variation and 300 mesh, this variation has the best mechanical performance compared to the other variations. This is indicated by the highest Yield Strength (YS) value of 8.873 MPa. This characteristic is highly advantageous for 3D printing applications that require high load resistance while maintaining dimensional stability, such as in 3D-printed structural components that need precise dimensions [17]. There was an increase in the variation of UTS (MPa), yield strength (MPa), Young's modulus (GPa), and strain (mm/mm) for the 5%/200, 3%/200, 5%/300, and 3%/300 mesh variations. The higher UTS and yield strength values for the 300-mesh variation are due to increasing the contact area between the fibers and the matrix, making load transfer from the matrix to the fibers more effective. The effect of increasing UTS and yield strength values will impact the filaments, making them stiffer and stronger even though the strain value obtained is relatively low. This is in line with research conducted by Wang et al., which explains that a significant increase in fiber fraction will add tensile strength and yield limit if the fibers are evenly dispersed [18], [19]. However, variation 5% /300mesh results the strain value was smaller, at 0.197. This can be explained by the fact that stiffness increases with a larger volume fraction of fibers, but although increasing the variation in fiber fraction further increases stiffness, the strain effectiveness of the filaments decreases. This can happen because of uneven fiber distribution, which creates weak zones in the material's binding structure [20]. Based on the evaluation of the tensile testing results on the filaments, the 5% addition of pineapple fiber with a mesh size of 300 is the most optimal variation, yielding the highest UTS value of 8.873 MPa and a strain value of 0.197. The balanced strain and UTS values make this variation a highly optimal combination. Naseer et al. explain that the optimal combination of strain and strength is crucial to avoid delamination during the extrusion process in the printing machine and to produce highly precise and durable prints[21].

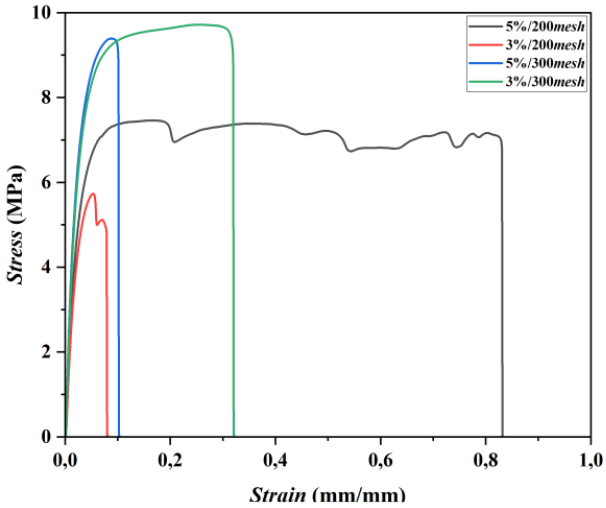

Figure 4. Graph of tensile properties of ABS-PALF Composite Filaments with different fiber volume fractions and mesh sizes.

Table 3. Tensile Properties of ABS-PALF Composite Filaments

Variation	Ultimate Tensile Strength (MPa)	Yield Strength (MPa)	Young's Modulus (GPa)	Strain (mm/mm)
5% / 200mesh	6.964 ± 0.63	6.584 ± 0.69	0.070 ± 0.04	0.650 ± 0.17
3% / 200mesh	5.063 ± 0.61	4.933 ± 0.65	0.077 ± 0.05	0.319 ± 0.15
5% / 300mesh	8.873 ± 0.52	8.873 ± 0.52	0.098 ± 0.04	0.197 ± 0.07
3% / 300mesh	7.795 ± 1.66	7.582 ± 1.76	0.139 ± 0.10	0.169 ± 0.14

4. CONCLUSION

Based on the research findings, it can be concluded that the volume fraction of pineapple leaf fibers and the fiber mesh size significantly influence the physical properties, surface morphology, and mechanical strength of composite filaments based on ABS waste. Increasing the fiber volume fraction from 3% to 5% was proven to improve dimensional stability, particle distribution homogeneity, and filament mechanical strength, particularly at the 5% variation with a 300 µm mesh size, which showed the most optimal performance. Conversely, a lower fiber volume fraction leads to fiber distribution irregularities, increases surface defects, and reduces tensile strength. On the other hand, the fiber mesh size also plays a key role in controlling morphological quality. Using smaller mesh-sized fibers (300 µm) results in a smoother filament surface, minimal porosity, and a more uniform cross-sectional shape, which directly impacts increased tensile strength. Thus, a combination of 5% volume fraction and 300 µm mesh size is recommended as the best formulation for producing viable and optimally usable ABS–PALF composite filaments in FDM-based 3D printing applications. Future investigations may examine fiber volume fractions ranging from 1% to 10%, various mesh sizes, and the implementation of hybrid fiber systems to expand the material design space. Variations in extrusion temperatures, screw speeds, and cooling methods can reveal correlations between processing and structure.

5. REFERENCES

[1] N. Evode, S. A. Qamar, M. Bilal, D. Barceló, and H. M. N. Iqbal, "Plastic waste and its management strategies for environmental sustainability," *Case Studies in Chemical and Environmental Engineering*, vol. 4, p. 100142, Dec. 2021, doi: 10.1016/j.cscee.2021.100142.

[2] E. Naderi Kalali, S. Lotfian, M. Entezar Shabestari, S. Khayatzadeh, C. Zhao, and H. Yazdani Nezhad, "A critical review of the current progress of plastic waste recycling technology in structural materials," *Curr Opin Green Sustain Chem*, vol. 40, p. 100763, Apr. 2023, doi: 10.1016/j.cogsc.2023.100763.

[3] H. Jung *et al.*, "Review of polymer technologies for improving the recycling and upcycling efficiency of plastic waste," *Chemosphere*, vol. 320, p. 138089, Apr. 2023, doi: 10.1016/j.chemosphere.2023.138089.

[4] S. Park, W. Shou, L. Makatura, W. Matusik, and K. Fu, "3D printing of polymer composites: Materials, processes, and applications," *Matter*, vol. 5, no. 1, pp. 43–76, Jan. 2022, doi: 10.1016/j.matt.2021.10.018.

[5] R. Phiri, S. Mavinkere Rangappa, S. Siengchin, O. P. Oladijo, and T. Ozbakkaloglu, "Advances in lightweight composite structures and manufacturing technologies: A comprehensive review," *Heliyon*, vol. 10, no. 21, p. e39661, Nov. 2024, doi: 10.1016/j.heliyon.2024.e39661.

[6] A. Jandyal, I. Chaturvedi, I. Wazir, A. Raina, and M. I. Ul Haq, "3D printing – A review of processes, materials and applications in industry 4.0," *Sustainable Operations and Computers*, vol. 3, pp. 33–42, 2022, doi: 10.1016/j.susoc.2021.09.004.

[7] R. B. Kristiawan, F. Imaduddin, D. Ariawan, Ubaidillah, and Z. Arifin, "A review on the fused deposition modeling (FDM) 3D printing: Filament processing, materials, and printing parameters," *Open Engineering*, vol. 11, no. 1, pp. 639–649, Apr. 2021, doi: 10.1515/eng-2021-0063.

[8] M. Harris, J. Potgieter, S. Ray, R. Archer, and K. M. Arif, "Acrylonitrile Butadiene Styrene and Polypropylene Blend with Enhanced Thermal and Mechanical Properties for Fused Filament Fabrication," *Materials*, vol. 12, no. 24, p. 4167, Dec. 2019, doi: 10.3390/ma12244167.

[9] S. R. Djafari Petroudy, "Physical and mechanical properties of natural fibers," in *Advanced High Strength Natural Fibre Composites in Construction*, Elsevier, 2017, pp. 59–83. doi: 10.1016/B978-0-08-100411-1.00003-0.

[10] D. Muck, H. G. Tomc, U. S. Elesini, M. Ropret, and M. Leskovšek, "Colour Fastness to Various Agents and Dynamic Mechanical Characteristics of Biocomposite Filaments and 3D Printed Samples," *Polymers (Basel)*, vol. 13, no. 21, p. 3738, Oct. 2021, doi: 10.3390/polym13213738.

[11] N. R. Rajendran Royan, J. S. Leong, W. N. Chan, J. R. Tan, and Z. S. B. Shamsuddin, "Current State and Challenges of Natural Fibre-Reinforced Polymer Composites as Feeder in FDM-Based 3D Printing," *Polymers (Basel)*, vol. 13, no. 14, p. 2289, Jul. 2021, doi: 10.3390/polym13142289.

[12] C. Cardona, A. H. Curdes, and A. J. Isaacs, "Effects of Filament Diameter Tolerances in Fused Filament Fabrication," *IU Journal of Undergraduate Research*, vol. 2, no. 1, pp. 44–47, May 2016, doi: 10.14434/iujur.v2i1.20917.

[13] L. Lendvai, I. Fekete, S. K. Jakab, G. Szarka, K. Verebélyi, and B. Iván, "Influence of environmental humidity during filament storage on the structural and mechanical properties of material extrusion 3D-printed poly(lactic acid) parts," *Results in Engineering*, vol. 24, p. 103013, Dec. 2024, doi: 10.1016/j.rineng.2024.103013.

[14] L. Lendvai, I. Fekete, D. Rigotti, and A. Pegoretti, "Experimental study on the effect of filament-extrusion rate on the structural, mechanical and thermal properties of material extrusion 3D-printed polylactic acid (PLA) products," *Progress in Additive Manufacturing*, vol. 10, no. 1, pp. 619–629, Jan. 2025, doi: 10.1007/s40964-024-00646-5.

[15] A. Hamrol, B. Góralski, and R. Wichniarek, "The Influence of Moisture Absorption and Desorption by the ABS Filament on the Properties of Additively Manufactured Parts Using the Fused Deposition Modeling Method," *Materials*, vol. 17, no. 9, p. 1988, Apr. 2024, doi: 10.3390/ma17091988.

[16] P. Pibulchinda, E. Barocio, A. J. Favaloro, and R. B. Pipes, "Influence of printing conditions on the extrudate shape and fiber orientation in extrusion deposition additive manufacturing," *Compos B Eng*, vol. 261, p. 110793, Jul. 2023, doi: 10.1016/j.compositesb.2023.110793.

[17] T. Appalsamy, S. L. Hamilton, and M. J. Kgaphola, "Tensile Test Analysis of 3D Printed Specimens with Varying Print Orientation and Infill Density," *Journal of Composites Science*, vol. 8, no. 4, p. 121, Mar. 2024, doi: 10.3390/jcs8040121.

[18] Y. Ou and D. Zhu, "Tensile behavior of glass fiber reinforced composite at different strain rates and temperatures," *Constr Build Mater*, vol. 96, pp. 648–656, Oct. 2015, doi: 10.1016/j.conbuildmat.2015.08.044.

[19] W. Alhaddad, M. He, Y. Halabi, and K. Y. M. Almajhali, "Influence of Fiber Volume Fraction on the Predictability of UD FRP Ply Behavior: A Validated Micromechanical Virtual Testing Approach," *Materials*, vol. 17, no. 19, p. 4736, Sep. 2024, doi: 10.3390/ma17194736.

[20] X. Wang *et al.*, "Low velocity impact properties of 3D woven basalt/aramid hybrid composites," *Compos Sci Technol*, vol. 68, no. 2, pp. 444–450, Feb. 2008, doi: 10.1016/j.compscitech.2007.06.016.

[21] M. N. Ahmad, M. R. Ishak, M. Mohammad Taha, F. Mustapha, and Z. Leman, "A Review of Natural Fiber-Based Filaments for 3D Printing: Filament Fabrication and Characterization," *Materials*, vol. 16, no. 11, p. 4052, May 2023, doi: 10.3390/ma16114052.

LOGIC
Journal of Engineering Design and Technology
Vol. 25 No.3 November ; p. 175-185

p-ISSN : 1412-114X
e-ISSN : 2580-5649
http://ojs2.pnb.ac.id/index.php/LOGIC

REDESIGN OF PATIENT WHEELCHAIR TYPE SM-8018 BASED ON ERGO-TOTAL FUNCTION DEPLOYMENT (ETFD) INTEGRATION

Heri Setiawan [1)], M. Yusuf[2)], Micheline Rinamuti [3)], Dominikus Budiarto [4)], Yohanes Dicka Pratama [5)], Achmad Alfian [6)]

[1,4,5,6)] Industrial Engineering Study Program, Musi Charitas Catholic University, Jl. Bangau No. 60 Palembang, South Sumatera, Indonesia
[2)] Mechanical Engineering, Politeknik Negeri Bali, Badung, Indonesia
[3)] Management Study Program, Musi Charitas Catholic University, Jl. Bangau No. 60 Palembang, South Sumatera, Indonesia

Correponding email [1)] : heri_setiawan@ukmc.ac.id

Abstract. Manual wheelchairs remain widely used in Indonesian health-care facilities, yet their design often does not fully accommodate local anthropometric characteristics and work patterns. The SM-8018 patient wheelchair used at PT SPU is operated by caregivers, exposing both patients and caregivers to potential ergonomic risks. This study aims to evaluate and redesign the SM-8018 wheelchair using an integrated Ergo-Total Function Deployment (ETFD) and House of Ergonomics (HoE) approach within a Total Ergonomics framework. A pre–post experimental design was applied involving 32 adult users and caregivers with at least six months of experience using or pushing the SM-8018. Data collection included anthropometric measurements, musculoskeletal complaints using the Nordic Body Map (NBM), subjective fatigue using the Japan Association of Industrial Health (JAIH) questionnaire, boredom scores, satisfaction using the Minnesota Satisfaction Questionnaire (MSQ) and voice of customers (VoC). VoC and ergonomic findings were mapped into a HoE matrix to derive priority design specifications through ETFD. Results showed notable mismatches between user anthropometry and key wheelchair dimensions, particularly seat depth and width, backrest and headrest height and angle, and push-handle height, which were associated with high levels of discomfort in the lower back, buttocks, shoulders and upper arms and with considerable fatigue. The ETFD–HoE analysis identified four primary redesign priorities: adjustment of push-handle height, optimisation of backrest and headrest geometry, refinement of seat dimensions and improvement of front-wheel stability. Pre–post comparisons indicated that musculoskeletal complaints and fatigue remained relatively high and in some cases increased, whereas boredom and satisfaction tended to change in a more favourable direction. These findings suggest that the first iteration of the SM-8018 redesign, although guided by Total Ergonomics principles, requires further refinement and system-level support. Nonetheless, the study demonstrates the feasibility of integrating ETFD, HoE and Total Ergonomics to systematically guide the improvement of low-cost hospital wheelchairs in the Indonesian context.

Keywords : ETFD Integration, Redesign, The Patient Wheelchair Type SM-8018, Total Ergonomic

1. INTRODUCTION

Wheelchairs are assistive devices that enable individuals with permanent or temporary mobility limitations to move, carry out daily activities and participate in social life more independently [1][2]. In health-care facilities, manual wheelchairs remain the most widely used because of their simple construction, low maintenance cost and

ease of repair, even though powered wheelchairs have been increasingly introduced in high-income settings [3][4]. The SM-8018 manual patient wheelchair is one of the commonly used models in Indonesian hospitals and clinics. This wheelchair is designed to be pushed by a caregiver rather than self-propelled by the patient, so that both the seated patient and the thruster are directly affected by the ergonomics of the product.

Field observations and preliminary evaluations at PT SPU indicate that several critical components of the SM-8018 wheelchair do not yet adequately accommodate the anthropometric characteristics and activity patterns of its users. The seat width, depth and height do not fully correspond to the body dimensions of typical Indonesian adult patients; the backrest and headrest are fixed and do not provide sufficient support for the upper back and cervical region; the push-handle height is not aligned with the elbow height of most caregivers; and the configuration of the front wheels may reduce stability when the wheelchair passes ramps or uneven floors. These design limitations may increase static muscular load and awkward postures during sitting and pushing, thereby contributing to musculoskeletal complaints, discomfort and fatigue for both patients and caregivers [5][6][7][8]. Inadequate comfort and safety in turn can negatively influence patients' perceived quality of life during treatment and rehabilitation [1][2].

From an ergonomic perspective, prolonged sitting in a constrained posture combined with repeated pushing tasks can trigger musculoskeletal disorders (MSDs), especially in the neck, back, shoulders, arms and buttocks. Such disorders are frequently assessed using instruments such as the Nordic Body Map (NBM) to identify the location and intensity of complaints [9]. In addition to physical complaints, indicators of mental and physiological load – including subjective fatigue, feelings of monotony or boredom, and job satisfaction – also play an important role in evaluating the acceptability of a work system and the design of the tools used [10][11][12][13]. The Japan Association of Industrial Health (JAIH) fatigue questionnaire, boredom scales and the Minnesota Satisfaction Questionnaire (MSQ) are widely used to capture these aspects in a systematic way.

A number of previous studies have discussed the design and improvement of wheelchairs from mechanical, structural or basic anthropometric perspectives, focusing for example on strength, stability, manoeuvrability or simple dimensional fit between users and products [3][4][6]. Other research has applied Quality Function Deployment (QFD) or limited ergonomic checklists to translate the voice of customers into design specifications. However, these studies generally analyse either physical complaints or user preferences separately, and rarely integrate musculoskeletal complaints, fatigue, boredom and satisfaction into a single, comprehensive evaluation framework. Furthermore, there is still limited research that applies Total Ergonomics – integrating Appropriate Technology (AT) and the Systemic, Holistic, Interdisciplinary and Participatory (SHIP) approach – to low-cost manual hospital wheelchairs in the Indonesian context [5][7][8].

Consequently, several important gaps remain. First, the specific ergonomic shortcomings of the existing SM-8018 design, particularly in relation to Indonesian patients' and caregivers' anthropometry and patterns of use, have not been described in detail. Second, previous ergonomic and QFD-based studies on wheelchair design have not explicitly integrated multidimensional outcome measures (MSDs, fatigue, boredom and satisfaction) with an Ergo-Total Function Deployment (ETFD) or House of Ergonomics (HoE) approach. Third, the potential of Total Ergonomics (AT and SHIP) to systematically prioritise design improvements for hospital wheelchairs has not yet been fully explored.

To address these gaps, this study aims to redesign the SM-8018 manual patient wheelchair used at PT SPU based on an integrated Ergo-Total Function Deployment approach. Specifically, the objectives of this research are: (1) to evaluate the mismatch between the current SM-8018 wheelchair dimensions and the anthropometric characteristics, musculoskeletal complaints, fatigue, boredom and satisfaction of users and caregivers; (2) to construct a House of Ergonomics that translates the voice of customers and ergonomic risk findings into technical design requirements; and (3) to determine and prioritise key design modifications for the SM-8018 patient wheelchair within a Total Ergonomics (AT and SHIP) framework so as to enhance comfort, safety, health and efficiency for both patients and caregivers.

2. METHODS

2.1 Research design and setting

This study employed a pre–post experimental design to evaluate and redesign the SM-8018 manual patient wheelchair used at PT SPU, a medical equipment manufacturer and distributor in Indonesia. The pre–post design was chosen to enable direct comparison between the existing wheelchair configuration and the redesigned specifications in terms of anthropometric fit, musculoskeletal complaints, fatigue, boredom and user satisfaction. The ergonomic evaluation and measurement sessions were conducted in the wheelchair assembly and testing area under typical working conditions.

2.2 Participants

A total of 32 participants took part in this study. They consisted of adult users and caregivers who routinely operated or pushed the SM-8018 wheelchair at PT SPU and affiliated health-care facilities. Inclusion criteria were: (1) age ≥ 18 years, (2) experience in sitting in or pushing the SM-8018 wheelchair for at least six months, and (3) absence of acute musculoskeletal injury during the data collection period. Participants who reported severe pain requiring medical treatment or who were unable to complete the questionnaires were excluded. All participants were informed about the study procedures and provided written consent prior to participation.

2.3 Variables and instruments

To address the first objective—evaluating the mismatch between the current SM-8018 design and user characteristics—several groups of variables were measured:

1. Anthropometric dimensions
   Key body dimensions relevant to wheelchair design were recorded, including: popliteal height, buttock–popliteal length, hip breadth, elbow height in standing and sitting, shoulder height, and body mass and stature. Measurements were taken using a standard anthropometer, measuring tape and digital scale, following conventional anthropometric procedures. These data were later compared with the existing dimensions of the SM-8018 seat, backrest, armrest, headrest and push handle.
2. Musculoskeletal complaints (MSDs)
   Musculoskeletal complaints were assessed using the Nordic Body Map (NBM) questionnaire. Participants reported the presence and intensity of discomfort or pain in different body regions (e.g., neck, shoulders, back, buttocks, arms and legs) after using or pushing the wheelchair. Scores for each body part were coded and summed to generate an overall MSD index, and the percentage of participants reporting discomfort in each region was calculated.
3. Subjective fatigue
   Subjective fatigue was measured using the Japan Association of Industrial Health (JAIH) fatigue questionnaire, which consists of multiple items covering general, physical and mental fatigue symptoms. Responses were recorded on a Likert-type scale and converted into an overall fatigue index. Higher scores indicated higher perceived fatigue.
4. Boredom / monotony
   Feelings of monotony or boredom related to the activity of sitting in or pushing the wheelchair were captured using a boredom scale that assessed the extent to which participants experienced repetitive, unchallenging or monotonous tasks. The items were rated on a Likert scale, and an average boredom score was computed for each participant.
5. Satisfaction
   User satisfaction with the SM-8018 wheelchair was evaluated using the Minnesota Satisfaction Questionnaire (MSQ) adapted to the context of assistive device use. Items addressed comfort, ease of use, perceived safety and overall satisfaction. Responses were transformed into a satisfaction index, where higher scores represented higher satisfaction.
6. Voice of customers (VoC) and ergonomic requirements
   In addition to the standardized instruments above, semi-structured interviews and open-ended questions were used to collect the voice of customers (VoC) from both patients and caregivers. The VoC data captured qualitative perceptions regarding comfort, safety, handling, stability on ramps or uneven surfaces, and suggestions for improvement. These qualitative inputs were then translated into ergonomic requirements and technical characteristics within the Ergo-Total Function Deployment (ETFD) framework.

2.4 Procedure

Data collection was carried out in two main stages corresponding to the pre–post design.

1. Pre-intervention (baseline) stage
   a) Participants were first familiarised with the purpose of the study and the measurement instruments.
   b) Anthropometric measurements were taken once for each participant.
   c) Participants then used or pushed the existing SM-8018 wheelchair while performing typical patient transport activities (e.g., moving along corridors, turning, passing ramps or uneven floor transitions) for a specified duration.
   d) Immediately after the activity, participants completed the NBM, JAIH fatigue, boredom and MSQ satisfaction questionnaires, and provided qualitative feedback (VoC) on perceived problems and desired improvements.
2. Design development stage using ETFD and House of Ergonomics (HoE)

a) The baseline anthropometric data, MSD, fatigue, boredom and satisfaction indices, along with VoC information, were consolidated to identify ergonomic problems and potential mismatches between the existing SM-8018 design and user needs.
b) These findings were mapped into a House of Ergonomics (HoE), in which the "customer ergonomic requirements" (comfort, safety, health, efficiency, stability and ease of handling) were linked to "ergonomic design characteristics" such as seat width and depth, backrest and headrest height and angle, push-handle height, wheelbase and front-wheel configuration.
c) The HoE matrix was used to calculate relationship weights and priorities, forming the core of the Ergo-Total Function Deployment (ETFD) process and generating a set of prioritized design specifications.

3. Post-intervention (prototype evaluation) stage
a) Based on the prioritized specifications from ETFD, redesign recommendations for the SM-8018 wheelchair were formulated, focusing on adjustments to seat dimensions, backrest and headrest configuration, push-handle height and wheel stability.
b) A prototype or detailed redesign concept reflecting these specifications was then evaluated by the same group of participants under similar task conditions.
c) After using or pushing the redesigned wheelchair, participants once again completed the NBM, JAIH fatigue, boredom and MSQ satisfaction questionnaires and provided feedback on the redesigned features.

2.5 Data analysis

Descriptive statistics (mean, standard deviation, minimum, maximum and percentiles) were calculated for all anthropometric variables and compared with the corresponding dimensions of the existing SM-8018 wheelchair to identify mismatches and inform the redesign. For the subjective outcome measures (MSDs, fatigue, boredom and satisfaction), pre- and post-intervention scores were computed for each participant.

Prior to inferential analysis, the normality of the difference scores was examined using the Shapiro–Wilk test. When the data satisfied the normality assumption, paired sample t-tests were applied to compare pre- and post-intervention means for each outcome variable at a significance level of $\alpha = 0.05$. For variables that did not meet normality assumptions, the non-parametric Wilcoxon signed-rank test was considered. In addition, percentage changes in MSDs, fatigue, boredom and satisfaction indices were calculated to facilitate interpretation of the practical impact of the redesign.

2.6 Integration of ETFD and Total Ergonomics

To address the second and third objectives—constructing the HoE and prioritising key design modifications within a Total Ergonomics framework—the ETFD results were analysed using the principles of Appropriate Technology (AT) and the Systemic, Holistic, Interdisciplinary and Participatory (SHIP) approach. Customer ergonomic requirements and technical characteristics were interpreted in terms of the ECSHE dimensions (Effective, Comfortable, Safe, Healthy and Efficient).

The final redesign priorities were determined by combining: (1) the quantitative priority weights obtained from the ETFD/HoE matrix, (2) the magnitude and statistical significance of changes in MSDs, fatigue, boredom and satisfaction, and (3) qualitative feedback from participants. This integrated analysis produced a ranked list of critical design features—such as push-handle height, backrest and headrest geometry, and front-wheel stability—that should be modified in order to improve comfort, safety, health and efficiency for both patients and caregivers when using the SM-8018 patient wheelchair.

3. RESULTS AND DISCUSSION

3.1 Description of the existing SM-8018 patient wheelchair

The SM-8018 manual patient wheelchair used at PT SPU is designed to be pushed by a caregiver rather than self-propelled by the patient. Figure 1 shows the standard components of a manual wheelchair together with the main elements of the SM-8018 model, including the seat, backrest, armrests, footrests, headrest, push handles and wheel configuration. Figure 2 illustrates the SM-8018 wheelchair when in use during typical patient transport activities such as moving along corridors, turning and passing ramps or uneven floor transitions.

Figure 1. a) Standard manual wheelchairs and their parts [7][10], and b) dimensions of the patient wheelchair type SM-8018 production result of PT SPU

Figure 2. The Design of the SM-8018 Patient Wheelchair When in Use

Field observations during the baseline stage indicated several practical limitations of the existing design. The fixed backrest and headrest do not adequately support the upper back and cervical region for many users, and the seat dimensions do not fully match the anthropometric characteristics of typical Indonesian adults. For caregivers, the push-handle height appears lower or higher than their natural elbow height, which forces them to bend forward or elevate their shoulders while pushing. These qualitative observations are consistent with the initial complaints reported by participants and motivated the need for a more systematic ergonomic evaluation and redesign of the SM-8018 wheelchair.

3.2 House of Ergonomics and ETFD results

The voice of customers (VoC) collected from patients and caregivers was translated into ergonomic requirements and mapped into a House of Ergonomics (HoE) matrix (Figure 3). In this HoE, customer ergonomic requirements—such as comfort during sitting, perceived safety, stability on ramps, ease of handling, postural support and ease of maintenance—were positioned on the left side of the matrix, while technical/ design characteristics—such as seat width and depth, seat height, backrest and headrest height and angle, push-handle height, wheelbase and front-wheel configuration—were placed along the top.

Table 1. Summary of Participants' Responses to the ECSHE Variable Characteristics and Assessment of Wheelchair Components

Variable	Attribute	Wheelchair Parts	Wheelchair Evaluation
Effective (E)	Performance Functional	Stability (Static & Dynamic)	When in a fixed state, it performs well, but within a moving or adaptable framework, it remains less stable if the user's body weight is overweighed
		Transporting patient wheelchair (simple to transfer between locations, simple to use, simple to transport a mobility chair)	It functions well, however, the front tire continues to spin, pivot, and halt independently if it encounters a minor obstruction.
Comfortable (C)	Holder and Postural supports	Dimensions (Greatest dimensions, breadth, overall stature, height of the seat, width of the seat from the flooring, height of the armrests relative to the seat, length of the seat, elevation of the backrest, maximum weight capacity for wheelchairs,	The quality is acceptable, but the elevation of the back support is inadequate; it needs to reach the level of the head or headrest. The chair's rear support is not designed for proper posture, being both shorter and less inclined

		modifying the anthropometric measurements to fit the Indonesian population)	
		Holder (Seat type, seat cushion, seat material, seat cushion material)	The padding on the seat is inadequate, causing it to indent when you sit, resulting in discomfort for the backside
		Adjustable and Ergonomic Factor (Beckrest, footrest, armrest, rear wheels, push handle)	Not ideal, particularly in the lower backrest area (there is indeed a headrest), the push handle has not been modified, resulting in cramps, discomfort, and fatigue from pushing.
Safe (S)	Strength, Durability and Safety	Strong material (Hard frame material)	Already well
		Endurance (Chair framei, push handle)	It works well; it continues to shake even if the person using it is overweight, but the handle for pushing cannot be modified.
		Flammability (Not flammable, Corrosion resistant)	Already well
		Surface safety (Flat surface, tire cover, have reflective stickers)	Already well
		Brake effectiveness (Stopped on the descent, did not come off suddenly)	Unsuitable for descending, ascending, and uneven terrain conditions.
Healthy (H)	MSDs	Reduce musculoskeletal complaints	There are still musculoskeletal complaints
	Fatigue	Reduces fatigue	Tired of pushing especially the push handle
	Boredom	Reduces boredom	It can reduce boredom
	Satisfaction	Increase satisfaction	Not yet satisfied
Efficient (E)	Economic	Affordable product prices	Prices can be pressed again
	Maintenance	Easy to care for	Already well
	Raw Material	Raw material are strong and durable	The structure still appears delicate when the individual is overweight. Certain components are prone to damage (such as brake pads)

The relationships between customer requirements and technical characteristics were scored and weighted within the Ergo-Total Function Deployment (ETFD) framework. This analysis produced priority weights indicating which design attributes contributed most strongly to comfort, safety, health and efficiency (ECSHE). As summarised in Table 1, participants consistently highlighted issues of comfort (particularly in the back and buttocks), safety and stability when passing ramps, and physical effort required when pushing the wheelchair. These complaints were strongly associated, in the HoE matrix, with the geometry of the seat and backrest, the headrest configuration, the push-handle height and the stability of the front wheels.

The ETFD results, integrated with the Total Ergonomics perspective (Appropriate Technology and SHIP), are further detailed in Tables 2 and 3. Table 2 indicates how each proposed design change respects Appropriate Technology principles—being simple, affordable and maintainable in the PT SPU context—while Table 3 shows how the redesign aligns with the Systemic, Holistic, Interdisciplinary and Participatory (SHIP) approach. Overall, the ETFD–HoE analysis identified four main redesign priorities: (1) adjustment of push-handle height, (2) optimisation of backrest and headrest height and angle, (3) refinement of seat dimensions (width and depth) to match user anthropometry, and (4) improvement of front-wheel stability when the wheelchair passes ramps or uneven surfaces.

Table 2. Use of AT in Ergonomics Total Case Study the Patient Wheelchair Type SM-8018 Product Redesign

No.	Aspects of AT	Problem Solving Description
1.	Technically	Holder and postural supports the patient wheelchair type SM-8018 product redesign to find the root cause of ergonomics is not too difficult
2.	Economical	Redesign of holder and postural supports the patient wheelchair type SM-8018 product does not require high cost investment so that PT SPU can immediately follow up
3.	Ergonomics	Redesign of the potential for ergonomics of the patient wheelchair type SM-8018 product redesign with improved holder and postural supports to improve patient quality of life
4.	Socio-culturally	The holder and postural supports improvements have no implications for socio-cultural interactions between patients with of the patient wheelchair type SM-8018 product redesign pushers and the general social community
5.	Energy efficient	The redesign does not require energy that exceeds the threshold value and does not have an impact on excessive energy utilisation. the energy expended from pushing of the patient wheelchair type SM-8018 product redesign and patient also decreases
6.	Environmentally friendly	The patient wheelchair type SM-8018 product redesign has no impact on causing environmental pollution and supports sustainability

Table 3. Use of SHIP Approach in Ergonomics Total Case Study the Patient Wheelchair Type SM-8018 Product Redesign

No.	Aspects of AT	Problem Solving Description
1.	Systemic	An approach that considers the system as a whole, including human, technological, and environmental factors, to improve worker performance, safety, and health. system analysis, problem identification, system design, system implementation, and system evaluation have solved the problem of holder and postural supports the patient wheelchair type SM-8018 product redesign
2.	Holistic	Understand the system as a single entity consisting of many interrelated components. Solve problems without creating new ones
3.	Interdisplinary	Combining knowledge from various disciplines, such as psychology, physiology, engineering, and design to the patient wheelchair type SM-8018 product redesign
4.	Participatory	Involve workers and other stakeholders in the system design and implementation process of the patient wheelchair type SM-8018 product redesign

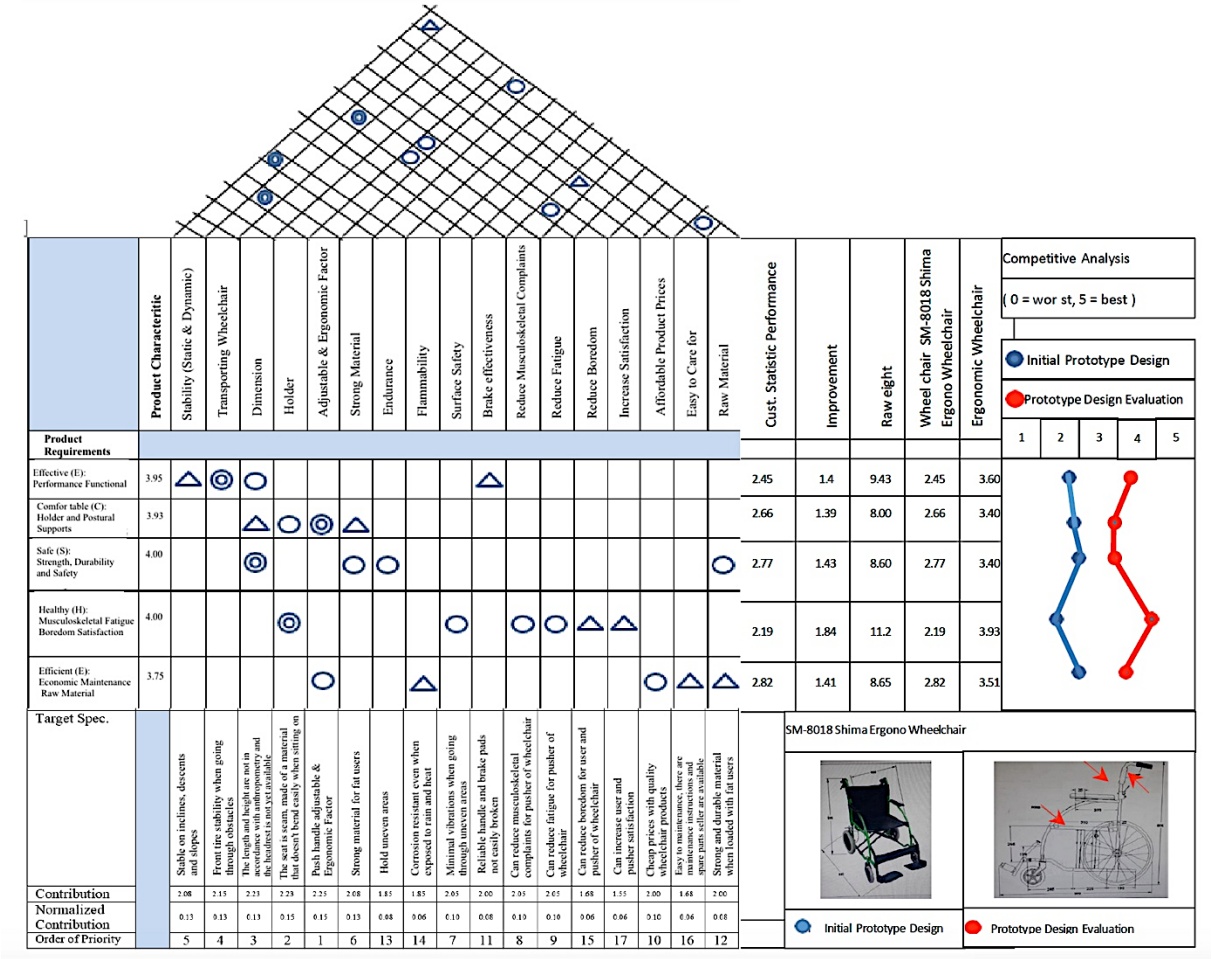

Figure 3. House of ergonomic of the patient wheelchair type SM-8018 protoype product

3.3 Anthropometric Fit and Musculoskeletal Complaints

Anthropometric data collected from the 32 participants revealed mismatches between the existing SM-8018 dimensions and the body dimensions of users. For many participants, the seat depth exceeded their buttock–popliteal length, which may increase pressure in the popliteal area and promote slouched sitting. Likewise, the seat width did not always provide sufficient lateral support, and the backrest height did not reach a recommended level relative to shoulder and cervical height. The push-handle height often fell below or above the elbow height in standing, forcing caregivers to adopt non-neutral postures when pushing.

These mismatches were reflected in the musculoskeletal complaints measured using the Nordic Body Map (NBM). A large proportion of participants reported discomfort or pain in the lower back and buttocks, as well as in the shoulder and upper arm regions after using or pushing the wheelchair. Complaints were particularly concentrated in body segments that directly interact with the wheelchair components (seat, backrest, headrest and push handles). From an ergonomic perspective, these findings indicate that the current design of the SM-8018 wheelchair does not yet provide adequate postural support and load distribution during prolonged sitting and pushing tasks.

The patterns of musculoskeletal complaints observed in this study are consistent with previous ergonomic investigations that link non-optimal seat and backrest geometry with increased low-back and buttock discomfort, and associate inappropriate handle height with shoulder and upper-back strain [7][9][10]. They support the need to adjust the SM-8018 dimensions based on Indonesian anthropometric data, as recommended in the Total Ergonomics approach [14][15][16][17].

3.4 Fatigue, Boredom and Satisfaction Outcomes

Subjective fatigue measured by the JAIH questionnaire, boredom scores and satisfaction indices (MSQ) provided a more comprehensive view of the impact of the SM-8018 design on users and caregivers. In the baseline (pre-

intervention) condition, participants reported noticeable levels of fatigue after performing typical wheelchair-related tasks, as well as feelings of monotony in repetitive pushing activities and only moderate levels of satisfaction with comfort, stability and ease of handling.

Following the ETFD-based redesign and evaluation of the prototype, the statistical analysis of pre–post data showed that musculoskeletal complaint indices and fatigue scores remained relatively high and, in some cases, increased significantly, whereas boredom and satisfaction scores changed in the opposite direction. In other words, although the redesign addressed several priority dimensions identified in the HoE, the short-term impact on physical load was not yet fully favourable, while some aspects of perceived monotony and satisfaction showed a tendency to improve or at least change in a more positive direction.

This pattern contrasts with the results of previous ergonomic interventions conducted by Setiawan and co-workers in other industries. For example, in a study on redesigning wet blanket workstations in a crumb rubber factory, the integration of ergonomic principles led to a substantial reduction in worker fatigue [18]. Similarly, an intervention applying a comprehensive ergonomic work system at a tofu factory resulted in a marked decrease in fatigue complaints [19][20][21][22][23], and an ergonomics-based improvement programme for freight workers at the 16 Ilir Market in Palembang produced a notable increase in satisfaction levels [24].

Compared with these earlier interventions, the present study suggests that the first iteration of the SM-8018 redesign—although guided by ETFD and Total Ergonomics—may still require further refinement, particularly in relation to load distribution during pushing and the dynamic stability of the wheelchair. The persistence or increase of musculoskeletal complaints and fatigue indicates that some critical constraints, such as overall weight, rolling resistance, or the interaction between seat/backrest geometry and pushing technique, have not yet been fully resolved.

3.5 Integrated Discussion in the Total Ergonomics Perspective

The combined results of anthropometric evaluation, NBM, fatigue, boredom and satisfaction measurements, and ETFD–HoE analysis highlight the complexity of designing an ergonomically sound manual patient wheelchair in a realistic industrial context. On the one hand, the HoE and ETFD framework successfully translated the voice of customers and ergonomic findings into a set of clear technical priorities, namely the adjustment of push-handle height, optimisation of backrest and headrest design, refinement of seat dimensions and improvement of front-wheel stability. These priorities are consistent with the ECSHE dimensions (Effective, Comfortable, Safe, Healthy and Efficient) and with the principles of Appropriate Technology and SHIP.

On the other hand, the pre–post comparison of subjective outcomes indicates that modifying a subset of design parameters alone is not always sufficient to reduce musculoskeletal load and fatigue in the short term. In the SM-8018 case, it is possible that the redesigned configuration alters the way caregivers push and control the wheelchair, leading to temporary changes in muscle activation patterns and perceived effort. Furthermore, some contextual factors—such as floor conditions, frequency and duration of wheelchair use, and work-organisation aspects including rest pauses and task rotation—may still be sub-optimal and continue to contribute to fatigue and discomfort.

From a Total Ergonomics standpoint, these findings emphasise that product redesign must be integrated with broader system-level changes. In addition to refining the SM-8018 geometry based on the present ETFD priorities, future interventions should consider: (1) optimising the rolling resistance and overall mass of the wheelchair, (2) providing training for caregivers on optimal pushing techniques and posture, (3) improving environmental conditions such as floor smoothness and ramp design, and (4) revisiting work-organisation policies to ensure adequate rest breaks and task variation.

Despite these limitations, the present study demonstrates the feasibility of applying the Ergo-Total Function Deployment and House of Ergonomics approach to a low-cost hospital wheelchair in Indonesia. The integration of quantitative anthropometric and subjective outcome measures with a participatory, SHIP-based design process offers a structured pathway for progressively improving the SM-8018 wheelchair. Subsequent design iterations, validated with larger samples and complemented by objective measures of posture and force, are expected to achieve reductions in musculoskeletal complaints and fatigue closer to those observed in previous Total Ergonomics interventions in other sectors [25][26][27][28].

4. CONCLUSION

This study applied an integrated Ergo-Total Function Deployment (ETFD) and House of Ergonomics (HoE) approach within a Total Ergonomics framework to evaluate and redesign the SM-8018 manual patient wheelchair used at PT SPU. By combining anthropometric measurements, musculoskeletal complaints (NBM), subjective fatigue (JAIH), boredom and satisfaction (MSQ) with the voice of customers (VoC), the research aimed to identify mismatches between the existing design and user needs, translate ergonomic requirements into technical specifications and prioritise key design modifications.

The results indicate that the current SM-8018 wheelchair does not yet adequately accommodate the anthropometric characteristics of Indonesian patients and caregivers. Seat depth and width, backrest and headrest height and angle, as well as push-handle height, showed notable mismatches with user body dimensions. These discrepancies were reflected in musculoskeletal complaints concentrated in the lower back, buttocks, shoulders and upper arms, and in considerable levels of subjective fatigue after typical wheelchair-related tasks. The HoE and ETFD analysis confirmed that comfort, safety, stability and ease of handling are strongly linked to the geometry of the seat, backrest and headrest, push-handle height and front-wheel configuration.

The pre–post comparison of subjective outcomes following the ETFD-based redesign revealed that musculoskeletal complaints and fatigue remained relatively high and in some cases increased, whereas boredom and satisfaction scores showed a tendency to change in a more favourable direction. These findings suggest that the first iteration of the SM-8018 redesign, although guided by ergonomic priorities and Total Ergonomics principles, is not yet sufficient to substantially reduce physical load in the short term. Product-level improvements need to be complemented by further optimisation of seat and backrest support, push-handle ergonomics, wheelchair mass and rolling resistance, as well as by system-level changes in work organisation, environmental conditions and caregiver training.

Despite these limitations, the study demonstrates the feasibility and usefulness of integrating ETFD, HoE and Total Ergonomics (AT and SHIP) for the systematic improvement of low-cost hospital wheelchairs in the Indonesian context. The approach produced a clear set of redesign priorities—namely adjustment of push-handle height, optimisation of backrest and headrest geometry, refinement of seat dimensions and enhancement of front-wheel stability—that can guide subsequent design iterations at PT SPU. Future research should involve larger and more diverse samples, incorporate objective measures of posture and force, and evaluate long-term effects of the redesigned wheelchair on musculoskeletal load, fatigue, boredom and satisfaction in real clinical settings.

5. ACKNOWLEDGEMENT

The author would like to thank the staff of PT SPU Palembang for providing data support and observations, the academic community of lecturers of Industrial Engineering Study Program & Management Study Program, LPPM Musi Charitas Catholic University, and the Logic Journal Editor and Reviewer Team for publishing this article.

6. REFERENCES

[1] H. Castellucci et al., “Applied anthropometry for common industrial settings design: Working and ideal manual handling heights,” Int. J. Ind. Ergon., vol. 78, p. 102963, 2020, doi: https://doi.org/10.1016/j.ergon.2020.102963.

[2] H. Setiawan, M. Rinamurti, C. D. Kusmindari, A. Alfian, Y.D. Pratama, and D. Budiarto, “Ergonomic Hazard Measurement, Evaluation and Controlling in the Pempek Palembang Home Industry Based on SNI 9011:2021”, International Journal of Innovative Science and Research Technology, vol.8, no.5, Jun. 2023, doi: 10.5281/zenodo.8037377.

[3] S. Pheasant and C. M. Haslegrave, Bodyspace: Anthropometry, Ergonomics and the Design of Work, Third Edition, 3rd ed. Boca Raton: CRC Press., 2016.

[4] H. Setiawan, et al., Sistem Lingkungan Industri. In M. S.: Mila Sari, (Ed.), Book Chapter (1st ed., pp. 103–121). Indonesia: Get Press, 2023.

[5] H. Setiawan, S. Susanto, M. Rinamurti, and Y. D. Pratama, “Implementation of Ergo-Tourism and Local Wisdom to Design Tourism Village Governance Based on Balinese Cultur in Darma Buana, Belitang II South Sumatera Province”, Toursci, vol. 2, no. 3, pp. 237–247, Feb. 2025, doi: https://doi.org/10.62885/toursci.v2i3.618

[6] Webster, K. L. W., and Haut, E. R. Human factors and ergonomics in the operating room. In Handbook of Perioperative and Procedural Patient Safety, Book Chapter (pp. 75-86), Marilands: Elsevier Press, 2023.

[7] H. Setiawan, S. Susanto, M. Rinamurti, and A. Alfian, “Design and Implementation of Green Human Resource Management (Green HRM) in SMEs Palembang City ”, Ekuisci, vol. 2, no. 3, pp. 188–198, Jan. 2025, doi: https://doi.org/10.62885/ekuisci.v2i3.597

[8] Rinamurti, M., and Setiawan, H., “Industrial Ergonomic Work Design to Improve The Employee Quality of Life and Productivity at PT Cita Rasa Palembang”, *AIP Conference Proceedings*, vol. 2680, no. 1, 2023, doi: https://doi.org/10.1063/5.0127077

[9] H. Setiawan, et al., *Psikologi Industri dan Organisasi*: *Konsep dan Studi Kasus dalam Industri dan Organisasi*. In C. Nanny Mayasari, S.Pd., M.Pd. (Ed.). Book Chapter (1st ed., pp. 149–163). Indonesia: Get Press, 2023.

[10] K. E. Kroemer Elbert, H. B. Kroemer, and A. D. Kroemer Hoffman, "Designing to Fit the Moving Body," in Handbook of Ergonomics: How to Design for Ease and Efficiency, Book chapter (3 ed. pp. 379-441) Cambridge, Massachusetts, USA: Academic Press, 2018.
[11] H. Setiawan and M. Rinamurti, "Recommendations of ergonomic checkpoints and total ergonomics intervention in the pempek kemplang palembang industry". *IOP Conf. Ser.: Mater. Sci. Eng.* 885 012057, 2020, doi: https://doi.Org/10.1088/1757-899X/885/1/012057
[12] H Setiawan and M Rinamurti, "Pemberdayaan Masyarakat Melalui Pelatihan Ergo-Entrepreneurship Untuk Meningkatkan Kualitas Hidup dan Sikap Kewirausahaan Karyawan Pembuat Pempek PT Cita Rasa Palembang", J*urnal Pengabdian kepada Masyarakat Universitas Bina Darma*, vol.1, no. 1, pp. 1-12, 2021, doi: https://doi.org/10.33557/pengabdian.v1i1.1338
[13] H. Setiawan, S. Susanto, M. Rinamurti, A. Alfian, Y.D. Pratama, D. Budiarto, and C. Clara, "Ergo-Technopreneurship Training to Improve Knowledge and Attitude of Technology Entrepreneurs Palembang Local Culinary Traders", *Journal Ekuisci*, vol. 2, no.4, pp.226–236. 2025, doi: https://doi.org/10.62885/ekuisci.v2i4.633
[14] W. Susihono and I. P. Gede Adiatmika, "Assessment of inhaled dust by workers and suspended dust for pollution control change and ergonomic intervention in metal casting industry: A cross-sectional study," Heliyon, vol. 6, no. 5, p. e04067, 2020, doi: 10.1016/j.heliyon.2020.e04067.
[15] A. F. Hansen et al., "Participatory ergonomics: What works for whom and why? A realist review.," Ergonomics, pp. 1–21, Apr. 2023, doi: 10.1080/00140139.2023.2202842.
[16] E. N. S. Yuliani, I. P. G. Adiatmika, K. Tirtayasa, and N. Adiputra, "Implementation of a total ergonomics approach in reducing work fatigue: Literature study," J. Appl. Ind. Eng., vol. 3, no. 2, pp. 207–214, 2021.
[17] M. Yusuf, L. Sudiajeng, K. A. Suryawan, and I. M. Sudana, "Redesign of Ergonomic Worktables in Reinforced Concrete Sheet Works Reduce Ergonomic Risk Level," in Proceedings of the 5th International Conference on Applied Science and Technology on Engineering Science iCAST-ES, ScitePress Digital Library, 2022, pp. 370–374. doi: 10.5220/0011806000003575.
[18] H. Setiawan, S. Susanto, M. Rinamurti, A. Alfian, Y.D. Pratama, and D. Budiarto, "Design of a Round Tofu Printer Using the Ergo-Product Design Method: (Case Study: Mr. Andi's Tofu Factory Palembang)", *Jurnal Improsci*, vol.2, no.4, pp.234–245. 2025, doi: https://doi.org/10.62885/improsci.v2i4.614
[19] M. Yusuf, I Ketut Gde Juli Suarbawa, and I Made Anom Santiana, "Analysis of potential ergonomic hazards in metal craft welding workers," Int. J. Occup. Saf. Heal., vol. 15, no. 2 SE-Original Articles, pp. 165–172, Apr. 2025, doi: 10.3126/ijosh.v15i2.66529.
[20] T. Budiyanto, M. Yusuf, and B. P. K. As'ari, "The Relationship Between Noise and Temperature to the Level of Work Fatigue in Workers in the Cutting Section," Am. J. Sci. Eng. Technol., vol. 8, no. 3, pp. 141–145, Jul. 2023, doi: 10.11648/j.ajset.20230803.13.
[21] I. K. G. J. Suarbawa, M. Yusuf, and L. Sudiajeng, "Ergonomic Factors Which Affect the Work Productivity of Clove Flower Harvesters," Int. J. Adv. Sci. Eng. Inf. Technol., vol. 14, no. 2 SE-Articles, pp. 675–682, Apr. 2024, doi: 10.18517/ijaseit.14.2.19783.
[22] I. M. Sudana and M. Yusuf, "Design of Ergonomic Flour Dough Mixer with Participatory Approach to Increase Work Productivity MSME Employees," Eur. J. Appl. Sci. Eng. Technol., vol. 2, no. 5 SE-Articles, pp. 80–87, Sep. 2024, doi: 10.59324/ejaset.2024.2(5).09.
[23] M.-G. Garcia, M. G. Roman, A. Davila, and B. J. Martin, "Comparison of Physiological Effects Induced by Two Compression Stockings and Regular Socks During Prolonged Standing Work," Hum. Factors, vol. 65, no. 4, pp. 562–574, Jun. 2021, doi: 10.1177/00187208211022126.
[24] H. Setiawan, S. Susanto, M. Rinamurti, and Y.D. Pratama, "Implementation of A Total Ergonomics Approach To Improve the Quality of Life of Freight Workers In 16 Ilir Market, Palembang City, South Sumatera Province", *Journal of Medisci,* vol. 2, no. 3, pp.172–182, 2024, doi: https://doi.org/10.62885/medisci.v2i3.596
[25] H. Setiawan, S. Susanto, D. Budiarto, Y.D. Pratama, and A. Alfian, "Recommendations for Sustainable Waste Management Technology in Palembang City", *Jurnal Agrosci*, vol.2, no.4, pp.254–266, 2025, doi: https://doi.org/10.62885/agrosci.v2i4.641
[26] V. Kamala, and T.P. Robert, "Fuzzy-Logic-Based Ergonomic Assessment in an Automotive Industry", *South African Journal of Industrial Engineering*, vol. 33, no.4, pp. 109–125, 2022, doi: https://doi.org/10.7166/33-4-2593
[27] N. M. Hawari, R. Sulaiman, K. M. Kamarudin, and R. C. Me, "Musculoskeletal Discomfort Evaluation using Rapid Entire Body Assessment (REBA) and Quick Exposure Check (QEC) among Woodworking Workers in Selangor, Malaysia," Asian J. Appl. Sci., vol. 10, no. 5 SE-Articles, 2022, doi: 10.24203/ajas.v10i5.7047
[28] M. Mazni, M. Noorezam, and Z. Zulkafli, "The Design of An Ergonomic Wheelchair", *Malaysian Journal of Industrial Technology,* vol. 5 no. 4, pp. 28-33, 2021.

LOGIC
Journal of Engineering Design and Technology
Vol. 25 No.3 November ; p. 186-193

p-ISSN : 1412-114X
e-ISSN : 2580-5649
http://ojs2.pnb.ac.id/index.php/LOGIC

INFLUENCE OF WORKPLACE ENVIRONMENT AND ERGONOMIC POSTURE ON MUSCULOSKELETAL DISORDERS IN TRADITIONAL GAMELAN CRAFT WORKERS IN BALI

I Ketut Gde Juli Suarbawa [1)*], M. Yusuf [1)], I Made Suarta [1)], I Gede Oka Pujihadi [1)]

1) Mechanical Engineering Department, Politeknik Negeri Bali, Bali, Indonesia

Correponding email [1)] : julisuarbawa@pnb.ac.id

Abstract. This study investigates the effect of work posture and workplace environmental conditions on musculoskeletal disorders (MSDs) and fatigue among traditional gamelan craftsmen in Bali, Indonesia. Using a pre-experimental one-group pretest–posttest design, fifty-one male workers were assessed using the Nordic Body Map (NBM), the EORTC QLQ-C30 fatigue scale, and the Rapid Upper Limb Assessment (RULA). The results showed a significant increase in MSD scores from 29.72 to 48.90 and fatigue scores from 31.06 to 44.26 after a single four-hour work session ($p < 0.001$). RULA analysis indicated that 100% of workers performed tasks in moderate- to high-risk postures, with 36.8% requiring immediate ergonomic intervention. The most affected anatomical regions included the lower back, upper back, neck, and thighs. These findings suggest that prolonged static postures, floor-level working positions, and suboptimal workplace environmental conditions substantially contribute to physical strain. The results highlight the urgent need for ergonomic interventions tailored to traditional craft industries to reduce cumulative trauma risks and improve worker well-being.

Keywords : Fatigue, Ergonomic Posture, Musculoskeletal Disorders, Work Environment.

1. INTRODUCTION

Musculoskeletal disorders (MSDs) are among the leading causes of disability and reduced productivity worldwide. The World Health Organization [1] reports that over 1.7 billion people suffer from MSDs, accounting for a giant share of non-communicable sickness burdens worldwide. In particular, low back pain is the single biggest contributor to years lived with disability (YLDs), affecting almost 570 million humans globally. These problems not only reduce work capacity and quality of life but also pose good sized financial burdens on healthcare systems and employers because of absenteeism and early retirement [2].

MSDs are regularly related to a mixture of biomechanical, organizational, and environmental risk factors, together with repetitive motion, sustained awkward postures, prolonged static loading, and suboptimal environmental conditions like insufficient lighting, ventilation, or temperature control [3], [4]. Whilst a developing frame of literature has explored those danger factors in formal industrial settings, there may be still limited understanding approximately their incidence and contributing factors in casual and traditional work environments, particularly in low- and center-profits international locations.

One such understudied sector is the traditional craft industry, particularly the small-scale manufacturing of Balinese gamelan musical instruments. Artisans in this sector typically perform labor-intensive tasks such as metal forging, carving, and assembling in poorly ventilated, high-temperature environments, often in seated or crouched postures for extended periods. These physical conditions, combined with limited ergonomic awareness and the absence of proper tools or workstation design, make these workers highly susceptible to musculoskeletal health risks. What makes Balinese gamelan craftsmen unique compared to other artisanal or industrial workers is the strong cultural tradition that shapes their work practices; most production processes are carried out on the floor

without adjustable work surfaces, requiring prolonged forward bending, repetitive forceful hammering, and precision movements to achieve the desired acoustic quality. These culturally embedded and physically demanding methods create ergonomic burdens rarely seen in other craft industries, placing gamelan workers at a significantly higher risk of musculoskeletal disorders. Preliminary evidence from neighborhood studies indicates that extra than 80% of gamelan craftsmen record neck, shoulder, and lower back pain [5], yet comprehensive, data-driven studies continue to be scarce.

An evaluation of present literature reveals that most ergonomic research have focused on massive-scale manufacturing, healthcare, or workplace-based totally occupations, where interventions together with sit down-stand desks, ergonomic chairs, or automation are feasible [6]. However, these findings are not easily generalizable to informal sectors that operate with limited resources and culturally embedded work practices. Furthermore, although several studies have assessed postural risks using tools such as RULA or REBA, only a few have simultaneously examined environmental factors including temperature, lighting, and humidity and how these factors interact with ergonomic posture to influence MSD outcomes.

A scientific overview of musculoskeletal problems in handicraft employees stated symptom prevalence starting from 38.5% to 100%, predominantly affecting the neck, back, knees, and upper limbs [7]. Postural factors (awkward positions, repetitive movements), lengthy working hours, and task repetitiveness had been noticeably related to MSD rates. But, research overwhelmingly targeted on formal occupational settings, with scant interest to informal craft sectors wherein infrastructure boundaries extensively shape ergonomics chance exposure. MDPI posted a 2021 observe extending the RULA device for hand-made informal sector. All 18 contributors were categorised at high or very excessive ergonomic hazard, highlighting the pressing need for interventions that keep in mind unstructured workflow and informal workstations [8]. Likewise, research of bamboo craftsmen in Thailand suggested that over 96% of workers sat at the floor, with close to-typical neck flexion and trunk bending. RULA ratings averaged degree four indicating immediate correction required and MSD occurrence passed 85% [9]. Further, precision handicraft people in India exhibited excessive fees of neck (61.6%), lower back (74.8%), and knee (54.7%) issues. Regression evaluation diagnosed age, enjoy, extended awkward posture, continuous work without breaks, and high working demands as enormous predictors of MSD signs and symptoms [10]. In another context, Ethiopian self-hired tailors verified good sized institutions among neck–shoulder pain and elements inclusive of awkward static posture, repetitive motions, and restricted breaks [11]. Those findings strengthen the generalizability of MSD risk factors across various informal sectors, suggesting that ergonomic vulnerabilities be successful in environments with restrained assets and restrained formal education.

This review reveals a critical research gap: there is limited empirical knowledge of how combined physical and environmental workplace factors contribute to MSDs in traditional, culturally significant industries such as gamelan production. This increases numerous critical studies questions: To what quantity does the physical work surroundings (e.g., heat exposure, lighting situations, ventilation) contribute to the development or worsening of musculoskeletal symptoms among gamelan craftsmen?

To address these questions, the existing look at aims to research the influence of the workplace environment and ergonomic posture on the superiority and severity of musculoskeletal issues amongst conventional gamelan craft people in Bali. This study employs a mixed-methods approach by combining direct measurements of environmental parameters (temperature, humidity, and lighting) with an ergonomic posture assessment and self-reported musculoskeletal symptoms using the Nordic Body Map questionnaire. The underlying hypothesis is that suboptimal environmental conditions, when combined with prolonged non-neutral postures, significantly increase the likelihood and severity of MSDs among these workers. To date, such an integrated assessment remains limited in traditional craft settings, making this study an important contribution to understanding how multiple workplace factors simultaneously influence musculoskeletal health.

In addition to its methodological approach, the present research offers a distinctive contribution to the field of occupational health and ergonomics. It examines a unique worker population often overlooked in existing literature and provides evidence on how combined physical and environmental factors interact to shape MSD risk in traditional, resource-limited craft environments. First, it focuses on a unique population-artisans working in traditional, informal settings-that is largely overlooked in contemporary MSD research. Second, it integrates physical and environmental risk assessments, supplying a extra holistic knowledge of the multifactorial nature of MSDs. Third, by means of grounding the analysis in a culturally precise context, it opens pathways for designing domestically appropriate, low-price ergonomic interventions aimed toward retaining worker health without disrupting conventional craftsmanship. similarly, the examine contributes the broader dialogue about fairness approximately fairness in occupational health studies. Informal and culturally rooted labor sectors regularly fall outside the purview of labor rules and occupational protection requirements. consequently, evidence generated from this examine has the potential to inform centered policies and interventions that may lessen health disparities and improve operating situations in small-scale, traditional industries. ultimately, improving ergonomics and environmental situations inside the gamelan industry no longer most effective complements worker nicely-being but additionally enables preserve the continuity of an vital detail of Balinese cultural heritage.

2. METHODS

2.1 Research Design

This study employed a pre-experimental, one-group pretest-posttest layout, commonly utilized in ergonomic subject studies in which randomization is infeasible due to ethical or contextual obstacles [12]. The layout enabled within-subject comparisons of musculoskeletal complaints and fatigue symptoms earlier than and after a complete work in a natural occupational setting. This design is particularly suitable for small-scale informal sectors, where ergonomic dangers are structurally embedded and tough to govern experimentally [3]. The combination of observational ergonomic tools and subjective self-reporting supplied each quantitative and qualitative insights into quick-time period physiological responses to working conditions.

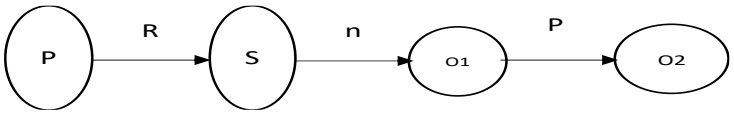

Figure 1. Research design

Information:
P : Population
R : Randomize
n : Number of selected samples
O1 : Pretest measurement unit
O2 : Posttest measurement unit
P : Treatment (Bronze Metal Forging Work Activities)

2.2 Participants

A total of 51 male gamelan craftsmen from Tihingan Village, Klungkung, Bali, were recruited using a total population sampling strategy. The total number of active craftsmen in the village is approximately 256 individuals, making the sample size equal to nearly 20% of the overall population. This proportion is considered sufficiently representative for occupational ergonomics research, particularly in small, homogeneous artisan communities where work tasks and environmental conditions are relatively uniform. Such sampling approaches are also consistent with previous ergonomics studies conducted in traditional craft industries [11]. Eligibility standards covered: (1) energetic involvement in forging or assembling gamelan devices for at least 12 months; (2) age range 20–56 years; (3) body mass index between 18–22; and (4) no musculoskeletal damage that would interfere with posture evaluation. All members provided knowledgeable consent in compliance with ethical requirements.

2.3 Data Collection

Musculoskeletal issues were measured using RULA and the Nordic body Map (NBM) tool [13], administered earlier than and after work session (08:00–12:00 WITA). The NBM captures localized discomfort across 27 anatomical areas. Previous research confirm its validity and sensitivity for discipline-primarily based MSD assessments [14]. Fatigue was assessed using an adapted version of the EORTC QLQ-C30 fatigue subscale, which has demonstrated high reliability in physically demanding occupations [15]. The instrument evaluates physical and emotional fatigue using a 4-point Likert scale. Postural danger became assessed the usage of the Rapid Upper Limb Assessment (RULA) tool [16], a longtime observational technique for detecting ergonomic dangers associated with top extremity postures. Observations were performed during peak activity periods and scored independently by trained ergonomists. RULA action levels (1–4) had been used to categorize the urgency of intervention. Despite the fact that no virtual sensors were deployed, field notes indicated accelerated ambient temperature (29–33°C), low light levels (< 300 lux), and minimum mechanical ventilation. these situations had been triangulated against symptom ratings to discover environmental contributions to fatigue and MSD improvement, aligning with environmental threat methodologies in [3], [4].

2.4 Data Analysis

Data were analyzed using IBM SPSS Statistics 23.0. Descriptive statistics (mean, SD, frequencies) described participant characteristics and symptom prevalence. The Shapiro–Wilk test assessed normality of difference ratings. Since the data were normally distributed, paired sample t-assessments were conducted to evaluate modifications in musculoskeletal complaints and fatigue degrees before and after working. RULA rankings were presented categorically consistent with action levels, and frequencies have been analyzed to decide the proportion of workers requiring ergonomic intervention. Comparative results from the NBM confirmed increased prevalence of pain post-shift in more than one anatomical areas, particularly the lower back, neck, and thighs. This increase was statistically significant ($p < 0.001$).

3. RESULTS AND DISCUSSION

3.1 Result

Participant Characteristics

A total of 51 male gamelan craftsmen participated in this study. The mean age of the participants was 40.24 years (SD = 5.01), with an average height of 161.32 cm (SD = 8.22) and an average body weight of 61.06 kg (SD = 6.44). The mean Body Mass Index (BMI) was 20.32 (SD = 1.15), indicating a generally normal nutritional status. Participants had an average work experience of 7.70 years (SD = 3.21), and the majority were engaged full-time in manual forging activities performed in floor-seated positions. These demographic characteristics are consistent with previous studies conducted in low-resource occupational environments [10].

Table 1. Participant Characteristics (N = 51)

Variable	Mean ± SD	Range
Age (years)	40.24 ± 5.01	28 – 51
Height (cm)	161.32 ± 8.22	149 – 179
Weight (kg)	61.06 ± 6.44	45 – 75
BMI (kg/m²)	20.32 ± 1.15	18.01–22.00
Work Experience (yr)	7.70 ± 3.21	2 – 18

Pre- and Post-Work Fatigue and MSD Scores

Musculoskeletal discomfort and fatigue had been measured both before and after work. As illustrated in Figure 2, mean musculoskeletal disease (MSD) scores increased from 29.72 (SD = 0.51) before work to 48.90 (SD = 3.27) after work. Fatigue ratings additionally showed a large growth from 31.06 (SD = 0.43) to 44.26 (SD = 2.12) post-work. both variations had been statistically big ($p < 0.001$) the usage of paired-pattern t-exams, confirming the extreme bodily burden imposed with the aid of the work shift. Bar chart showing post-work increases in MSD (+64.65%) and fatigue (+42.5%) scores.

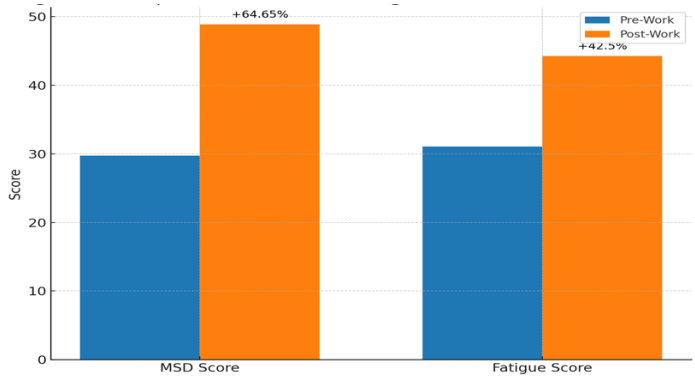

Figure 2. Comparison of MSD and Fatigue Scores Before and After Work

Table 2. Paired t-Test Results for MSD and Fatigue Scores

Variable	Pre-Test Mean ± SD	Post-Test Mean ± SD	t-value	p-value
MSD Score	29.72 ± 0.51	48.90 ± 3.27	13.832	<0.001
Fatigue Score	31.06 ± 0.43	44.26 ± 2.12	12.752	<0.001

Ergonomic Posture Risk (RULA)

RULA (Rapid Upper Limb Assessment) results revealed that all participants exhibited work postures classified as high ergonomic risk. Specifically, 63.2% of respondents scored within Action Level 3 (scores 5–6), indicating that corrective measures are needed soon, while the remaining 36.8% fell into Action Level 4 (score 7), requiring immediate ergonomic intervention.

Table 3. Distribution of RULA Scores Among Participants

RULA Action Level	Score Range	n	Percentage (%)
Level 3	5–6	32	63.2%
Level 4	7	19	36.8%

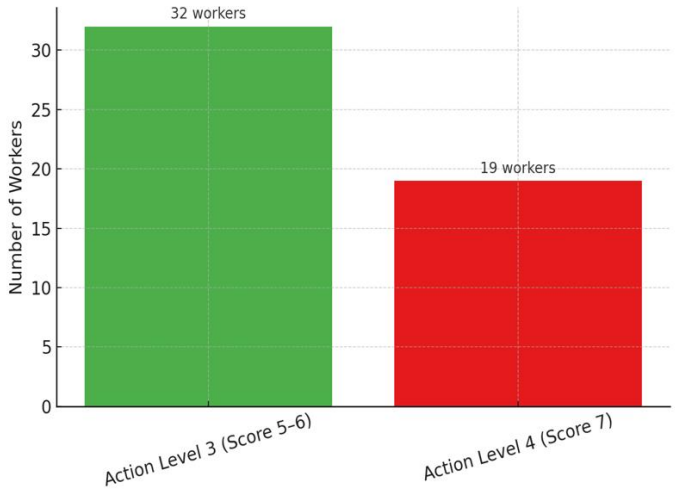

Figure 3. RULA action level distribution

Musculoskeletal Complaints by Body Region (NBM)

Post-work Nordic Body Map (NBM) data showed that the most frequently affected anatomical regions were the lower back (48 reports), upper back (45 reports), neck (42 reports), and thighs (40 reports). These areas correspond to the sustained forward-leaning posture and unsupported lower-limb positioning commonly observed during metal forging and engraving tasks.

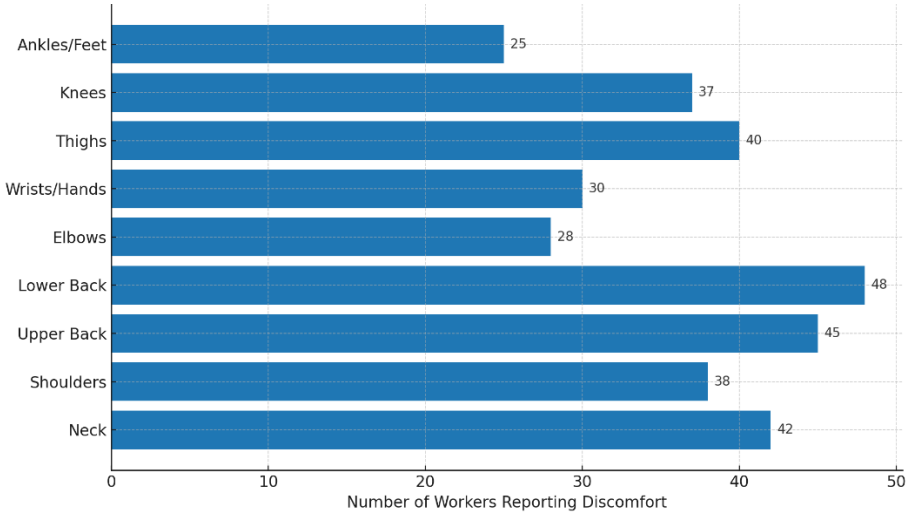

Figure 4. Distribution of musculoskeletal complaints by body region (post-work NBM)

A horizontal bar chart indicating the frequency of discomfort reports across nine key body regions. This body-vicinity-precise evaluation reinforces the link among extended static postures, floor-seated working positions, and the onset of acute musculoskeletal symptoms. All normality assumptions were satisfied (Shapiro–Wilk check $p > 0.05$), and coupled sample t-tests revealed quite large increases in both MSD and fatigue ratings post-work. moreover, posture chance evaluation showed that 100% of individuals operated in conditions requiring ergonomic

interest. those effects together exhibit the urgent need for workplace redesign, task rotation, and posture modification in conventional gamelan manufacturing to prevent long-term musculoskeletal injury.

3.2. Discussion

This study investigated the acute effects of traditional gamelan forging on musculoskeletal disorders (MSDs) and fatigue levels among 51 workers in Bali. The results revealed significant increases in both MSD scores and fatigue post-shift, with high ergonomic risk (RULA) confirmed for all participants. These findings warrant urgent ergonomic improvements.

Increased MSD and Fatigue Scores

The increases in MSD scores (from 29.72 to 48.90) and fatigue scores (from 31.06 to 44.26) after the work session mirror earlier findings showing substantial intra-day rises in musculoskeletal strain among manual workers [17]. The use of combined pre/post assessments and posture observations is well established in ergonomic studies of artisanal and informal sectors [11], [18]. Numerically, the magnitude of MSD increase in this study is comparable to pre-intervention MSD levels above 40 reported among traditional metal-casting workers [19]. Similar acute increases have also been noted in repetitive or static ICT tasks, demonstrating that even short work periods can rapidly accumulate physical strain.

Postural Risk and Body Region Pain Patterns

RULA analysis classified 100% of participants in Action Levels 3 or 4, with 36.8% requiring immediate intervention. This is comparable to findings in informal welding sectors, where more than 70% of workers exhibited non-neutral postures associated with high MSD incidence [20]. Post-work NBM scores in this study also showed the highest discomfort in the lower back, upper back, neck, and thighs, a pattern consistent with ergonomic studies in other informal craft settings, where MSD prevalence in these regions commonly exceeds 60–80% [21]. These similarities indicate that the combination of sustained bending, floor-seated positions, and repetitive hammering places gamelan craftsmen at musculoskeletal risk levels comparable to other high-risk informal occupations.

Contextualizing Environmental Factors

Although environmental factors were not measured quantitatively, field observations indicated heat exposure of 29–33 °C, illumination below 300 lux, and minimal ventilation conditions known to aggravate MSD risk. These findings align with Zare et al. [4] who demonstrated that improving lighting to above 500 lux and reducing workspace temperature by 2–3 °C significantly decreased musculoskeletal complaints. Similar ergonomic interventions in congested manual labor settings, such as the use of proper tools and scheduled rest breaks, have also been shown to lower MSD and fatigue levels by 20–30%, reinforcing the influence of environmental stressors in this study.

Comparison with Multicomponent Interventions

Systematic reviews affirm that ergonomic techniques combining bodily, instructional, and organizational additives produce the greatest reductions in MSD and fatigue signs and symptoms. As an example, nurses receiving multicomponent interventions demonstrated sizeable decreases in MSD incidence and fatigue [22]. Those interventions typically incorporate posture schooling, progressed tool use, environmental modifications, and scheduled relaxation factors together absent within the unergonomic gamelan work environment.

Implications for Ergonomic Design in Traditional Workplaces

The evidence shows that a multifaceted ergonomic software comprising posture education, tool redesign, environmental adjustments (e.g. cooling, lighting), and participatory design may want to drastically reduce MSD risk in gamelan employees. [19] stated advantageous results on lower back, thigh, and fatigue proceedings after a blended intervention package. Likewise, case research in traditional metallic-casting environments located sustained advantages at one and 8 months submit-intervention with similar strategies.

Study Limitations

This study's pre–post single-organization design limits causal inference, and environmental variables were qualitatively determined in place of measured instrumentally. Future research should establish objective measurements (e.g., lux meters, heat indices, airflow sensors) and randomized or controlled designs to validate those findings

4. CONCLUSION

This study provides compelling proof that traditional gamelan manufacturing in Bali exposes employees to large ergonomic and physiological risks. Using a pretest–posttest design, we found a substantial increase in

musculoskeletal complaints and fatigue degrees after a single work session. MSD ratings rose by using 64.7% and fatigue by using 42.5%, with pain most frequently reported in the lower back, upper back, neck, and thighs. We also found that all participants worked in postures categorised as medium to high ergonomic hazard, with over one-third requiring on the spot intervention. Those findings aid the hypothesis that non-impartial postures, prolonged ground-seated positions, and insufficient environmental situations (e.g., excessive heat, terrible lighting) immediately contribute to physical strain amongst craft people. The pattern of complaints is consistent with previous studies in informal and traditional sectors, reinforcing the pressing need for focused ergonomic strategies. To guard the health and productiveness of these culturally essential artisans, we recommend enforcing a complete ergonomic intervention application. Such interventions need to encompass posture schooling, device and workstation redesign, environmental manage, and participatory ergonomic practices tailored to neighborhood situations. Without such action, the risk of cumulative trauma and long-term disability amongst gamelan craftsmen is probably to persist or worsen.

5. ACKNOWLEDGEMENT

The authors would like to express sincere gratitude to the Ministry of Higher Education, Science, and Technology, as well as the Center for Research and Community Service of the Bali State Polytechnic, for providing funding, which enabled the successful completion of this study and the creation of a publishable article.

6. REFERENCES

[1] World Health Organization, “Musculoskeletal health,” https://www.who.int/news-room/fact-sheets/detail/musculoskeletal-conditions.
[2] F. Jiang, C. Lu, Z. Zeng, Z. Sun, and Y. Qiu, “Global burden of disease for musculoskeletal disorders in all age groups, from 2024 to 2050, and a bibliometric-based survey of the status of research in geriatrics, geriatric orthopedics, and geriatric orthopedic diseases,” J Orthop Surg Res, vol. 20, no. 1, p. 179, Feb. 2025, doi: 10.1186/s13018-025-05580-y.
[3] T. T. T. Le, W. Jalayondeja, K. Mekhora, P. Bhuuanantanondh, and C. Jalayondeja, “Prevalence and risk factors of work-related musculoskeletal disorders among physical therapists in Ho Chi Minh City, Vietnam,” BMC Public Health, vol. 24, no. 1, p. 6, Jan. 2024, doi: 10.1186/s12889-023-17527-1.
[4] M. Zare, N. Black, J. C. Sagot, G. Hunault, and Y. Roquelaure, “Ergonomics interventions to reduce musculoskeletal risk factors in a truck manufacturing plant,” Int J Ind Ergon, vol. 75, Jan. 2020, doi: 10.1016/j.ergon.2019.102896.
[5] K. Tirtayasa, N. Adiputra, and I. G. Djestawana, “THE CHANGE OF WORKING POSTURE IN MANGGUR DECREASES CARDIOVASCULAR LOAD AND MUSCULOSKELETAL COMPLAINTS AMONG BALINESE GAMELAN CRAFTSMEN,” 2003.
[6] P. Kotnik and N. Koprivnik, “Musculoskeletal Disorders in the Workplace of Physiotherapists: Occupational Risk Factors and Their Role in Prevention and Management: A Systematic Review,” Open Access Maced J Med Sci, vol. 12, no. 2, pp. 347–355, Jun. 2024, doi: 10.3889/oamjms.2024.11900.
[7] D. Das, A. Kumar, and M. Sharma, “A systematic review of work-related musculoskeletal disorders among handicraft workers,” International Journal of Occupational Safety and Ergonomics, vol. 26, no. 1, pp. 55–70, Jan. 2020, doi: 10.1080/10803548.2018.1458487.
[8] B. Shezi, R. A. Street, A. Mathee, N. Cele, S. Ndabandaba, and R. N. Naidoo, “Ergonomic Risk Assessment during an Informal Hand-Made Cookware Operation: Extending an Existing Model,” Int J Environ Res Public Health, vol. 18, no. 18, p. 9459, Sep. 2021, doi: 10.3390/ijerph18189459.
[9] Araya, Chawapornpan, and Thanee, “Ergonomic Factors and Musculoskeletal Disorders Among Bamboo Handicraft Workers,” Nurs J (Manila), vol. 47, no. 2, pp. 38–49, Apr. 2024.
[10] D. Das and A. K. Singh, “Risk factors associated with work-related musculoskeletal disorders among floor-sitting precision handicraft workers,” Int Arch Occup Environ Health, vol. 95, no. 5, pp. 1129–1145, Jul. 2022, doi: 10.1007/s00420-021-01817-5.
[11] T. H. Mekonnen, D. G. Yenealem, and D. M. Geberu, “Physical environmental and occupational factors inducing work-related neck and shoulder pains among self-employed tailors of informal sectors in Ethiopia, 2019: results from a community based cross-sectional study,” BMC Public Health, vol. 20, no. 1, p. 1265, Dec. 2020, doi: 10.1186/s12889-020-09351-8.
[12] D. Kee, “Characteristics of Work-Related Musculoskeletal Disorders in Korea,” Int J Environ Res Public Health, vol. 20, no. 2, Jan. 2023, doi: 10.3390/ijerph20021024.
[13] I. Kuorinka et al., “Standardised Nordic questionnaires for the analysis of musculoskeletal symptoms,” Appl Ergon, vol. 18, no. 3, pp. 233–237, 1987.
[14] A. Ispășoiu and I. Milosan, “Ergonomic Risk Assessment In Certain Industrial Fields Using The Qec And Rula Methods,” Review of the Air Force Academy, vol. XXI, no. 1, pp. 47–55, Oct. 2023, doi: 10.19062/1842-9238.2023.21.1.6.

[15] A. Penson et al., "Short fatigue questionnaire: Screening for severe fatigue.," J Psychosom Res, vol. 137, Oct. 2020, doi: 10.1016/j.jpsychores.2020.110229.
[16] L. McAtamney and E. Nigel Corlett, "RULA: a survey method for the investigation of work-related upper limb disorders," Appl Ergon, vol. 24, no. 2, pp. 91–99, Apr. 1993, doi: 10.1016/0003-6870(93)90080-S.
[17] L. Tang, G. Wang, W. Zhang, and J. Zhou, "The prevalence of MSDs and the associated risk factors in nurses of China," Int J Ind Ergon, vol. 87, p. 103239, Jan. 2022, doi: 10.1016/j.ergon.2021.103239.
[18] T. T. T. Le, "Test-retest reliability of the Nordic Musculoskeletal questionnaire (NMQ) in Vietnamese physical therapists," TẠP CHÍ KHOA HỌC TRƯỜNG ĐẠI HỌC QUỐC TẾ HỒNG BÀNG, vol. 4, pp. 81–86, Jun. 2023, doi: 10.59294/HIUJS.VOL.4.2023.389.
[19] W. Susihono and I. P. G. Adiatmika, "The effects of ergonomic intervention on the musculoskeletal complaints and fatigue experienced by workers in the traditional metal casting industry," Heliyon, vol. 7, no. 2, Feb. 2021, doi: 10.1016/j.heliyon.2021.e06171.
[20] S. Suherdin and S. Kartadarma, "Ergonomic Hazard Control Modeling for Informal Welding Workers in Greater Bandung: A Study on Musculoskeletal Disorders (MSDs)," Jurnal Ilmu Kesehatan Masyarakat, vol. 16, no. 1, pp. 18–31, Mar. 2025, doi: 10.26553/jikm.2025.16.1.18-31.
[21] W. Santos et al., "Efficacy of Ergonomic Interventions on Work-Related Musculoskeletal Pain: A Systematic Review and Meta-Analysis," J Clin Med, vol. 14, no. 9, p. 3034, Apr. 2025, doi: 10.3390/jcm14093034.
[22] G. Krishnanmoorthy, S. Rampal, S. R. Karuthan, F. Baharudin, and R. Krishna, "Effectiveness of Participatory Ergonomic Interventions on Work-Related Musculoskeletal Disorders, Sick Absenteeism, and Work Performance Among Nurses: Systematic Review," JMIR Hum Factors, vol. 12, pp. e68522–e68522, Jun. 2025, doi: 10.2196/68522.

LOGIC
Journal of Engineering Design and Technology
Vol. Vol. 25 No.3 November ; p. 194-200

p-ISSN : 1412-114X
e-ISSN : 2580-5649
http://ojs2.pnb.ac.id/index.php/LOGIC

THERMAL PERFORMANCE ANALYSIS OF TIO_2 AND PARAFFIN AS PHASE CHANGE MATERIALS

I Made Arsawan [1,3], IDG Ary Subagia [2,3]*, IKG Wirawan[2], DNK Putra Negara [2], NW Sugiarti [3]

1) Mechanical Engineering Departement, Politeknik Negeri Bali, Jl. Kampus Bukit Jimbaran, Badung-Bali-Indonesia.
2) Study Program of Mechanical Engineering, Engineering Faculty, Udayana University, Kampus Bukit Jimbaran, (80361), Badung-Bali-Indonesia.
3) Engineering Materials Laboratory, Engineering Faculty, Udayana University, Kampus Bukit Jimbaran, (80361), Badung-Bali-Indonesia.

Corresponding email [2*]: arsubmt@unud.ac.id

Abstract. Phase change materials (PCMs) are materials that can store and release thermal energy through phase changes from solid to liquid at specific temperatures. This study aims to analyze the effect of TiO_2 concentration in paraffin as a phase change material for thermal energy storage applications. TiO_2 is used as an additive to paraffin to enhance thermal conductivity and accelerate heat transfer, thus improving the performance of the phase change material (PCM). This research investigates the thermal characteristics of the paraffin and TiO_2 mixture by measuring thermal properties such as melting point, heat capacity, thermal stability, and the energy storage capability of the material using techniques such as Differential Scanning Calorimetry (DSC). The results show that the addition of TiO_2 can enhance the thermal performance of pure paraffin as a phase change material. A concentration of 10% TiO_2 can absorb thermal energy up to 94.58 kJ/kg. This study is expected to contribute to the development of more efficient energy storage materials.

Keywords: Latent Heat Phase, Change Material Composite, Thermal Conductivity, Thermal Energy Storage, Thermal Performance Analysis.

1. INTRODUCTION

Phase change materials (PCMs) are capable of absorbing and releasing heat energy in the form of latent heat during phase transition processes. Paraffin is one of the most commonly used types of PCM due to its several advantages, such as chemical stability, non-corrosiveness, and relatively low cost [1-3]. However, paraffin has a limitation in its low thermal conductivity, which hinders the efficiency of heat transfer during the melting and solidifying processes [4-6].

To address the limitation of low thermal conductivity in paraffin, various PCM composites have been developed by incorporating high-conductivity materials such as expanded graphite, aluminium, TiO_2, and coconut-shell carbon. Previous studies have reported significant enhancements; for example, the addition of 10–20 wt% expanded graphite increased the thermal conductivity of paraffin from approximately 0.25 W/m·K to 2–5 W/m·K [7–9]. Aluminium particles at concentrations of 5–15 wt% have been shown to improve thermal conductivity by 50–200% [10–11], while 5–10 wt% coconut-shell carbon resulted in an increase of around 30–70% [12–13].

The use of TiO_2 as an additive in PCM has also been widely investigated. Studies conducted in [14–18] demonstrated that incorporating 1–15 wt% TiO_2 can enhance the thermal conductivity of paraffin by approximately 20–90%, depending on particle size and dispersion quality. In addition to improving thermal conductivity, TiO_2 contributes to thermal stability; for instance, the addition of 10 wt% TiO_2 has been reported to reduce the rate of temperature fluctuation during heating and cooling cycles by up to 25%, thereby improving resistance to thermal degradation and enhancing stability during repeated operational cycles [19].

TiO_2 particles typically have a nanometres size, ranging from approximately 20 nm to 180 nm, depending on the synthesis method and thermal treatment [20]. The small particle size and almost homogeneous distribution can increase the surface area and interaction between TiO_2 and the PCM matrix, enhancing thermal conductivity and mechanical stability of the PCM. TiO_2 has a surface morphology that can be in the form of spherical particles or other steric shapes with a tendency to agglomerate when the concentration is too high. A uniformly distributed morphology and slightly surface roughness can enhance the heat transfer efficiency and energy circulation during

the phase change process [21-22].

The use of TiO_2 as a thermal energy storage material combined with paraffin wax is expected to provide a good solution for the development of thermal energy storage (TES). The concentration of TiO_2 in paraffin wax is studied to determine the optimum concentration for the development of thermal energy storage materials.

2. METHODS

2.1 Material

The materials used in this study are paraffin wax, titanium iso-propoxide ($TiOR_4$), ethanol (EtOH), and distilled water (H_2O). The paraffin wax utilised in this study was obtained from PT. Aneka Kimia Inti (Indonesia) to ensure material traceability and reproducibility. Its detailed specifications are provided in Table 1 [23].

Table 1. Characterization of Paraffin Wax.

Temp. Melting (°C)	Heat of Fusion (kJ/kg)	Thermal Conductivity (W/mK)	Density (kg/m3)
64	266	0,339 (solid 45,70C)	916 (solid 24^0C)

2.2 TiO_2 Synthesis

The TiO_2 material used in the experiment was obtained from titanium iso-propoxide via the sol-gel method. The sol–gel method was chosen for this study because it enables a more homogeneous dispersion of particles within the paraffin matrix, allows better control over particle morphology and size, and facilitates the formation of a stable porous structure that helps to prevent PCM leakage during phase transitions. In addition, the sol–gel process can be carried out at relatively low temperatures, thereby minimising paraffin degradation and enhancing the thermal stability of the composite. These advantages make the sol–gel method more suitable than conventional synthesis techniques for producing PCM composites with improved thermal performance. The initial step involved performing hydrolysis and condensation processes. In the hydrolysis stage, titanium iso-propoxide was dissolved in ethanol (EtOH) and hydrolyzed by the addition of distilled water (H_2O) with the following reaction:

$$Ti(OR)_4 + H_2O \longrightarrow Ti(OH)_4 + ROH$$

The titanium hydroxide formed will precipitate as a solid in the solution, marking the initial step in the Sol-Gel process. The next step is the condensation process, where a transition occurs from sol to gel. The hydroxide ions (OH) produced from the hydrolysis of the metal precursor with alcohol (ROH) undergo a condensation reaction, forming bonds between the oxygen (O) atoms in the hydroxide. The result of this condensation process is the formation of a three-dimensional network (gel) from the oxygen particles that begin to form solid material. The reaction that occurs is:

$$Ti(OH)_4 \longrightarrow TiO_2 + H_2O$$

In this reaction, the Titanium Hydroxide molecules undergo condensation to form Titanium Dioxide (TiO_2) and water molecules (H2O). This process involves the bonding of oxygen atoms within the hydroxide, resulting in the formation of a solid material in the form of a gel consisting of TiO_2.

2.3 Preparation Composite PCM (Paraffin Wax-TiO_2)

The PCM composite was synthesised through a three-step preparation process, as illustrated in Figure 1. In Step 1, the raw materials—paraffin wax and TiO_2 derived from the sol–gel process—were prepared and weighed according to the desired composition. In Step 2, the paraffin was placed into a beaker and heated on a magnetic stirrer until fully melted at 100 °C. The temperature was then reduced to 70 °C, and the mixture was stirred at 60 rpm while TiO_2 powder was gradually introduced to ensure uniform dispersion. The mixing process was continued for 2 hours to obtain a homogeneous paraffin-TiO_2 (PCM PT) composite. In Step 3, the molten mixture was cast into a mould and allowed to solidify before being subjected to thermal characterisation tests.

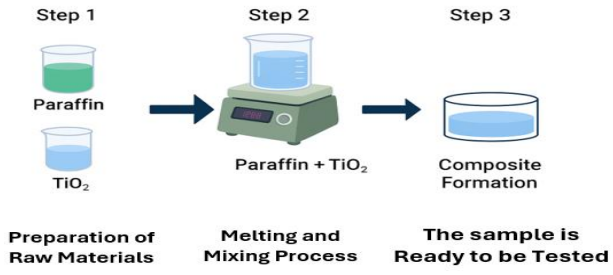

Figure 1. Schematic Diagram of PCM Composite Preparation

The testing process of the samples was carried out at various concentrations of TiO_2 in paraffin wax. The composition of the samples is presented in Table 2.

Table 2. Composition of TiO_2 and paraffin wax mixture for PCM.

Sample Code	Sample Description	Paraffin (%)	TiO_2 (%)
PCM PP	Pure paraffin	100	0
PCM PT 5%	Paraffin composite with 5 wt.% TiO_2	95	5
PCM PT 10%	Paraffin composite with 10 wt.% TiO_2	90	10
PCM PT 15%	Paraffin composite with 15 wt.% TiO_2	85	15

2.4 Research Variables

The variables in this study consist of independent and dependent variables. The independent variable in this study is the PCM material, which is the concentration of TiO_2 in paraffin, while the dependent variable is the thermal characteristics of the PCM material.

2.5 Material Characterization

The characterisation of the PCM material was conducted to determine the physical and thermal properties of each prepared sample. The thermal behaviour of pure paraffin and the composite PCM was analysed using Differential Scanning Calorimetry (DSC), performed at a heating/cooling rate of 10 °C/min within a temperature range of 20–80 °C under a nitrogen atmosphere (100 mL/min). Thermal stability was assessed using Thermogravimetric Analysis (TGA, Q50) with a heating rate of 10 °C/min from 30 to 550 °C, also under nitrogen flow. The rate of mass loss with increasing temperature was further evaluated using Derivative Thermogravimetry (DTG) to identify decomposition stages.

3. RESULTS AND DISCUSSION

3.1 Thermal Energy Absorption Capacity of PCM

The DSC test results showed that the addition of TiO_2 into paraffin altered the thermal properties of the PCM, as demonstrated in Figure 2.

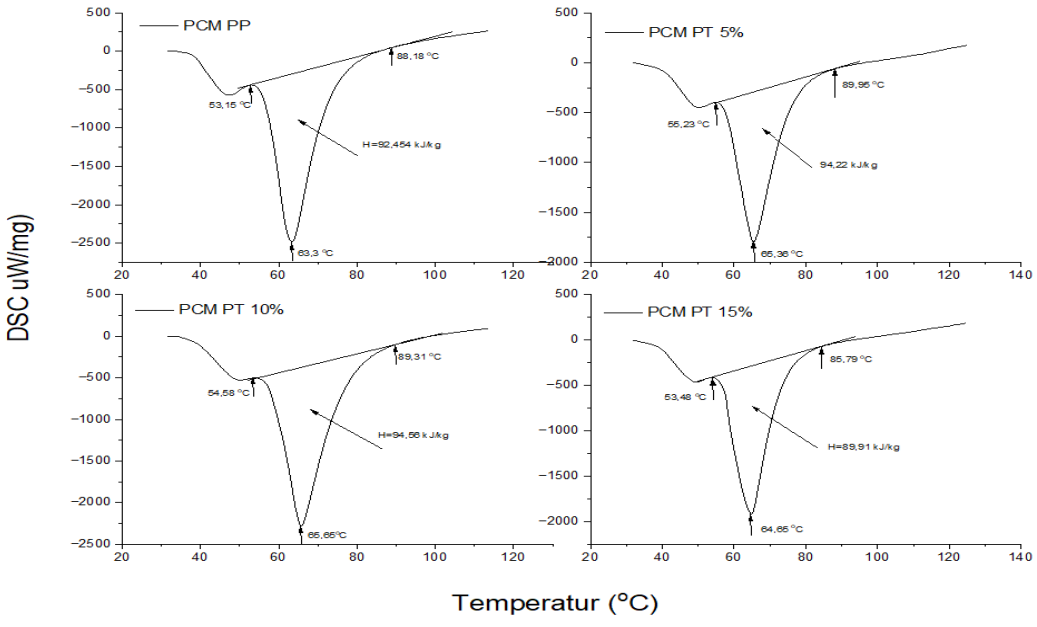

Figure 2. DSC test results of PCM material with various TiO_2 concentrations in paraffin

Figure 2 shows the DSC test results of PCM materials, which include paraffin wax (pure PCM) and a mixture of paraffin wax and TiO_2 (PCM PT). For pure PCM, an endothermic peak (heat absorption) occurs around 53.15-89.18 °C. The area under the curve for this peak is 92.45 kJ/kg, indicating the melting enthalpy (ΔH), which is the energy required to melt the paraffin. For the PCM with a 95% paraffin wax and 5% TiO_2 mixture, the endothermic peak occurs at temperatures between 55.23-89.95°C, and the area under the curve for this peak is 94.22 kJ/kg, showing the melting enthalpy (ΔH), which is the energy required to melt the PCM PT 5%. In this condition, the

melting point occurs at 65.36°C. For the PCM with a 90% paraffin wax and 10% TiO_2 mixture, the onset of melting occurs at 54.58°C, and the end-set of melting occurs at 89.31°C. The melting point of this PCM PT 10% is 65.65°C. The total heat absorbed during the endothermic process reaches 94.56 kJ/kg. At a TiO_2 concentration of 15%, the initial melting process begins at 53.48°C, the melting point occurs at 64.65°C, and the endset of melting occurs at 85.79°C. The total heat required for this PCM to change from solid to liquid is 89.91 kJ/kg. The detailed results are presented in Table 3.

Table 3. Thermal transition parameters of PCM

Sample	Onset (°C)	Melting point (°C)	Endset (°C)	ΔH (kJ/kg)
PCM PP	53.15	63.30	89.18	92.45
PCM PT 5%	55.23	65.36	89.95	94.22
PCM PT 10%	54.58	65.65	89.31	94.56
PCM PT 15%	53.48	64.65	85.79	89.91

The results of these tests show a shift in the on-set melting and end set melting when TiO_2 is added to pure PCM. The addition of TiO_2 into paraffin increases the on-set melting and end-set melting of the PCM material, except for the addition of 15% TiO_2 into paraffin. The on-set and end-set melting shift because TiO_2 particles interact with the paraffin molecular chains, limiting the free movement of the molecules during the melting process, which results in either an increase or decrease in the initial melting temperature. The on-set melting depends on how well TiO_2 is dispersed in the paraffin matrix. At 5% and 10% TiO_2 compositions, both the on-set and end-set slightly increase, indicating enhanced local thermal stability. However, at 15%, the values slightly decrease due to possible agglomeration. TiO_2 increases the thermal conductivity of the mixture, leading to more uniform heat distribution during heating. This can cause a more uniform melting process but also affects the on-set and end-set temperatures depending on the heat distribution and particle size. If the TiO_2 particles are evenly distributed, they can act as nucleation centers that stabilize the melting process, increasing the on-set /end-set temperatures. However, if particle agglomeration occurs, as may happen with 15% TiO_2, it can disrupt the paraffin crystal structure, lowering the on-set /end-set melting temperatures. From Figure 2, the optimal composition in terms of thermal stability and enthalpy occurs in the PCM with 5%–10% TiO_2 content, while 15% TiO_2 tends to cause a decrease in performance.

Looking at the specific heat capacity (Cp) of the PCM produced, it is observed that the higher the TiO_2 concentration in the PCM, the greater the specific heat capacity of the material, as shown in Figure 3.

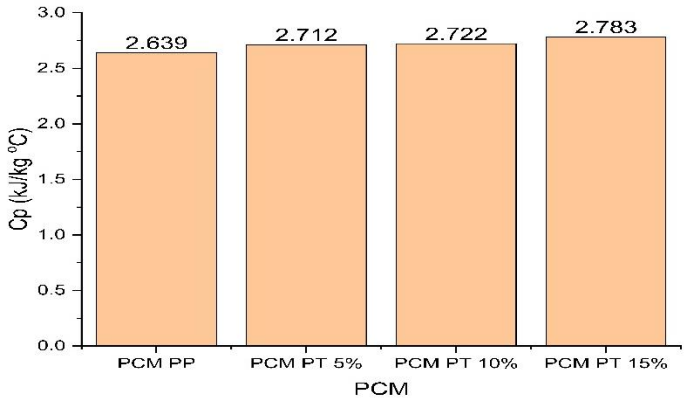

Figure 3. Specific heat capacity of PCM material with TiO_2 concentrations

Specific heat capacity (Cp) is the amount of heat energy required to raise the temperature of one unit mass of a substance by one degree Celsius (°C) or one Kelvin (K) without a phase change. Compared to Figure 2, there is a phenomenon where, at a TiO_2 concentration of 15% in paraffin, the amount of heat energy that can be absorbed by the PCM is the lowest compared to the other PCMs. However, the specific heat capacity at 15% TiO_2 concentration is the highest. This phenomenon contradicts the equation $Q = m.Cp.\Delta T$, where an increase in Cp should result in a higher Q. In Figure 2, when the TiO_2 concentration reaches 15%, a portion of the paraffin fraction decreases due to the dispersion of more TiO_2 particles, which, by volume, do not contribute to the latent heat release/absorption like paraffin. This reduces the amount of material actively undergoing phase changes, resulting in a lower total ΔH. At TiO_2 concentrations of 5%-10%, TiO_2 helps improve heat distribution without significantly disrupting the phase change of paraffin. However, at a TiO_2 concentration of 15%, aggregation or saturation of TiO_2 particles can occur, leading to a hindrance in the movement of paraffin molecules during melting or freezing, and a reduction in the effective paraffin mass fraction capable of contributing to the phase change. At a 15% TiO_2 concentration, interactions between TiO_2 particles can form more efficient thermal pathways (increasing Cp), but

on the other hand, they create a microstructure that limits the crystallization or perfect melting of paraffin, which impacts the melting enthalpy.

3.2 Thermal Stability of PCM

The thermal stability of the PCM can be observed from the TGA and DTG test results, as shown in Figures 4 and 5. The thermal stability of the PCM material, as shown in Figure 4, indicates that all PCMs demonstrate good thermal stability below 250°C, as evidenced by the lack of significant mass reduction up to 250°C. Figure 5, which presents the DTG test results of various PCM materials consisting of paraffin and TiO_2, shows that all samples exhibit a melting peak in the same temperature range, between 50–70°C, which corresponds to the characteristics of paraffin. The addition of TiO_2 to paraffin modifies the peak intensity and thermal stability. At a 15% TiO_2 concentration, a significant change is observed with a much larger peak, which may indicate a catalytic effect or chemical interaction between TiO_2 and paraffin. The addition of TiO_2 particles to paraffin-based PCM affects the phase transition process and the thermal stability of the material. Although the melting point remains similar, the intensity and mass change profile vary, indicating thermal modification and changes in the melting kinetics.

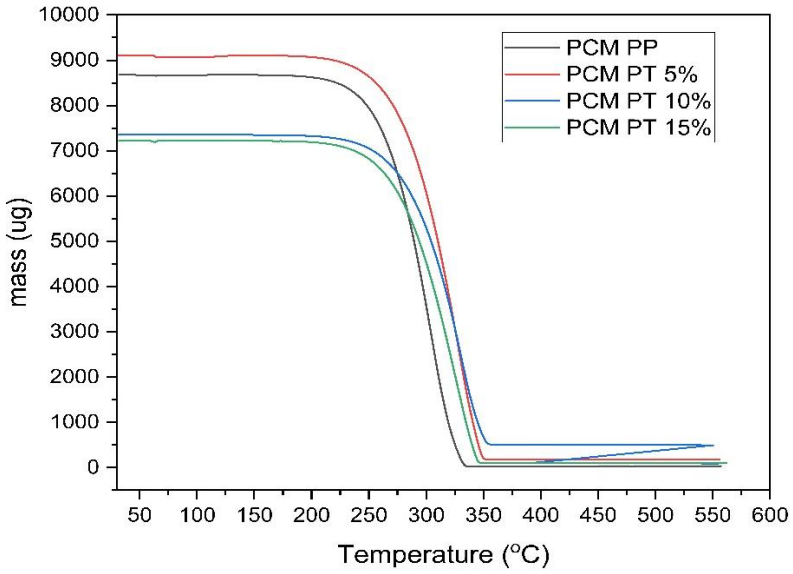

Figure 4. TGA test results of PCM PP and PCM with a mixture of paraffin wax and TiO_2

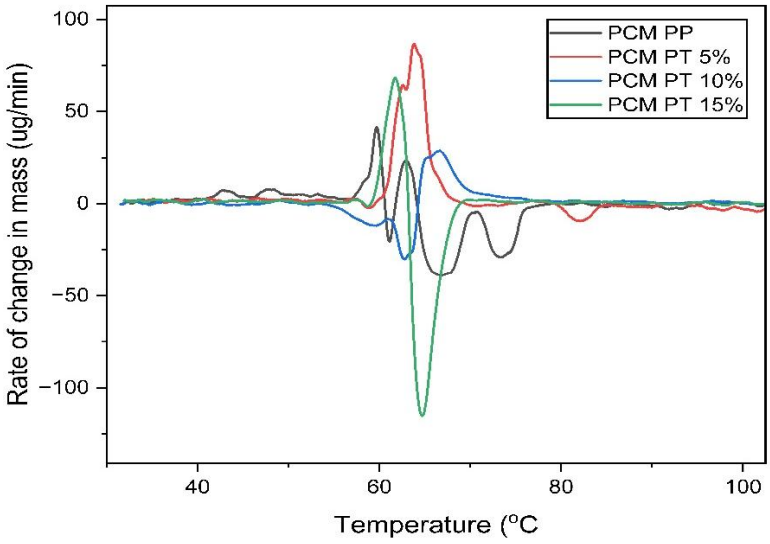

Figure 5. DTG test results of PCM PP and PCM with a mixture of paraffin wax and TiO_2

The DTG curves provide a more detailed representation of the thermal degradation mechanism Figure 5. The incorporation of TiO_2 causes a slight shift in the DTG peak temperature and broadening of the decomposition profile. This phenomenon suggests an interaction between paraffin molecules and the surface of TiO_2 particles,

which restricts molecular mobility. As a result, a higher amount of energy is required for chain scission, thereby enhancing the thermal stability of the composite.

At a TiO_2 concentration of 15 wt%, the DTG peak becomes sharper and more pronounced. This may indicate a catalytic effect or specific chemical interactions between TiO_2 and paraffin. A sharper peak implies a more uniform degradation process, suggesting stronger interfacial interactions or a more homogeneous dispersion of TiO_2 within the paraffin matrix. Variations in DTG peak intensity and temperature confirm that TiO_2 acts not merely as an inert filler, but actively modifies the thermal decomposition mechanism. These kinetic changes are associated with enhanced heat-transfer pathways, alterations in crystallisation behaviour, and a possible partial confinement effect induced by the TiO_2 surface. Although TiO_2 affects the degradation characteristics, the melting peak remains within the range of 50–70 °C, indicating that the phase-change mechanism is not disrupted. This is crucial, as the performance of PCMs depends heavily on consistent melting–solidification temperatures. Overall, the DTG analysis demonstrates that TiO_2 improves the thermal resistance of paraffin-based PCMs by regulating molecular mobility, modifying decomposition kinetics, and strengthening interfacial interactions. These enhancements are most pronounced at higher TiO_2 concentrations, highlighting its strong potential as an effective thermal stabiliser in PCM composites.

4. CONCLUSION

The thermal analysis results demonstrate that the incorporation of TiO_2 into pure paraffin induces notable changes in the thermal behaviour of the PCM. The addition of TiO_2 enhances the specific heat capacity of the material, indicating improved heat-storage ability. Among the tested samples, the PCM containing 10 wt% TiO_2 exhibits the highest latent heat absorption, reaching 94.56 kJ/kg. Furthermore, the presence of TiO_2 particles significantly influences both the phase-transition characteristics and the thermal stability of paraffin-based PCM, indicating that TiO_2 acts not only as a filler but also as a functional additive capable of modifying the thermal performance of the composite.

5. ACKNOWLEDGEMENT

The author wishes to acknowledge and thank all individuals and organizations that have contributed to the preparation of this article. While this work represents an important step, it remains incomplete and will require further enhancement through subsequent studies, with the objective of identifying an efficient and environmentally sustainable thermal energy storage material.

6. REFERENCES

[1] C. J. Ho and J. Y. Gao, “An experimental study on melting heat transfer of paraffin dispersed with Al2O3 nanoparticles in a vertical enclosure,” *Int. J. Heat Mass Transf.*, vol. 62, no. 1, 2013, doi: 10.1016/j.ijheatmasstransfer.2013.02.065.

[2] Z. Khan, Z. Khan, and A. Ghafoor, “A review of performance enhancement of PCM based latent heat storage system within the context of materials, thermal stability and compatibility,” Energy Conversion and Management, vol. 115, pp. 132-158 2016, doi: 10.1016/j.enconman.2016.02.045.

[3] Z. N. Meng and P. Zhang, “Experimental and numerical investigation of a tube-in-tank latent thermal energy storage unit using composite PCM,” *Appl. Energy*, vol. 190, 2017, doi: 10.1016/j.apenergy.2016.12.163.

[4] A. Arshad, M. Jabbal, L. Shi, J. Darkwa, N. J. Weston, and Y. Yan, “Development of TiO_2/RT–35HC based nanocomposite phase change materials (NCPCMs) for thermal management applications,” *Sustain. Energy Technol. Assessments*, vol. 43, 2021, doi: 10.1016/j.seta.2020.100865.

[5] Y. Lin, Y. Jia, G. Alva, and G. Fang, “Review on thermal conductivity enhancement, thermal properties and applications of phase change materials in thermal energy storage,” Renewable and Sustainable Energy Reviews, vol. 82, part.3, pp. 2730-2742, 2018, doi: 10.1016/j.rser.2017.10.002.

[6] H. Mhiri, A. Jemni, and H. Sammouda, “Numerical and experimental investigations of melting process of composite material (nanoPCM/carbon foam) used for thermal energy storage,” *J. Energy Storage*, vol. 29, 2020, doi: 10.1016/j.est.2019.101167.

[7] X. Chen, P. Cheng, Z. Tang, X. Xu, H. Gao, and G. Wang, “Carbon-Based Composite Phase Change Materials for Thermal Energy Storage, Transfer, and Conversion,” Advanced Science, vol. 8, issue. 9, article no. 2001274, 2021. doi: 10.1002/advs.202001274.

[8] P. Goli, S. Legedza, A. Dhar, R. Salgado, J. Renteria, and A. A. Balandin, “Graphene-enhanced hybrid phase change materials for thermal management of Li-ion batteries,” *J. Power Sources*, vol. 248, 2014, doi: 10.1016/j.jpowsour.2013.08.135.

[9] M. Malik, I. Dincer, M. Rosen, and M. Fowler, “Experimental Investigation of a New Passive Thermal Management System for a Li-Ion Battery Pack Using Phase Change Composite Material,” *Electrochim. Acta*, vol. 257, 2017, doi: 10.1016/j.electacta.2017.10.051.

[10] J. R. Patel and M. K. Rathod, “Recent developments in the passive and hybrid thermal management

techniques of lithium-ion batteries," Journal of Power Sources, vol. 480, article no. 228820, 2020, doi: 10.1016/j.jpowsour.2020.228820.
[11] W. Li, Y. Dong, X. Zhang, and X. Liu, "Preparation and performance analysis of graphite additive/paraffin composite phase change materials," *Processes*, vol. 7, no. 7, 2019, doi: 10.3390/pr7070447.
[12] P. Mantilla Gilart, Á. Yedra Martínez, M. González Barriuso, and C. Manteca Martínez, "Development of PCM/carbon-based composite materials," *Sol. Energy Mater. Sol. Cells*, vol. 107, 2012, doi: 10.1016/j.solmat.2012.06.014.
[13] F. Bahiraei, A. Fartaj, and G. A. Nazri, "Experimental and numerical investigation on the performance of carbon-based nanoenhanced phase change materials for thermal management applications," *Energy Convers. Manag.*, vol. 153, 2017, doi: 10.1016/j.enconman.2017.09.065.
[14] Y. Li, J. Li, Y. Deng, W. Guan, X. Wang, and T. Qian, "Preparation of paraffin/porous TiO_2 foams with enhanced thermal conductivity as PCM, by covering the TiO_2 surface with a carbon layer," *Appl. Energy*, vol. 171, 2016, doi: 10.1016/j.apenergy.2016.03.010.
[15] S. A. Mansour, A. A. Atwa, E. M. Farag, and R. A. Elsad, "Thermal properties investigation of paraffin wax/titania nanocomposites as phase change materials," *J. Therm. Anal. Calorim.*, vol. 148, no. 19, 2023, doi: 10.1007/s10973-023-12354-3.
[16] S. Sami and N. Etesami, "Improving thermal characteristics and stability of phase change material containing TiO_2 nanoparticles after thermal cycles for energy storage," *Appl. Therm. Eng.*, vol. 124, 2017, doi: 10.1016/j.applthermaleng.2017.06.023.
[17] S. I. Ibrahim *et al.*, "Stability and thermal conductivity of different nano-composite material prepared for thermal energy storage applications," *South African J. Chem. Eng.*, vol. 39, 2022, doi: 10.1016/j.sajce.2021.11.010.
[18] C. Li, H. Yu, Y. Song, M. Wang, and Z. Liu, "A n-octadecane/hierarchically porous TiO_2 form-stable PCM for thermal energy storage," *Renew. Energy*, vol. 145, 2020, doi: 10.1016/j.renene.2019.06.070.
[19] I. Arsawan, I. Negara, and I. Pujihadi, "Utilization of Parafin and TiO_2 as Phase Change Materials (PCM) for Processor Coolers," Proceedings of the 5th International Conference on Applied Science and Technology on Engineering Science (iCAST-ES 2022), pp. 732-740, 2023. doi: 10.5220/0011875800003575.
[20] E. Supriyanto, A. Holikin, and Suwardiyanto, " The thermal annealing effect on Crystal Structure and Morphology of Titanium Dioxide (TiO2) Powder," *J. ILMU DASAR*, vol. 15, no. 1, pp. 37-41, 2015, doi:10.19184/jid.v15i1.638
[21] N. Shabrina, G. Yudoyono, and S. Sudarsono, "Karakterisasi Struktur, Morfologi, dan Sifat Optik Lapisan Tipis Titanium Dioksida yang Dideposisi Menggunakan Teknik Spray Pyrolysis," *J. Sains dan Seni ITS*, vol. 11, no. 5, 2023, doi: 10.12962/j23373520.v11i5.108566.
[22] R. Prasetyawati, H. Ahmad, Marfuatun, , "Struktur Morfologi, Komposisi Kimia Dan Resistansi Lapisan TiO_2-Cu Sebagai Lapisan Aktif Pada Sel Surya Fotoelektrokimia," *J. Fis. Unnes*, vol. 3, no. 2, pp. 128-131, 2013, doi: 10.15294/jf.v3i2.3822
[23] B. Zalba, J. M. Marín, L. F. Cabeza, and H. Mehling, "Review on thermal energy storage with phase change: Materials, heat transfer analysis and applications," Applied Thermal Engineering, vol. 23, pp. 251-283, 2003. doi: 10.1016/S1359-4311(02)00192-8.

LOGIC
Journal of Engineering Design and Technology
Vol. 25 No.3 November; p. 201-209

p-ISSN : 1412-114X
e-ISSN : 2580-5649
http://ojs2.pnb.ac.id/index.php/LOGIC

COMPREHENSIVE ANALYSIS ON THE INFLUENCE OF FLAP WIDTH ON THE HYDRODYNAMIC PARAMETERS OF OWSC DEVICES

Rasya Aulia Nathania Nisa[1)], James Julian[1)*], Fitri Wahyuni[1)], Riki Hendra Purba[1)], Fathin Muhammad Mahdhudhu[2)], Elvi Armadani[3)]

1) Department of Mechanical Engineering, Universitas Pembangunan Nasional Veteran Jakarta, Jakarta, Indonesia
2) Department of Naval Architecture, Universitas Pembangunan Nasional Veteran Jakarta, Jakarta, Indonesia
3) Department of Industrial Engineering, Universitas Pembangunan Nasional Veteran Jakarta, Jakarta, Indonesia

Corresponding email [1)] : zames@upnvj.ac.id

Abstract. The growing need for renewable energy has driven significant interest in harnessing ocean wave power, particularly through Oscillating Wave Surge Converters (OWSCs). This study focuses on examining the effect of flap width on the hydrodynamic capacity of an OWSC, as flap geometry plays a crucial role in energy capture efficiency. A numerical methodology utilizing the Boundary Element Method (BEM) was employed to assess hydrodynamic parameters across both temporal and frequency domains. Five flap width variations were tested under regular wave conditions with different periods, while mesh independence and validation against experimental data ensured accuracy. The results in the time domain revealed a direct correlation between flap width and angular deviation, velocity, torque, and power output, although wider flaps exhibited less stability due to increased inertia. Frequency domain analysis indicated that each flap width had a distinct resonant peak, with narrower flaps performing best at shorter periods and wider flaps at longer ones. Notably, moderately sized flaps (W2 and W3) achieved the highest efficiency, with Capture Width Ratios exceeding 70%, outperforming wider flaps despite their larger surface area. These findings highlight the importance of optimized flap width for efficient and reliable OWSC design.

Keywords: Flap Width, Hydrodynamic, OWSC, Time Domain, Wave Energy.

1. INTRODUCTION

The global energy sector faces critical challenges due to its reliance on finite and environmentally damaging non-renewable sources, which contribute to climate change and geopolitical instability. This pushes for a diversification into renewable energy technologies [1], [2]. Ocean wave energy, presenting a substantial and largely unexplored source for clean power generation, is estimated to have a global potential of 2 TW [3], [4], [5]. The core challenge lies in developing efficient and cost-effective devices, known as Wave Energy Converters (WECs), to harness this mechanical energy. One effective WEC design is the Oscillating Wave Surge Converter (OWSC), which typically employs a hinged flap responding to the horizontal surge motion of waves to drive a Power Take-Off (PTO) system, converting the mechanical energy into electricity [6]. OWSCs are generally preferred for deployment in nearshore environments due to their accessibility, design simplicity, and high efficiency in capturing energy [7]. These features have made OWSC devices the focus of many studies, many of which focus on enhancing the performance of the device.

Various studies have shown that multiple design parameters, including the size, shape, and submergence of the flap, influence the performance of an OWSC. One study by Lin et. al analyzes the effect of plate geometry parameters such as width, thickness, cross-section, and number of segments on the performance of an OWSC. The study concluded that cross cross-section and width of the plate have a distinct influence on its performance [8]. Nevertheless, this study does not provide a detailed analysis of the hydrodynamic characteristics of the device. Another study by Cui et. al investigates the effect of cross-sectional shapes of the flap on the performance of the device, which resulted in the rectangular shape as the best configuration for capturing energy [7]. However, this study is limited to 2D cases, so it does not consider the width or volume of the flap. Furthermore, a study by Anggara et. al further highlights that the dimensional parameters, namely the ratio of width to thickness, of the

flap govern the performance of the device [9]. Nonetheless, as this study investigates the ratio of two dimensions where one dimension is constrained by the other, it does not give an analysis of the individual dimensions of the flap. Although a study by Wang et al. [10] examined the effect of flap width on an OWSC's performance, it concentrated solely on the frequency domain hydrodynamic parameters.

From the previous studies, it can be inferred that flap dimensions influence the energy capture of the wave. However, these studies lack detailed, hydrodynamic investigations on the effect of specific and individual dimensions of the flap. Therefore, the main objective of this study is to investigate the effect of flap width on the flap hydrodynamic parameters of an OWSC. Furthermore, this study offers a novelty by providing an analysis of both the frequency domain and time domain, allowing for a detailed understanding of these parameters. This is crucial for optimizing the design to produce stable and consistent power output, which is essential for integration into the electrical grid. Additionally, time-domain hydrodynamic parameters will provide valuable insights into how to fine-tune OWSC designs to maximize power generation, thereby contributing to the development of a more reliable and efficient wave energy sector.

2. METHODS

2.1 Design of the Variations

This research investigates the hydrodynamic parameters of various widths on an OWSC. The selection of these flap dimensions was based on the dimensions of the experimental prototype by Wei et al (shown by W3 variation), which then the width variations are selected with a difference of 0.2 m. This technology is a type of WEC that harvests the surging kinetic energy of waves using a hinged flap. As a response to the surging wave, the flap will oscillate and then transfer the energy to a hydraulic power system [6]. This study's geometry is based on the model employed in an experimental investigation by Wei et al. [11]. This is carried out because the model is sufficiently compatible to be computed using the numerical approach used in this study, in addition to serving as a validation reference to preserve data actualization. As seen in Figure 1, five width variations are examined while maintaining constant thickness, height, and water depth. The dimension of each variation is shown in Table 1.

Table 1. Flap Dimensions of Each Variation.

Variations	Height (m)	Width (m)	Thickness (m)	Mass (kg)	Water Depth (m)
W1		0.4		2.662	
W2		0.6		4.299	
W3	0.31	0.8	0.0875	5.323	0.305
W4		1		6.654	
W5		1.2		7.985	

2.2 Governing Equations

The Boundary Element Method (BEM) is employed in this study, which involves several equations. The foundation of BEM for wave-body interaction problems is potential flow theory, which makes the assumptions that the fluid is irrotational, inviscid, and incompressible [12]. This method uses Laplace and Bernoulli equations to calculate the forces and torques exerted on the OWSC flap. The linear potential flow theory is crucial for calculating wave forces, with Eq 1 representing the flow field's velocity potential [8]. Eq 2 describes the hydrodynamic characteristics of the flap as a single body in the frequency domain, which includes the added mass matrix, damping matrix, mass matrix, as well as the wave exciting force. The flap's response to a specific wave force with a constant amplitude is calculated with Eq 3 in the time domain [8].

$$\nabla^2\phi(x,y,z,t) = \phi_I(x,y,z,t) + \phi_D(x,y,z,t) + \phi_R(x,y,z,t) = a_w\varphi(x,y,z,t)e^{-i\omega t} \quad (1)$$

$$M\ddot{X}(t) + K\dot{X}(t) + C_h X(t) = F(t) \quad (2)$$

$$\left[-\omega^2 (M_s + M_a(\omega)) - i\omega C(\omega) + K\right] X(\omega) = F(\omega) \quad (3)$$

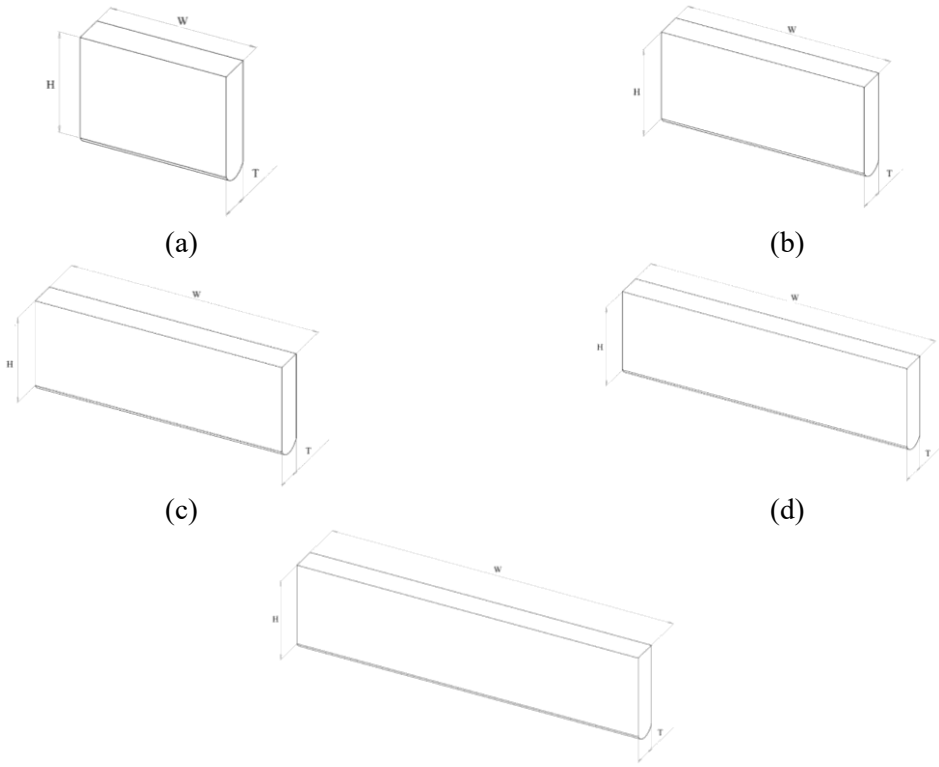

Figure 1. Geometry of width variations used in this study: (a) geometry of width 1 (W1), (b) geometry of width (W2), (c) geometry of width 3 (W3), (d) geometry of width 4 (W4), (e) geometry of width 5 (W5).

2.3 Mesh and Boundary Condition

The meshing process involves dividing geometry into smaller elements, allowing the equations within them to be solved. The preservation of mesh quality is paramount, as it significantly affects the accuracy, convergence, and stability of simulation outcomes. This study employs a quadrilateral mesh, segmenting the flap shape into smaller quadrilateral elements based on the surface domain. Figure 2 presents the mesh configuration.

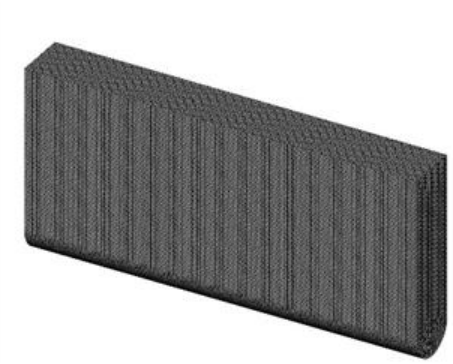

Figure 2. Mesh configuration of the study.

Boundary conditions are also set up to simulate the actual interaction between the flap structure and ocean waves. This study employs a model of waves, which falls under the category of regular waves characterized by a constant amplitude. The ocean wave is modelled using the Airy Wave Theory [12] represented in Eq 4. An analysis of the device's hydrodynamic properties under different wave periods is done with the period variation listed in Table 2.

$$\eta(x,t) = \frac{h}{2}\cos(\omega t - k(x\cos\theta)) \quad (4)$$

Table 2. Ocean wave period variations.

Wave Configuration		
Amplitude (m)	Period (s)	Wavelength (m)
0.1	1.1	1.581
	1.3	1.975
	1.5	2.357
	1.7	2.730
	1.9	3.098
	2.1	3.462
	2.3	3.823
	2.5	4.181
	2.7	4.538
	2.9	4.893

Response data from the interaction between the ocean wave and the OWSC device are analyzed to assess its hydrodynamic properties. Conversely, the device's hydrodynamic performance is achieved by examining several power statistics, including the mechanical power of the device and the power of the wave energy source, which are determined by Eqs (5) and (7), respectively [13]. Eq (6) describes the wave's group velocity, which is used to calculate the power of the wave energy source. Moreover, Eq (8), which also characterizes the device's efficiency, uses the capture width ratio (CWR) equation to determine the device's capacity to capture power.

$$P_w = \frac{1}{2}\rho g A^2 C_g \tag{5}$$

$$C_g = \frac{1}{2} C_p \left\{1 + \frac{kD}{\sinh kD \times \cosh kD}\right\} \tag{6}$$

$$P_{OWSC} = |\, \tau(t) \times \omega(t) \,| \tag{7}$$

$$CWR = \frac{P_{OWSC}}{P_w \times Width} \tag{8}$$

2.4 Mesh Independence Test

This study conducted a grid independence evaluation to examine numerical errors and ensure the model's accuracy. This study adopts the approach introduced by Roache [14]. Three mesh configurations were tested: coarse (13,352 elements), medium (20,642 elements), and fine (30,462 elements), with the number of elements constrained by a specific grid refinement ratio constrained by Eq (9). For each mesh, the maximum absolute amplitude is sampled at a wave amplitude of 0.1 meters and a period of 1.9 seconds. The order of accuracy is determined using Eq (10). The Grid Convergence Index (GCI) evaluates mesh accuracy using two forms: GCI_{fine}, which measures the error between medium and fine meshes, and GCI_{coarse}, which assesses the error between medium and coarse meshes. GCI_{fine} and GCI_{coarse} are formulated in Eq (11) and (12), respectively. To ensure error accuracy, calculations are performed within the convergence region, validated by Eq (14). The final error value for each mesh was then derived from Eq (15). Table 3 presents the results of the mesh independence test. In this table, the maximum response data was taken as sample data from each mesh variation. It can be seen that the variations achieved a convergence index of 1, which is within the convergence region, thus ensuring the accuracy of the error. The result demonstrates that the fine mesh configuration produces the lowest error. Accordingly, this configuration is selected for the study.

$$r = \frac{h_2}{h_1} \tag{9}$$

$$\bar{p} = \frac{\ln\left(\frac{f_3 - f_2}{f_2 - f_1}\right)}{\ln(r)} \quad (10)$$

$$GCI_{fine} = \frac{F_s |\epsilon|}{(r^{\bar{p}} - 1)} \quad (11)$$

$$GCI_{coarse} = \frac{F_s |\epsilon| r^{\bar{p}}}{(r^{\bar{p}} - 1)} \quad (12)$$

$$\epsilon = \frac{f_{n+1} - f_n}{f_n} \quad (13)$$

$$\frac{GCI_{fine}}{GCI_{coarse} r^{\bar{p}}} \approx 1 \quad (14)$$

$$fr_{h=0} = f_1 + \frac{(f_1 - f_2)}{(r^{\bar{p}} - 1)} \quad (15)$$

Table 3. Result of Mesh Independence Test.

Mesh Category	Fine	Medium	Coarse
Maximum Response (m)	57.63967514	57.64332581	57.64648465
$\bar{p}$		0.356885866	
r		1.5	
GCI_{fine}		0.044%	
GCI_{coarse}		0.0508%	
$\frac{GCI_{fine}}{GCI_{coarse}}$		1.000	
$f_{rh}=0$		57.66677285	
Error	0.03518%	0.04066%	0.04699%

3. RESULTS AND DISCUSSION

3.1 Data Validation

To ensure data actualization, data validation analysis was conducted before discussing the main data of the study. This analysis is executed by comparing the flap motion response data obtained through numerical methods with experimental data provided by Wei et. al [11]. This data is taken at a wave parameter of A=0.1m and T=1.9s. Figure 3 shows the comparison between numerical and experimental data. As depicted in the graph, the simulation data closely align with the experimental data points. The two datasets exhibit a high degree of similarity in terms of both frequency and phase angle. While minor variations in the amplitude are present (namely, 6% difference), the overall pattern and trend of the motion response are consistent, confirming the reliability of the numerical approach.

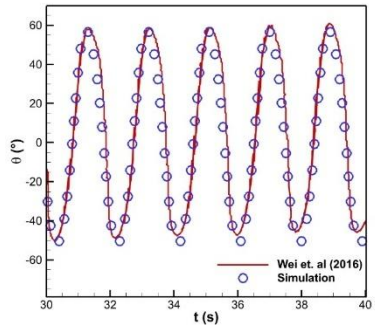

Figure 3. Comparison of experimental and simulation results for motion response at an ocean wave period of 1.9 seconds and an amplitude of 0.1 meters.

3.2 Data Analysis

The first set of data discussed is the hydrodynamic data in the time domain, subjecting the flaps to a wave with a period of 1.3 s and an amplitude of 0.1 m. Figure 4 depicts the motion response of each flap width variation over 40 seconds, showing that the motion for all five configurations is highly periodic and synchronous. A distinct and steady correlation exists between the width of the flap and the degree of angular deviation. As the flap width expands from W1 to W5, the degree of oscillation likewise rises. The widest flap, W5, achieves the largest angular deviation, while the narrowest, W1, has the smallest. This positive correlation occurs because a wider flap presents a larger surface area to the incoming waves, enabling it to absorb more energy. This results in a greater excitation force absorbed and, subsequently, a larger angular displacement.

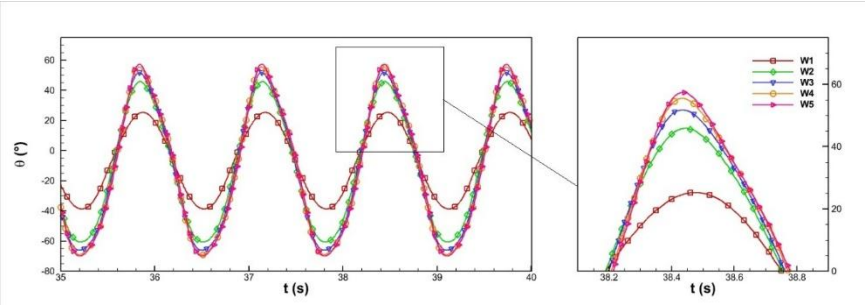

Figure 4. Motion response data of all variations when subjected to an ocean wave with a period of 1.3 seconds and an amplitude of 0.1 meters.

The hydrodynamic analysis reveals a clear proportionality between flap width and energy output parameters, despite the influence of inertial damping. Angular velocity, as shown in Figure 5 (a), is proportional to flap width because wider flaps capture a greater excitation force from the wave, resulting in higher absolute maximum angular velocity. The collateral increase in mass with width increases the inertial force, which acts as a damping force resisting motion, leading to less stable peak-to-trough transitions and greater hydrodynamic nonlinearity in wider flaps [15]. The torque, presented in Figure 5 (b), mirrors this proportionality, showing increased absolute maximum torque with wider flaps and similar trends in stability. An expected phase difference between torque and angular velocity exists, as torque functions as a restoring force opposing acceleration. Consequently, the device's power output, shown in Figure 5 (c) as the absolute product of torque and angular velocity, follows the same pattern: the wider the flap, the higher the power output. This consistently demonstrates that the influence of the absorbed excitation force significantly outweighs the inertial damping effect.

(a)

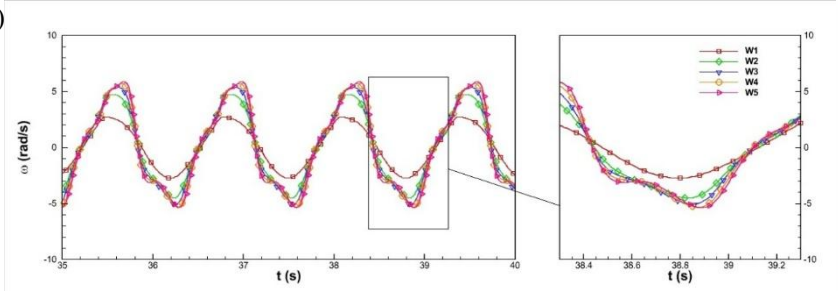

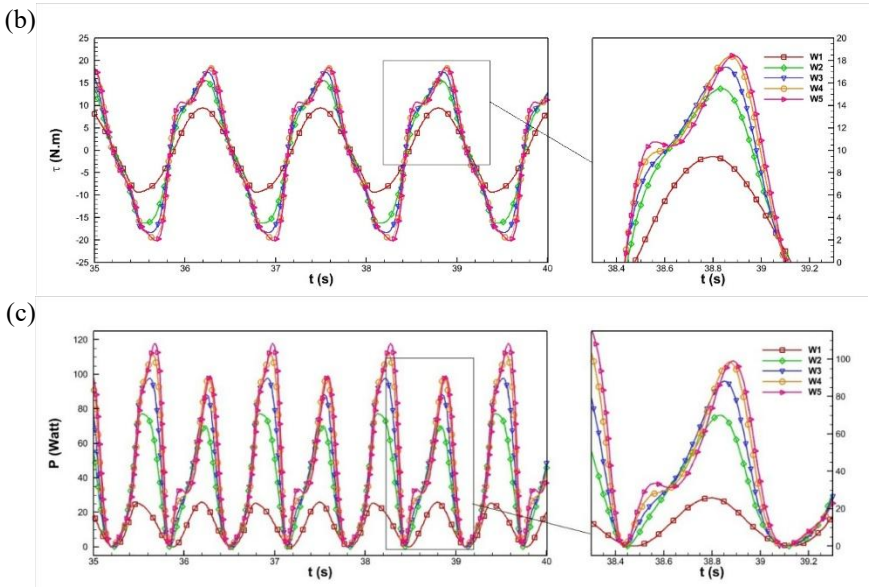

Figure 5. Other hydrodynamic parameters at ocean wave configuration of T=1.3 s and A=0.1 m, (a) angular velocity, (b) torque, and (c) power output.

The analysis of hydrodynamic parameters in the frequency domain reveals a strong dependence on both flap width and wave period across all variations. Figure 6 (a) illustrates that wider flaps (W2-W5) consistently achieve larger maximum angular deviations (motion response) for any given wave period, demonstrating their enhanced capacity for wave energy capture. The peaks across all variations in the maximum response data can be inferred as resonant peaks, which occur when the natural period of the structure aligns with the period of the wave, thus maximizing the motion of the structure [16]. The narrowest flap (W1) peaked sharply at approximately 1.1 seconds, while the wider flaps (W2-W5) are tuned to perform optimally in the longer period range of 1.3 to 1.5 seconds. This resonance phenomenon and the proportional relationship between flap width and performance are consistently reflected in the average angular velocity, average torque, and average power data shown in Figures 6 (b), (c), and (d). For instance, the maximum values for these parameters occur around 1.3 seconds for the wider flaps and 1.1 seconds for the narrowest flap, confirming that the substantial energy absorbed by wider flaps translates into a greater driving force, resulting in higher angular velocity, torque, and power despite traveling a greater angular distance.

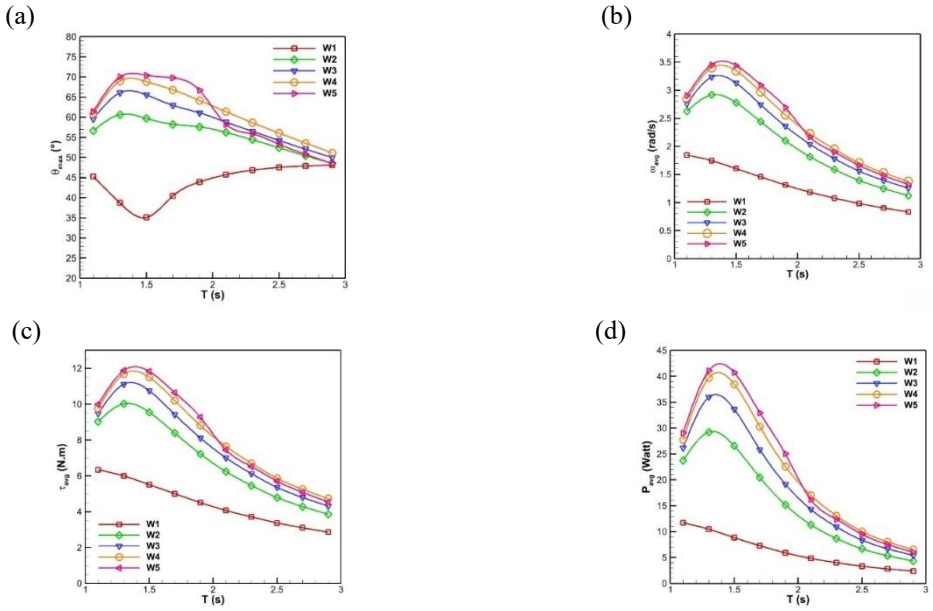

Figure 6. Hydrodynamic parameters at various ocean wave periods, (a) maximum response, (b) average angular velocity, (c) average torque, and (d) average power.

In the context of efficiency, it is formulated by the CWR data shown in Table 4. The data reveal a clear relationship between wave period and CWR, with an optimal performance zone for each flap width. As the wave period increases, the CWR for all configurations generally decreases after reaching a peak. The narrowest flap, W1, achieves its highest efficiency at the shortest wave period of around 1.1 s, with a CWR of 45.74%. However, the medium-width flaps (W2 and W3) demonstrate superior performance; they reached their peak efficiencies at a slightly longer period of around 1.3 s, with CWR values of 70.77% and 70.29%, respectively. The CWR for the widest flaps, W4 and W5, peaks at around 1.3 s, but at lower values of 62.08% and 53.50%, respectively. Beyond this optimal period, the efficiency for all flaps drops significantly. For instance, at 2.9 s, the CWR for all configurations falls below 11%. The data suggest that while wider flaps (W4 and W5) are effective at capturing a large wave front, their increased mass and hydrodynamic resistance might reduce their overall CWR compared to moderately-sized flaps (W2 and W3), especially in the optimal wave period range. This indicates that there is an optimal flap width that balances wave capture efficiency and hydrodynamic resistance to maximize the CWR. It can be noted that the current study achieved a higher maximum efficiency of 70.77% compared to other studies, which reach a maximum efficiency of around 50% [9], [10]

Table 4. Efficiency of the Flap Variations at Different Wave Periods.

Period (s)	Capture Width Ratio				
	W1	W2	W3	W4	W5
1.1	45.74%	57.45%	51.13%	43.38%	37.85%
1.3	40.96%	70.77%	70.29%	62.08%	53.50%
1.5	34.57%	64.29%	65.75%	60.16%	53.05%
1.7	26.79%	46.55%	47.47%	44.51%	40.33%
1.9	20.81%	33.04%	33.69%	31.76%	29.33%
2.1	16.45%	23.90%	24.35%	23.18%	18.35%
2.3	13.31%	17.90%	18.15%	17.38%	13.70%
2.5	10.84%	13.52%	13.66%	13.11%	10.33%
2.7	9.03%	10.69%	10.79%	10.35%	8.07%
2.9	7.58%	8.54%	8.63%	8.30%	6.39%

4. CONCLUSION

Using the Boundary Element Method (BEM), this study confirmed that flap width is a critical design parameter for the Oscillating Wave Surge Converter (OWSC), directly impacting energy capture and power output. In the time domain, increasing flap width led to proportional increases in motion response, angular velocity, torque, and power due to greater wave energy absorption and a stronger excitation force. However, increased inertia introduced a damping effect, causing less stable peak-to-trough transitions. In the frequency domain, each flap width exhibited a specific resonant peak (W1 at around 1.1 s; W2-W5 at around 1.3-1.5 s), but optimal efficiency was found in the moderately sized flaps (W2 and W3). The configurations achieved the highest Capture Width Ratio (CWR) values of 70.766% and 70.289%, respectively. When designing OWSC flaps, there should be a balance between wave capture against the dampening effects of inertia and hydrodynamic resistance, as moderately sized flaps (W2 and W3) achieved the highest efficiencies, outperforming wider flaps. Additionally, the frequency domain analysis guides designers to tune the flap's performance to the local wave climate: narrower flaps (W1) resonate best at shorter wave periods (around 1.1 s), while wider flaps (W2-W5) perform optimally at longer periods (around 1.3-1.5 s). This suggests that simply widening the flap does not guarantee maximum efficiency due to the adverse effects of added mass and hydrodynamic resistance, underscoring the need for future research with a finer resolution of wave periods to pinpoint the optimal design for specific wave climates.

6. REFERENCES

[1] Intergovernmental Panel on Climate Change (IPCC), “Climate Change 2022 - Mitigation of Climate Change: Working Group III Contribution to the Sixth Assessment Report of the Intergovernmental Panel on Climate Change,” *Cambridge University Press*, Jul. 2023, doi: doi.org/10.1017/9781009157926.

[2] IRENA, *Renewable Capacity Statistics 2025* . Abu Dhabi: International Renewable Energy Agency, 2025.

[3] W. R. Sari, G. Gunawan, A. Surjosatyo, D. Angga, and F. Muzhoffar, “Systematic Analysis of Potential Marine Renewable Energy for Coastal Ecological Balance on Bawean Island: A Review,” *International Journal of Marine Engineering Innovation and Research*, vol. 9, no. 2, pp. 1479–2548, Jun. 2024, doi: 10.12962/J25481479.V9I2.20298.

[4] A. Shadmani, M. R. Nikoo, A. H. Gandomi, M. Chen, and R. Nazari, "Advancements in optimizing wave energy converter geometry utilizing metaheuristic algorithms," *Renewable and Sustainable Energy Reviews*, vol. 197, p. 114398, Jun. 2024, doi: 10.1016/J.RSER.2024.114398.

[5] B. Yang *et al.*, "Wave energy converter array layout optimization: A critical and comprehensive overview," *Renewable and Sustainable Energy Reviews*, vol. 167, p. 112668, Oct. 2022, doi: 10.1016/J.RSER.2022.112668.

[6] W. A. Arrosyid *et al.*, "Recent advancements in wave energy converter technologies: A comprehensive review on design and performance optimization," *Ocean Engineering*, vol. 340, p. 122328, Nov. 2025, doi: 10.1016/J.OCEANENG.2025.122328.

[7] J. Cui, X. Chen, and S. Dai, "Numerical study on dual oscillating wave surge converter with different cross-section shapes using SPH under regular waves," *Ocean Engineering*, vol. 271, p. 113755, Mar. 2023, doi: 10.1016/J.OCEANENG.2023.113755.

[8] Y. Lin and F. Pei, "Numerical study on bottom-hinged plate wave energy converter geometry design," *Ocean Engineering*, vol. 260, Sep. 2022, doi: 10.1016/j.oceaneng.2022.112050.

[9] R. A. Anggara, J. Julian, F. Wahyuni, R. H. Purba, and N. T. Bunga, "Investigation of Flap Dimensional Parameters to Improve Hydrodynamic Performance of Oscillating Wave Surge Converter Device," *Jurnal Asiimetrik: Jurnal Ilmiah Rekayasa & Inovasi*, vol. 7, no. 1, pp. 59–70, Jan. 2025, doi: 10.35814/ASIIMETRIK.V7I1.7911.

[10] D. Wang, S. Qiu, and J. Ye, "Width effects on hydrodynamics of pendulum wave energy converter," *Applied Mathematics and Mechanics (English Edition)*, vol. 35, no. 9, pp. 1167–1176, Sep. 2014, doi: 10.1007/s10483-014-1857-6.

[11] Y. Wei, T. Abadie, A. Henry, and F. Dias, "Wave interaction with an Oscillating Wave Surge Converter. Part II: Slamming," *Ocean Engineering*, vol. 113, pp. 319–334, Feb. 2016, doi: 10.1016/j.oceaneng.2015.12.041.

[12] J. N. Newman, "Marine Hydrodynamics, 40th edition," *The MIT Press Cambridge, Massachusetts London, England*, p. 450, 2018, Accessed: Aug. 18, 2025. [Online]. Available: https://mitpress.mit.edu/9780262534826/marine-hydrodynamics/

[13] J. Julian *et al.*, "Study of hydrodynamic characteristics in oscillating wave surge converter," *Jurnal Polimesin*, vol. 22, no. 2, pp. 158–164, Apr. 2024, doi: 10.30811/JPL.V22I2.4715.

[14] P. J. Roache, "Perspective: A Method for Uniform Reporting of Grid Refinement Studies," *J Fluids Eng*, vol. 116, no. 3, pp. 405–413, Sep. 1994, doi: 10.1115/1.2910291.

[15] D. Hoek, "Forced Changes Only: A New Take on the Law of Inertia," *Philos Sci*, vol. 90, no. 1, pp. 60–76, Jan. 2023, doi: 10.1017/PSA.2021.38.

[16] H. N. Nguyen, "Is the Velocity Always in Phase with the Wave Excitation Force in Constrained Optimal Control of Wave Energy Converters?," *IFAC-PapersOnLine*, vol. 56, no. 2, pp. 2632–2637, Jul. 2023, doi: 10.1016/J.IFACOL.2023.10.1352.

LOGIC
Journal of Engineering Design and Technology
Vol. 25 No.3 November; p. 210-218

p-ISSN : 1412-114X
e-ISSN : 2580-5649
http://ojs2.pnb.ac.id/index.php/LOGIC

THERMAL PERFORMANCE OF A BRANCHING-CHANNEL LIQUID COOLING SYSTEM FOR CYLINDRICAL LI-ION 18650 BATTERIES

Anggie Topan Wijaya[1)], James Julian[1)*], Fitri Wahyuni[1)], Riki Hendra Purba[1)], Fathin Muhammad Mahdhudhu[2)], Elvi Armadani[3)], Adi Winarta[4)]

1) Mechanical Engineering, Universitas Pembangunan Nasional Veteran Jakarta, Jakarta
2) Naval Architecture, Universitas Pembangunan Nasional Veteran Jakarta, Jakarta
3) Industrial Engineering, Universitas Pembangunan Nasional Veteran Jakarta, Jakarta
4) Mechanical Engineering, Politeknik Negeri Bali, Bali

Corresponding email [1)] : zames@upnvj.ac.id

Abstract. Lithium-ion batteries need effective thermal management to avoid safety risks like thermal runaway. This study analyzes and optimizes a liquid cooling system. Battery Thermal Management System (BTMS) using a branching mini-channel cold plate design for eight Li-ion 18650 batteries. A Computational Fluid Dynamics model was developed to simulate performance at a 2C discharge rate with configurations of 3 (N3), 5 (N5), and 7 (N7) branches. The results, validated against experimental data, showed that all configurations kept maximum temperatures below 37°C and maintained temperature uniformity (ΔT) below 5°C. Increasing branches reduced pressure drop, with the N7 design showing the lowest ΔP of 5.16 Pa. Although it had a lower heat transfer coefficient, N7 achieved the highest J/F factor, indicating optimal thermo-hydraulic performance for liquid-cooled battery systems.

Keywords: BTMS, Branching Mini-Channel, Cold Plate, Li-Ion 18650, Liquid Cooling.

1. INTRODUCTION

In recent years, many studies have focused on energy sources, but continue to face challenges, mainly environmental pollution [1]. The G20 countries collectively account for about 76% of global greenhouse gas emissions, largely from natural resource use [2]. Advances in technology have encouraged the adoption of safer energy alternatives, such as batteries [3]. Cylindrical Li-ion batteries are particularly practical and widely applied in electric vehicles, backup systems, and small electronics [4]. However, their performance and safety remain sensitive to temperature variations [5]. Poor temperature control can cause thermal degradation, shorten service life, or even trigger thermal runaway and explosion [6].

Recent studies on battery cooling aim to reduce excessive heat generation in lithium-ion cells [7]. This effort led to the development of the Battery Thermal Management System (BTMS), designed to maintain optimal battery temperatures between 25°C-40°C and ensure temperature uniformity with $\Delta T < 5°C$ [8], [9]. The BTMS also enhances temperature homogeneity across all battery cells, extending cycle life and reducing operational costs [10], [11], [12]. Various configurations for BTMS have been suggested, such as systems utilizing air cooling, liquid cooling, phase change materials (PCM), and hybrid cooling methods [13]. Cooling strategies are generally categorized into active and passive systems. Among active approaches, liquid-based cooling is considered beyond effective than air cooling due to its superior heat removal and temperature stability [14], [15], [16]. Previous studies have examined liquid-cooling plates, as shown in Table 1.

Previous studies indicate that liquid cooling effectively reduces T_{MAX}, yet maintaining temperature uniformity (ΔT) remains challenging. Conventional serpentine designs face efficiency trade-offs under high discharge rates due to significant pressure drops (ΔP), while bionic channels introduce manufacturing complexity. Therefore, this study fills the gap in the research by numerically analyzes and optimizes a liquid-based BTMS using branching channel designs (3, 5, and 7 branches), considering branched designs offer an optimal balance between ease of manufacturing and high thermal performance. By optimizing the number of branches, this study hopes that simple geometries can compete with complex designs in maintaining battery temperature without complicated processes.

Table 1. Comparative Analysis of Previous Studies

Ref.	Author (s)	Configuration	Battery Type	Findings	Trade-offs
[17]	Ibrahim et al.	Serpentine Channel	18650 Cylindrical	Maintained T_{MAX} < 50°C (peak 46°C) and ΔT = 8.6°C at 2C discharge rate.	Failed to maintain ΔT < 5°C under higher discharge rates
[18]	Patil et al.	U-shaped Hexagonal	Pouch Cell	Inlet temperature affects T_{MAX} (99.31%), channel count affects ΔT (46.09%). Optimized ΔT reached 0.22°C.	Numerical sensitivity focus; specific geometry optimization required.
[19]	Li et al.	Hybrid (Heat pipe + Serpentine)	Prismatic	Significantly reduced ΔT by approximately 72.49% compared to standard plates.	Increased system complexity, weight, and manufacturing cost.
[20]	Wang et al.	Bionic Spider-web	Pouch Cell	Achieved T_{MAX} = 37.89°C at extreme 12C rate.	Poor temperature uniformity ΔT= 8.86°C exceeding the 5°C target.
[21]	Luo et al.	Square-Spiral-Ring	Prismatic	T_{MAX} = 33.63°C ΔT= 6.45 °C Pressure drop reduced by 686.8 Pa compared to serpentine.	ΔT remained above the ideal threshold of 5°C.
[22]	Wang et al.	Bionic Butterfly-shaped	Prismatic	Excellent uniformity ΔT = 4.99°C and low pressure drop (36.26 Pa vs. 189.11 Pa for serpentine).	Complex geometry leads to difficulty in manufacturability.

2. METHODS

2.1 Lithium-ion Battery Model

This research focuses on a liquid cooling system that has been designed explicitly for a cylindrical lithium-ion cell of the 18650 type. The arrangement of battery packs in terms of their thermal generation properties will be treated equally because the batteries are of the same type. The dimensions of the battery model are shown in Figure 1. It has a height of 65 mm and a diameter of 18 mm.

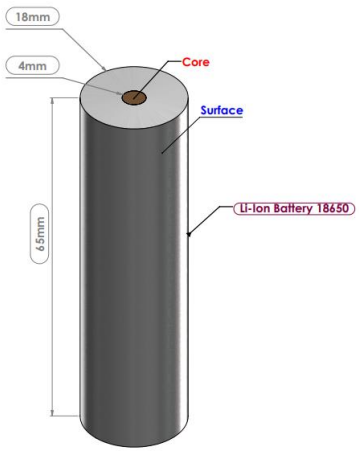

Figure 1. Lithium-ion 18650 battery model

2.2 Mini-Channel Cold Plate Models

Figure 2 illustrates the configuration of the batteries placed in a single module, followed by a visualization of the small channel branches inside the cooling plate. The liquid-based cooling configuration implemented consists of three different models: a three-branch, a five-branch, and a seven-branch mini-channel cold plate. There are eight battery arrays positioned in the cold plate. This configuration was chosen considering the liquid cooling strategy centered on mini-channels applied to induce forced convection. The cold plate component functions as the main source of heat exchange between the batteries and the fluid flow and is made of aluminum. The developed design also identifies key components such as the dimensions of the cold plate and the placement of the batteries.

Furthermore, Table 2 provides information on the material properties applied in this study including density, specific heat, thermal conductivity, and viscosity. Aluminum is utilized for the cold plate, while water serves as the cooling fluid.

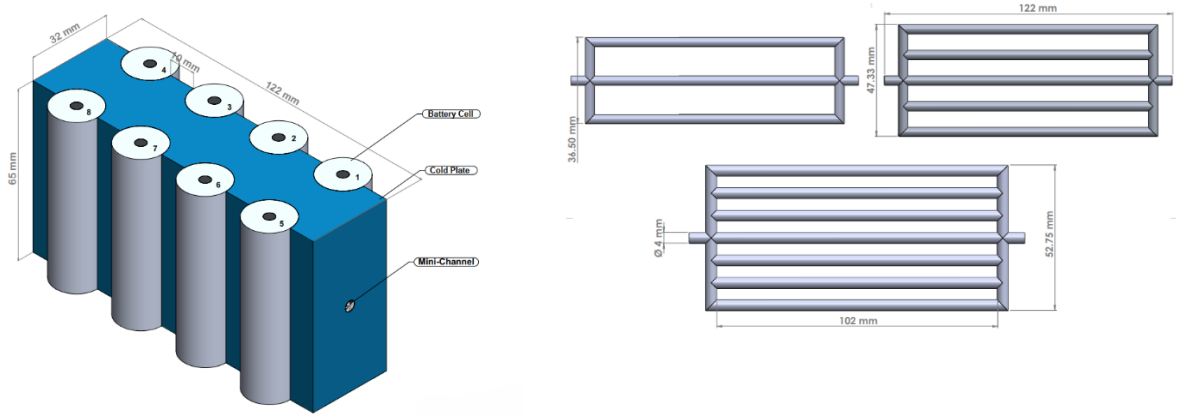

Figure 2. The structure of the branching mini-channel cold plate

Table 2. Thermal-physical Properties of the Battery Conditions

Material	ρ (kg.m^{-3})	c (J.kg^{-1}.k^{-1})	k (W.m^{-1}.k^{-1})	μ (Pa.s)
Alumunium	2179	871	202.4	-
Battery	2534.26	1558.3	3.02	-
Water	998.2	4128	0.6	1.03x10-3

2.3 Governing Equations

In this numerical study, a Computational Fluid Dynamics (CFD) solver is used. Then, to measure the interaction between the working fluid and the mini channel branching inside the cold plate, the concept of heat transfer is used because this phenomenon occurs to release heat from the battery. The mass flow rate applied to the cooling system design is defined as laminar flow. Therefore, fluid flow in this work utilizes the Navier-Stokes technique. To ensure that the fluid mass flow remains constant within the channel domain, equation (1), the Mass Conservation, is used to ensure that the fluid mass flow remains constant throughout the channel. Then, equation (2), momentum conservation, is used to measure the pressure distribution and velocity distribution along the flow moving within the channel. Equation (3) is functioned to model the phenomena of energy conservation and heat generation in batteries. Equation (4) is used to formulate a heat generation model based on the actual battery temperature conditions obtained from the experiment [23]. Furthermore, equation (5) is used to represent two heat generations to predict unsteady-state heat transfer in the battery, at locations in the core and surface of the battery.

$$\frac{\partial \rho}{\partial t} + \frac{\partial}{\partial x_i}(\rho u_i) = 0 \tag{1}$$

$$\rho_l \left[\frac{\partial \vec{v}}{\partial t} + (\vec{v} \bullet \nabla)\vec{v} \right] = -\nabla p + \mu \nabla^2 \vec{v} \tag{2}$$

$$\rho C_p \frac{\partial T}{\partial t} = \lambda_x \frac{\partial^2 T}{\partial^2 x} + \lambda_y \frac{\partial^2 T}{\partial^2 y} + \lambda_z \frac{\partial^2 T}{\partial^2 z} + Q_{gen} \tag{3}$$

$$Q_{gen}(t) = \rho C_p \frac{\Delta T}{\Delta t} \tag{4}$$

$$Q_{gen(1-2)}(x,y,z,t) = Q_{gen(1-2)}(t) - \lambda \nabla^2 T_{(1-2)} \tag{5}$$

2.4 Mesh and Boundary Conditions

An unstructured mesh in the shape of a tetrahedron was created in this study. This type of mesh is used because of its suitability for complex geometric shapes. The final mesh is shown in Figure 3(a). The variations used in this study are shown in Table 3, which shows the implementation of different numbers of channel branches in the

developed cooling model configuration. The channel diameter was fixed at 4 mm, and the mass flow rate was fixed at 0.0005 kg/s in each simulation case. The boundary conditions design is presented in Figure 3(b) , which consists of a battery, cold plate, and liquid zone. During the computational setup, the battery and aluminum cooling plate were set at a temperature of 35°C, following the ambient temperature experimental validation data for this article. Then, the initial water temperature was set at 25°C. Furthermore, a discharge rate of 2C was implemented in this case, considering the experimental data referred to, with heat generation applied as a heat source at radial gradient.

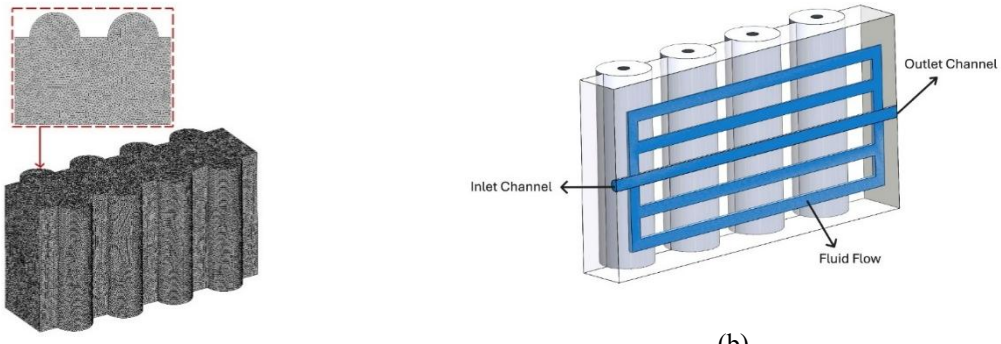

(a) (b)

Figure 3. The parameter specifications of this research: (a) mesh, (b) boundary conditions

Table 3. Parameter Variations in this Study

Number of channels (Branch)	Mass Flow Rate	Diameter Inlet (Ø)
3 Channel (N3) 5 Channel (N5) 7 Channel (N7)	0.0005 kg/s	4 mm

2.5 Non-dimensional Parameter

To expand the analytical understanding of the performance of the liquid cooling system implemented, this study adds a discussion on J/F, which is a non-dimensional factor number to calculate the performance efficiency approach. The non-dimensional parameter to measure the ability of fluids to transfer heat by convection is defined as the J factor, outlined in equation (6). Equation (7) is used to predict the flow regime, and equation (8) indicates the efficiency, the ratio of convective to conductive heat transfer across the boundary. The heat transfer rate, which is the measurement of thermal energy transfer per unit time, of the cold plate is quantified using equation (9). Equation (10) calculates the rate of heat absorption by the working fluid flow within the channel. The F factor, as a non-dimensional measure of pressure loss due to friction between the fluid and the channel walls, was evaluated using equation (11). Then, equation (12) calculates the pressure drop of the channel.

$$j = \frac{Nu}{Re \cdot Pr^{1/3}} \tag{6}$$

$$Re = \frac{\rho U D}{\mu} \tag{7}$$

$$Nu = \frac{h_w D}{\mu} \tag{8}$$

$$h_w = \frac{Q_l}{A_c[T_{bmax} - (T_{lin} + T_{lout})/2]} \tag{9}$$

$$Q = m.C_p.\ (T_{in} - T_{out}) \tag{10}$$

$$f = \frac{2\Delta p D c}{\rho_l U_{in}^2 L} \tag{11}$$

$$\Delta P = P_{in} - P_{out} \tag{12}$$

2.6 Mesh Independence Test

To ensure mesh quality, the estimation of numerical error for each mesh configuration was conducted using the Grid Convergence Index (GCI) method [24]. To calculate the ratio between the grid spacing of the fine mesh and the coarser mesh, using equation (13). Then, for determines how quickly the numerical error decreases as the grid is refined using equations (14). To calculate the uncertainty band error percentage for the fine and coarse mesh

used, indicating how far the result might be from the asymptotic true value (15) and (16), respectively, while the GCI reliability was verified through equation (18), and the benchmark value was used to calculate the true error of the simulation using equation (19). As summarized in Table 4, tests on battery 1, using its average temperature value, showed that the coarse, medium, and fine meshes contained 875,767, 1,751,435, and 3,502,671 elements, respectively. The fine mesh exhibited stable results with an error below 5%, confirming for subsequent analyses.

$$r = \frac{h_2}{h_1} \tag{13}$$

$$\overline{p} = \frac{\ln\left(\frac{f_3 - f_2}{f_2 - f_1}\right)}{\ln(r)} \tag{14}$$

$$GCI_{fine} = \frac{F_s \,|\in|}{\left(r^{\overline{p}} - 1\right)} \tag{15}$$

$$GCI_{coarse} = \frac{F_s \,|\in| \, r^{\overline{p}}}{\left(r^{\overline{p}} - 1\right)} \tag{16}$$

$$\in = \frac{f_{n+1} - f_n}{f_n} \tag{17}$$

$$\frac{GCI_{coarse}}{GCI_{fine} r^{\overline{p}}} \approx 1 \tag{18}$$

$$f\,\mathrm{r}_{h=0} = f_1 + \frac{(f_1 - f_2)}{\left(r^{\overline{p}} - 1\right)} \tag{19}$$

Table 4. Results of Mesh Independence Study.

Mesh	Fine	Medium	Coarse
Difference of Temperature	35.1546	35.1533	35.1493
$\overline{p}$		1.570096	
r		2	
GCIfine		0.002%	
GCIcoarse		0.0073%	
frh = 0		33.97114	
$\frac{GCI_{coarse}}{GCI_{fine} r^{\overline{p}}} \approx 1$		1	
Error	0.00196%	0.00581%	0.01724%

3. RESULTS AND DISCUSSION

3.1 Validation

To ensure validation can be used in this study, an experimental research approach model is required [23]. The aim is to bring the simulated battery temperature closer to actual conditions in the real world. The heat treatment applied to a single 18650 Li-ion battery included setting the ambient temperature at 35°C with a discharge rate of 2C. For more detailed results, see Figure 4. A close correlation was observed between the simulated and experimental data. Validation was performed by calculating the maximum deviations at the core and surface, which were 3.914% and 3.474%, respectively.

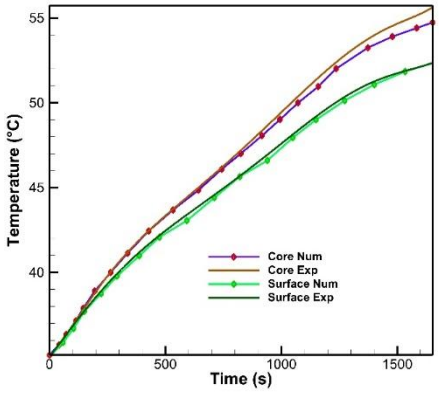

Figure 4. A comparison between numerical and experimental data on a single battery

3.2 Analysis

There are limitations to the model in this study, in which the battery computational domain used is arranged in series and parallel and only consists of eight units. Furthermore, the heat generation treatment in cylindrical batteries is given equally for all batteries, and the working fluid is incompressible. Furthermore, Figure 5(a) presents the evolution of T_{MAX} during discharge with and without mini-channel cold plates. Without active cooling, T_{MAX} rises rapidly and approaches 52°C by the end of the 1650-second simulation, underscoring the need for effective thermal management. With branched cold plates (N3, N5, and N7), the temperature rise is successfully controlled, with all configurations keeping T_{MAX} below 37°C after the initial peak at around 150 seconds. The differences among N3, N5, and N7 are minimal, only about 0.3°C at 900 seconds, because increasing the number of branches expands the heat-transfer surface and improves coolant distribution. Once steady operation is reached, the cooling system removes heat faster than the battery generates it, causing T_{MAX} to stabilize and gradually decline. The ΔT results, shown in Figure 5(b), indicate that all mini-channel configurations (N3, N5, N7) maintain excellent temperature uniformity, with values well below the 5°C threshold. The highest ΔT of about 2.4°C appears in N7, slightly higher than N3 and N5. This occurs because adding more branches lowers coolant velocity, briefly reducing convective heat transfer during early discharge. The ΔT increase in N7 is driven mainly by a drop in T_{MIN} rather than a rise in T_{MAX} , as the system cools faster than the battery equalizes heat internally.

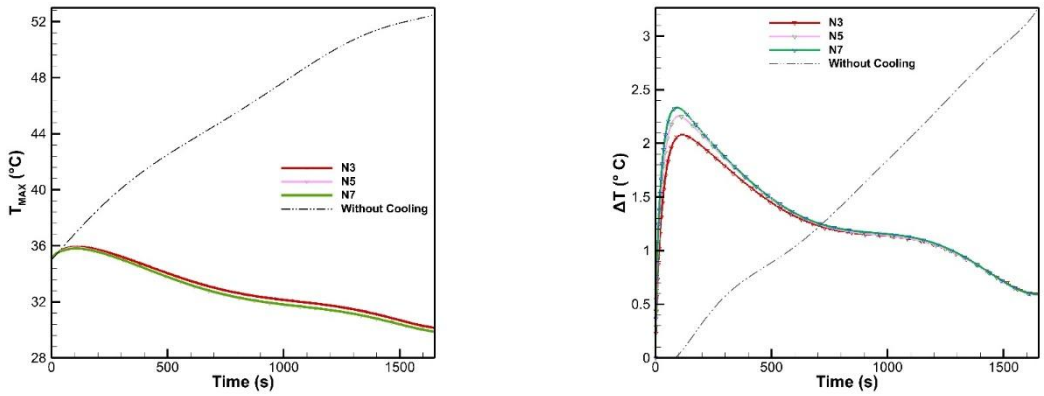

(a) (b)

Figure 5. Thermal response of the battery: (a) maximum temperature, (b) temperature difference for each configuration

Table 5 further shows that increasing the number of branches reduces pressure drop, from 6.42 Pa in N3 to 5.16 Pa in N7, indicating better hydraulic efficiency. However, the heat-transfer coefficient decreases with additional branching: N3 provides the highest value (624.59), while N7 delivers the lowest (291.32). Despite its larger ΔP, N3 still offers the strongest heat-transfer capability, demonstrating a practical performance trade-off.

Table 5. Pressure Drops and the Heat Transfer Coefficient with Each Configuration

Branching Channel	ΔP (Pa)	H_w (W $m^{-2}.K^{-1}$
N3	6.42	624.59
N5	5.50	391.32
N7	5.16	291.32

To evaluate the overall thermo-hydraulic accomplishment, Figure 6 presents the J/F analysis used to assess overall thermo-hydraulic performance by comparing heat-transfer effectiveness with the energy required to overcome frictional losses. The results show a steady increase in J/F as the number of branches grows. N7 delivers the highest value at about 0.21, followed by N5 at roughly 0.19, and N3 at around 0.17. This pattern indicates that the reduction in frictional losses outweighs the decrease in heat-transfer rate when the branches increase from 3 to 7. Consequently, the N7 configuration demonstrates the best overall thermo-hydraulic performance.

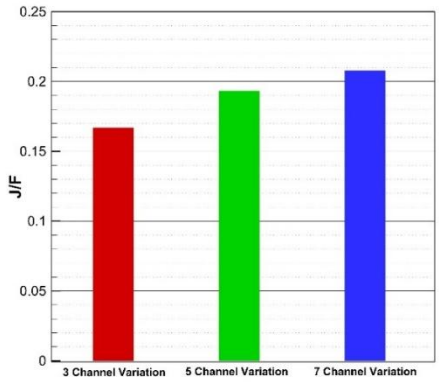

Figure 6. Thermal response of the battery for each configuration with the temperature difference

Figures 7, 8, and 9 collectively show that all configurations (N3, N5, N7) maintain good thermal uniformity at 1650 seconds, but N7 delivers the most compact high-temperature region. Physically, the N7 design increases the effective contact surface area and reduces the conduction path length between the battery surface and the coolant, facilitating more efficient heat extraction. Consequently, remaining hot spots are limited to areas outside the cold-plate contact zone, highlighting the geometric limitation where the cold plate does not fully envelop the battery cell. In contrast, N3 displays stronger temperature gradients due to fewer channels, which creates wider uncooled gaps between branches where heat accumulation occurs, while N5 performs at an intermediate level. Heat-flow contours further indicate that N7 provides the most uniform heat transport along the mini-channels, reducing local overheating and supporting better long-term battery stability. Pressure contours also reveal clear hydraulic differences: N3 experiences abrupt pressure changes as the flow splits into only three branches, increasing energy loss, whereas N7 maintains a lower-drop pressure distribution.

To apply this research to the real world, the right step for the battery manufacturing industry is to adopt a liquid cooling system design with branching channels so that it can be mass-produced. This is because, based on the above research results, the proposed cooling system for 18650 cylindrical Lithium-ion battery provides the best thermo-hydraulic performance balance and is able to maintain the battery temperature in the best condition and achieve temperature uniformity. With direct application in the real world, this means that the cooling pump requires less electrical power to circulate fluid in this cooling system. But the design needs to be further developed by expanding the cooling contact area and testing it under dynamic discharge rate conditions.

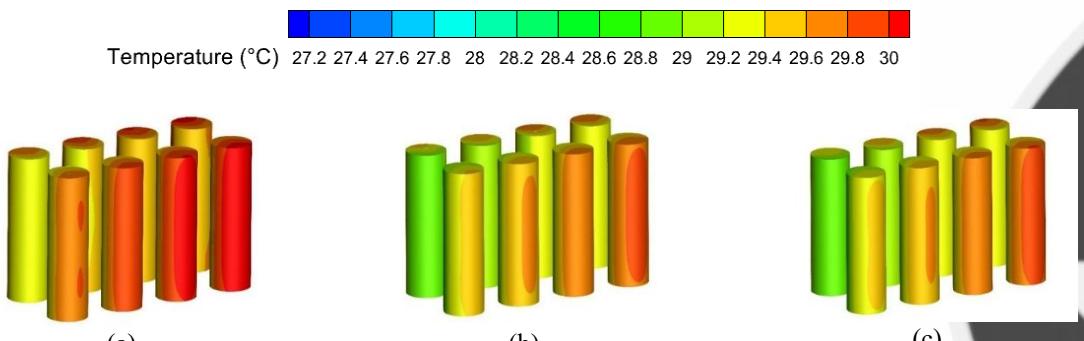

(a) (b) (c)

Figure 7. A comparison of thermal contour distribution of the battery (a) N3, (b) N5, (c) N7

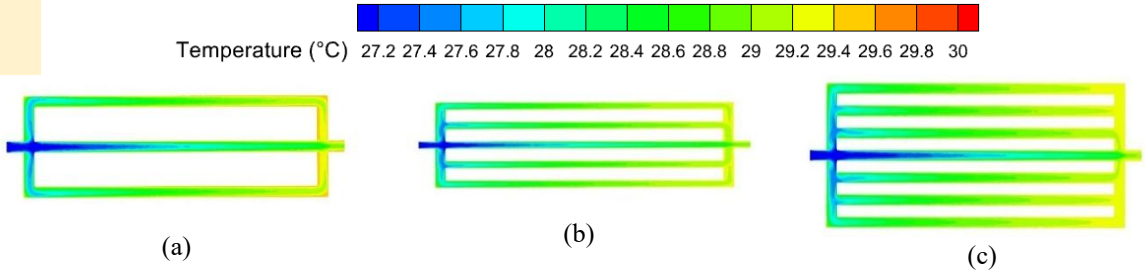

Figure 8. A comparison of branching mini-channel temperature distribution: (a) N3, (b) N5, (c) N7

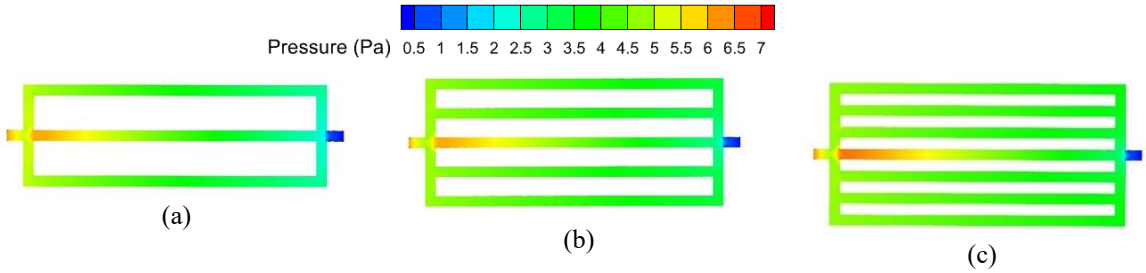

Figure 9. A comparison of branching mini-channel pressure distribution: (a) N3, (b) N5, (c) N7.

4. CONCLUSION

This numerical study examined the thermo-hydraulic behavior of a liquid-cooled BTMS using branching mini-channel cold plates for 18650 Li-ion batteries. All configurations (N3, N5, N7) successfully kept T_{MAX} below 37°C and maintained ΔT far under the 5°C threshold throughout discharge, meeting essential BTMS performance criteria. Increasing the number of branches lowered the pressure drop from 6.42 Pa (N3) to 5.16 Pa (N7), indicating reduced energy demand, though it was accompanied by a decline in the convective heat-transfer coefficient. Overall, N7 delivered the strongest and balanced performance, achieving the highest J/F value (0.21). This study has several limitations. The cooling plate design only uses side contact, so the battery poles and opposing surface rely on internal conduction, which causes hot spots outside the contact area. In addition, the analysis was performed at a constant discharge rate, so the transient thermal behavior under dynamic loads such as real driving cycles is still unknown. Future research should focus on improving the contact interface and evaluating performance under varied and realistic load profiles.

5. REFERENCES

[1] N. M. Malima, S. J. Owonubi, G. B. Shombe, N. Revaprasadu, and E. R. Sadiku, "Bioelectrochemical Technology for Sustainable Energy Production and Waste Treatment," in Bioelectrochemical Systems: Vol.2 Current and Emerging Applications, P. Kumar and C. Kuppam, Eds., Singapore: Springer, 2020, pp. 131–175. doi: 10.1007/978-981-15-6868-8_6.

[2] D. Murat, B. İnam, D. Murat, and B. İnam, "Relationship Between Fiscal Policies and Green Economy: An Application for G20 Countries," https://services.igi-global.com/resolvedoi/resolve.aspx?doi=10.4018/979-8-3693-2845-3.ch019. Accessed: Oct. 23, 2025. [Online]. Available: https://www.igi-global.com/gateway/chapter/www.igi-global.com/gateway/chapter/351395

[3] L. D. Tai and M.-Y. Lee, "Advances in the Battery Thermal Management Systems of Electric Vehicles for Thermal Runaway Prevention and Suppression," Batteries, vol. 11, no. 6, p. 216, June 2025, doi: 10.3390/batteries11060216.

[4] C.-L. Wang and J. C. Leong, "Analysis of Thermal Management Strategies for 21700 Lithium-Ion Batteries Incorporating Phase Change Materials and Porous Copper Foam with Different Battery Orientations," Energies, vol. 17, no. 7, p. 1553, Jan. 2024, doi: 10.3390/en17071553.

[5] N. Piao et al., "Challenges and development of lithium-ion batteries for low temperature environments," eTransp., vol. 11, 2022, doi: 10.1016/j.etran.2021.100145.

[6] Y. A. Bhutto, A. K. Pandey, R. Saidur, K. Sharma, and V. V. Tyagi, "Critical insights and recent updates on passive battery thermal management system integrated with nano-enhanced phase change materials," Materials Today Sustainability, vol. 23, p. 100443, Sept. 2023, doi: 10.1016/j.mtsust.2023.100443.

[7] F. A. Khalaf and A. L. Tarish, "Recent update progress for the battery thermal management of electric vehicles: challenges and solutions," Journal of Thermal Analysis and Calorimetry, vol. 150, no. 16, pp. 12135–12156, Aug. 2025, doi: 10.1007/s10973-025-14524-x.

[8] H. Tomar, S. Singh, P. Gupta, and K. Sireesha, "Design and Analysis of Thermal Management Systems for an Electric Vehicle Battery," in 2025 First International Conference on Advances in Computer Science, Electrical,

Electronics, and Communication Technologies (CE2CT), Feb. 2025, pp. 320–324. doi: 10.1109/CE2CT64011.2025.10941560.
[9] I. M. M. Benounnane, A. W. Belarbi, and M. E. B. Ghribi, "Comparative Analysis of Thermal Conductive Materials for Optimizing the Thermal Management of a Lithium-Ion Battery Pack," in 2024 3rd International Conference on Advanced Electrical Engineering (ICAEE), Nov. 2024, pp. 1–5. doi: 10.1109/ICAEE61760.2024.10783307.
[10] J. Zhao, P. Lv, and Z. Rao, "Experimental study on the thermal management performance of phase change material coupled with heat pipe for cylindrical power battery pack," Experimental Thermal and Fluid Science, vol. 82, pp. 182–188, Apr. 2017, doi: 10.1016/j.expthermflusci.2016.11.017.
[11] C. Wu, J. Ni, and X. Shi, "Research on multiple thermal conductivity phase-change-material-liquid thermal management system considering thermal safety and temperature uniformity of battery pack," Journal of Energy Storage, vol. 136, p. 118456, Nov. 2025, doi: 10.1016/j.est.2025.118456.
[12] M. Olyaei et al., "Virtual Testbed for Economical and Reliability Analysis of Battery Thermal Management Control Strategies1," Journal of Electronic Packaging, vol. 146, no. 041110, Aug. 2024, doi: 10.1115/1.4065988.
[13] A. Gharehghani et al., "Progress in battery thermal management systems technologies for electric vehicles," Renewable and Sustainable Energy Reviews, vol. 202, p. 114654, Sept. 2024, doi: 10.1016/j.rser.2024.114654.
[14] C. Wu, Z. Wang, Y. Bao, J. Zhao, and Z. Rao, "Investigation on the performance enhancement of baffled cold plate based battery thermal management system," Journal of Energy Storage, vol. 41, p. 102882, Sept. 2021, doi: 10.1016/j.est.2021.102882.
[15] A. Verma, T. Saikia, P. Saikia, D. Rakshit, and C. E. Ugalde-Loo, "Thermal performance analysis and experimental verification of lithium-ion batteries for electric vehicle applications through optimized inclined mini-channels," Applied Energy, vol. 335, p. 120743, Apr. 2023, doi: 10.1016/j.apenergy.2023.120743.
[16] Y. Chung and M. S. Kim, "Thermal analysis and pack level design of battery thermal management system with liquid cooling for electric vehicles," Energy Conversion and Management, vol. 196, pp. 105–116, Sept. 2019, doi: 10.1016/j.enconman.2019.05.083.
[17] A. Ibrahim, J. Guo, Y. Wang, Y. Zheng, B. Lei, and F. Jiang, "Performance of serpentine channel based Li-ion battery thermal management system: An experimental investigation," International Journal of Energy Research, vol. 44, no. 13, pp. 10023–10043, 2020, doi: 10.1002/er.5599.
[18] M. S. Patil, J.-H. Seo, S. Panchal, and M.-Y. Lee, "Numerical study on sensitivity analysis of factors influencing liquid cooling with double cold-plate for lithium-ion pouch cell," International Journal of Energy Research, vol. 45, no. 2, pp. 2533–2559, 2021, doi: 10.1002/er.5946.
[19] Y. Li, H. Guo, F. Qi, Z. Guo, M. Li, and L. Bertling Tjernberg, "Investigation on liquid cold plate thermal management system with heat pipes for LiFePO4 battery pack in electric vehicles," Applied Thermal Engineering, vol. 185, p. 116382, Feb. 2021, doi: 10.1016/j.applthermaleng.2020.116382.
[20] J. Wang, X. Liu, F. Liu, Y. Liu, F. Wang, and N. Yang, "Numerical optimization of the cooling effect of the bionic spider-web channel cold plate on a pouch lithium-ion battery," Case Studies in Thermal Engineering, vol. 26, p. 101124, Aug. 2021, doi: 10.1016/j.csite.2021.101124.
[21] W. Luo et al., "A numerical study of battery thermal management system with square spiral ring-shaped liquid cooling plate," Thermal Science and Engineering Progress, vol. 45, p. 102120, Oct. 2023, doi: 10.1016/j.tsep.2023.102120.
[22] Y. Wang et al., "Optimization of liquid cooling for prismatic battery with novel cold plate based on butterfly-shaped channel," Journal of Energy Storage, vol. 73, p. 109161, Dec. 2023, doi: 10.1016/j.est.2023.109161.
[23] N. Wang, A. Chen, W. Zhao, R. Zhu, and B. Duan, "An online temperature estimation for cylindrical lithium-ion batteries based on simplified distribution electrical-thermal model," Journal of Energy Storage, vol. 55, p. 105326, Nov. 2022, doi: 10.1016/j.est.2022.105326.
[24] P. J. Roache, "Perspective: A Method for Uniform Reporting of Grid Refinement Studies," J. Fluids Eng, vol. 116, no. 3, pp. 405–413, Sept. 1994, doi: 10.1115/1.2910291.